Multi-Resolution Techniques for a Compressible Staggered LES Numerical Code

a dissertation submitted to the Doctoral Committee of
Tecnologia Aeronautica e Spaziale of the
Sapienza, Università di Roma
in partial fulfillment of the requirements for the
degree of Doctor of Philosophy

Candidate
Ing. Giacomo Rossi

Tutor
Prof. Bernardo Favini
Mechanical and Aerospace Engineering Department
Sapienza, Università di Roma
Via Eudossiana 18, 00184 Rome, Italy

ENEA Tutor
PhD. Eugenio Giacomazzi
PESE Laboratory, PCEUE Division
Energy Technology Department, ENEA
Via Anguillarese, 301 00123 - Santa Maria di Galeria (Rome), Italy

27th November 2015
XXVI Ciclo

Facoltá di Ingegneria Civile e Industriale
Sapienza, Università di Roma
Via Eudossiana 16, 00184 Rome, Italy

Dedicated to Barbara

Acknowledgments

WWW.PHDCOMICS.COM

Contents

Contents

LIST OF FIGURES

List of Figures

List of Tables

Acronyms

CFD Computational Fluid Dynamics

CPU Central Processor Unit

CRESCO Centro computazionale di RicErca sui Sistemi COmplessi

DNS Direct Numerical Simulation

ENEA Agenzia Nazionale per le Nuove Tecnologie, l'Energia e lo Sviluppo Economico Sostenibile

HeaRT Heat Release and Turbulence code

FDS Flux Difference Splitting

FVS Flux Vector Splitting

IVM Immersed Volume Method

LES Large Eddy Simulation

OOP Object Oriented Programming

MPI Message Parsing Interface

RANS Reynolds Averaged Navier-Stokes

RHS Right Hand Side of an equation

SGS SubGrid-Scale components of flow properties

List of Symbols

τ Viscous part of stress tensor.

$\dot{\omega}_i$ Production – destruction rate of the ith species.

λ Second coefficient of viscosity.

$\underline{\mathbf{S}}$ Stress tensor.

$\mathbf{E}$ Strain rate.

$\mathbf{J}_i$ Diffusive mass flux.

$\mathbf{q}$ Heat flux.

$\mathbf{u}$ Velocity vector.

$\mathbf{V}_i$ Diffusion velocity of the ith species.

$\mathcal{H}_i$ Enthalpy of the ith species.

$\mathcal{R}_u$ Universal gas constant.

μ Coefficient of viscosity.

μ_b Coefficient of bulk viscosity.

ρ Density of the fluid.

D_i Equivalent diffusion coefficient.

E Total energy (internal and kinetic).

f_i Body force per mass unit acting on the ith species.

k Thermal conductivity.

k^{sgs} Subgrid Kinetic Energy.

l Grid level.

M Mach Number.

N_s Number of chemical species.

p Pressure of the fluid.

Pr_T Prandtl Turbulent Number.

r   Refinement ratio.

s_L^0 Laminar flame speed.

s_T Turbulent flame speed.

Sc_T Schmidt Turbulent Number.

T   Temperature of the fluid.

W_i Molecular weight of the ith species.

Y_i Mass fraction of the ith species.

Part I

Research Background

Introduction

İn this introductive chapter a general description of turbulent combustion is presented. Once shown the two main categories (premixed and non-premixed), the attention is focused on the

1.1 Interaction between Flames and Turbulence

Turbulent combustion is visible in most practical combustion systems such as rockets, internal combustion or aircraft engines, while laminar combustion applications are almost limited to lighters, candles and some domestic furnaces. So the study and the modelling of turbulent combustion processes is an important issue to develop and improve practical systems. In general, technical processes in turbulent combustion are subdivided into two classes: premixed and non-premixed combustion; in the first, oxidizer and fuel are mixed together before they reach the flame front, while in the second the mixing between oxidizer and fuel is not "artificially" obtained but is only due to molecular diffusion.

Combustion processes are very difficult to describe using analytical techniques, so numerical simulations for turbulent combustion are growing in importance, also if numerical simulations of turbulent reacting flows are very complex, especially for three points:

- turbulence is one of the most complex phenomenon in non-reacting fluid mechanics, because various time and length scales are involved;

- combustion is a very complex process involving a large range of chemical time and length scales; the chemical reactions that generally control combustion process take place in short times, over thin layers, therefore in the flow field there are very large temperature, density and mass fraction gradients;

- turbulent combustion is the result of a two way interaction between chemical reactions and flow structures; turbulence, in fact, is modified by combustion because of the strong flow accelerations through the flame front due to heat release and the large changes in kinematic viscosity associated with temperature changes; turbulence itself alters the flame structure, because

mixing can enhance chemical reactions but also, in opposite way, turbulence can completely inhibit combustion.

The main effect of turbulence on combustion is to increase combustion rate, both for premixed and for diffusion flames: the reaction rate per unit volume increase, and the combustion becomes more efficient. Once a range of different size eddies has developed, strain and shear at the interface between eddies enhance the mixing; in particular, during the eddy break-up process and the formation of smaller eddies, strain and shear will increase and thereby steepen the concentration gradients at the interface between reactants, which in turn enhances their molecular diffusion. All

FIGURE 1.1. Peters diagram

these aspects can be summarized in figure 1.1, where depending on the flame thickness (on the abscissa) and the flame speed (on the ordinate), different flame regimes can be identified.

1.2 TURBULENT PREMIXED FLAMES

FIGURE 1.2. Turbulent Premixed Flame

Turbulent premixed flames are of tremendous practical importance, because they can be encountered in many useful devices, as spark-ignition engines, gas-turbine engines, industrial gas burners; despite of their widespread availability, there is yet no comprehensive and generally accepted theory of turbulent premixed flames.

The propagation velocity of a turbulent premixed flame depends on the character of the flow and on the thermal and chemical properties of the mixture: a turbulent flame speed s_T is defined as the velocity needed at the inlet of a control volume V to keep a turbulent flame stationary in the mean inside the volume. For a one-dimensional turbulent flame propagating along x_1, the mean fuel mass fraction balance (equation 2.28 on page 20) can be written in the reference frame of the flame as:

$$\rho_1 s_T \frac{\partial \left(\overline{\rho} \widetilde{Y_i} \right)}{\partial t} = -\frac{\partial \left(\overline{\rho \widetilde{Y_i} \widetilde{V_{ij}}} + \overline{\rho} \widetilde{Y_i} \widetilde{V_{ij}} \right)}{\partial x_j} + \overline{\rho} \widetilde{\omega} - \frac{\partial J_{ij}^{SGS}}{\partial x_j} \tag{1.1}$$

Integrating this equation and cancelling the diffusion terms far away from flame front gives:
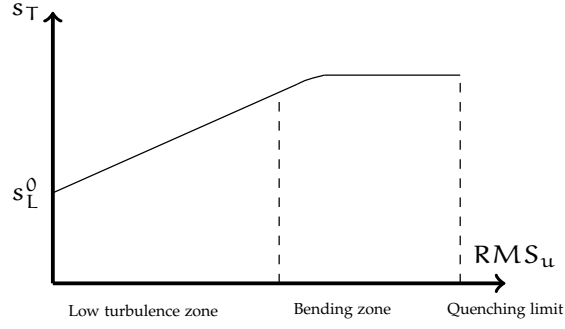
FIGURE 1.3.   Variations of the turbulent flame speed with RMS turbulent speed

$$A \rho_1 Y_F^1 s_T = -\int_V \dot{\omega}_F dV \tag{1.2}$$

where $\dot{\omega}_F$ is the rate at which the reactants are consumed by the chemical reaction, ρ_1 is the density and Y_F^1 is the fuel mass fraction in the fresh gases and A is the area of the box cross section. This equation expresses that the fuel mass flow rate entering the control box is totally consumed by combustion (true for lean mixtures). The turbulent flame speed can be correlated to the laminar flame speed by the:

$$\frac{s_T}{s_L^0} = \frac{A_T}{A} \tag{1.3}$$

This equation shows that the increase of the turbulent flame speed compared to the laminar flame speed s_L^0 is due to the increase of the total flame surface A_T, allowing a higher consumption rate for the same cross section. The ratio A_T/A is the flame wrinkling factor and corresponds to the ratio of available flame surface area divided by its projection in the propagating direction.

In figure 1.3 turbulent flame speed variations are presented: s_T first increases, almost linearly with rms_u, then becomes flat before total quenching occurs for too intense turbulence.

Not only the turbulence influences the shape and the position of the flame front, but also the flame front heavily influences the turbulence: fluid properties almost always depend on fluid temperature, so when temperature changes from one side of the flame front to the other, kinematic viscosity (and therefore local Reynolds number) changes; usually kinematic viscosity increases, so Reynolds number in burnt gases is smaller then in fresh gases, and this effect may lead to relaminarization.

Another effect of the flame on the fluid is flow acceleration through the flame front: this velocity increase can be significant and furthermore occurs in very thin regions, so the flow field can be significantly modified.

4

1.2.1 Structure of Turbulent Premixed Flame

Turbulent premixed flames can be classified into three groups, each of which can be associated to a flame regime:

- wrinkled laminar flames;

- flamelets in eddies;

- distribuited reactions.

In a turbulent flow field, various length scale exist simultaneously: the smallest scale, the Kolmogorov microscale (l_K), represents the smallest eddies in the flow; at the other extreme of the scale spectrum, the integral scale (l_0) characterizes the largest eddy sizes. The structure of a turbulent flame is governed by the relationship between l_K, l_0 and the laminar flame thickness (δ_L), that characterizes the thickness of a reaction zone controlled by molecular transport of heat and mass.

When the flame thickness is much thinner than the smallest scale of turbulence, the turbulent motion can only distort or wrinkle the laminar flame profile: in such case, chemical reactions occur in thin sheets, Damköler number (defined as the ratio between characteristic flow time and characteristic chemical time) is bigger than 1 and a fast-chemistry regime is evident.

At the other extreme, if all scales of turbulence are smaller than the laminar flame thickness, the transport phenomena in the reaction zone are controlled, or at least influenced, by flow turbulence: Damköler number is less than 1.

Flamelets in eddies regime is typified by moderate Damköler numbers and high turbulence intensities: the burning zone consists of parcels of unburned gas and almost fully burned gas; the rate of combustion is determined by the rate at which parcels of unburned gas are broken down into smaller ones, such that there is sufficient interfacial area between the unburned mixture and hot gases to permit reaction; the implication of this is that turbulent mixing rates completely control combustion.

1.3 Turbulent Non Premixed Flames

Turbulent non premixed flames are encountered in a large number of industrial systems, because a perfect reactant mixing, in given proportions, is not required and so burners are simpler to design and to build compared to premixed flames; furthermore, non premixed flames are also safer to operate because they do not exhibit propagation speeds and cannot flashback.

These flames are however more difficult to model because reacting species have to reach, by molecular diffusion, the flame front before reaction: their motion is therefore strongly modified by turbulent motions.

1.3.1 Features of Turbulent Non Premixed Flames

The main characteristic of non premixed flames is that they do not propagate: they are located where fuel and oxidizer meet, and this property is very useful

for safety purposes but has consequences on the interaction between flame and turbulence, because without propagation speed a non premixed flame is unable to impose its own dynamics on the flow field. So a diffusion flame is more sensitive to stretch than a turbulent premixed flame and is more likely to be quenched by turbulent fluctuations.

Another important point is the influence of buoyancy effects, because pressure gradients or gravity forces induce differential effects on fuel, oxidizer and combustion product streams.

Because of all these aspects, flame stabilization is a central design criterion for combustion chambers: insufficient stabilization can result in a combustor which cannot be operated safely or which oscillates dangerously; the choice between stabilization methods is a function of the inlet speeds of the reactants.

For low inlet speeds, the flame can be stabilized directly at the splitter plate separating the fuel and oxidized streams; this regime is seldom observed in real burners because the splitter plate can suffer from excessive heat transfer and because it corresponds to very small powers.

When the fuel speed is high, the flame cannot be stabilized without the use of pilot flames, dump geometries, autoignition or swirlers; in the first case, small premixed flames are used in the vicinity of the jet exit to ensure the flame ignition and stabilization; when one of the fuel or oxidizer streams is sufficiently hot, the flame stabilization may be ensured by auto-ignition process inside the mixing layer, independently of the inlet speeds. If flow speeds are much larger than the flame speed, one solution is to create a recirculating zone which acts as a hot burnt gases tank providing the energy to ignite incoming reactants: this zone can be created by a sudden expansion, in which the recirculating zone is created

FIGURE 1.4. Turbulent Diffusion Flame

by the burner geometry, or by swirlers, that cause a rotating movement of the incoming reactants.

1.3.2 Turbulent Non Premixed Combustion Regimes

Regimes description is very difficult in turbulent non premixed combustion: first, reactant mixing is a complex phenomena that isn't easy to model; the second

Cylindrical geometry	
Total length of the combustion chamber	$z_{max} \approx 80\,cm$
Radius of the combustion chamber	$r_{max} \approx 10\,cm$
Internal inlet diameter	$z_1 = 0.458\,cm$
External inlet diameter	$z_2 = 0.634\,cm$
Inlet wall thickness	$l_w = 0.088\,cm$

TABLE 1.1. Geometrical features of the Sandia Jet "Flame A"

difficulty arises from the fact that diffusion flames do not feature a propagation speed and that the local flame thickness depends on flow conditions. The local flame thickness and speed depend on the local flow conditions such as local strain rates and may be affected by unsteady effects; moreover, in a given burner the flame structure may strongly depend on the spatial location: a flamelet structure may be encountered close to the injectors, while a partial extinction followed by a re-ignition may be found downstream.

1.4 MOTIVATIONS

The doctoral research presented in this dissertation is focused on the development of a multi-resolution and multi-block mesh with staggered variables integration technique for the numerical simulation of compressible and reacting flows. As can be understood from the previous sections, to obtain a satisfactory numerical solution of the flow field with turbulent combustion, a numerical grid with high spatial resolution is mandatory: with multi-block structured grids, both in Cartesian and cylindrical coordinates, this goal isn't always possible to achieve, especially when the numerical simulation is performed on a domain with big dimension and very small elements (like bluff bodies and fuel injectors).

As example can be chosen the numerical simulation of the Sandia "Flame A" jet performed by the mean of HeaRT numerical code [Giacomazzi et al., 2008]: this test case is a $CO/H_2/N_2$ (percentage 40/30/30 in volume) non-premixed, unconfined, turbulent jet flame. The fuel is injected at 292 K from a straight circular tube with squared-off ends (inner diameter 4.58 mm, outer diameter 6.34 mm), with a bulk velocity of $76\,m\,s^{-1}$; the air at 290 K and wet (molar fraction of water 0.012) coflows at $0.75\,m\,s^{-1}$.

The geometrical features (summarized in the table 1.1), don't allow to produce a structured cylindrical mesh with an high spatial resolution on the wall duct and concurrently with a manageable number of grid nodes: in the first numerical simulation of the test case entire domain, performed on a computational grid with 63 452 nodes, the flame blows off because at the inlet way out the flow field isn't well predicted.

A second numerical simulation, performed only on the anchoring zone (a domain with $r_{max} = 1.5\,cm$ and $z_{max} = 2\,cm$), with a computational grid of 206 349 nodes (that permit to obtain a 1.0×10^{-5} m spatial resolution close to the nozzle), allow to underline the vortex shedding phenomena that occur on the duct
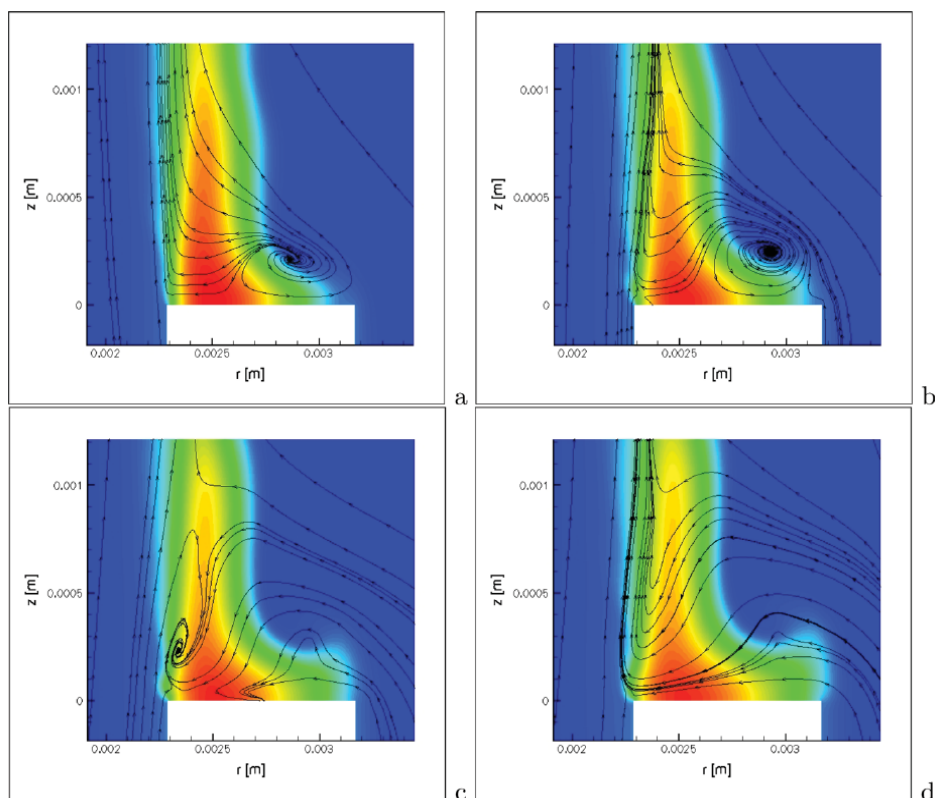
FIGURE 1.5. Temperature contours, details of the shedding and flame anchoring

wall and that permit a stable flame anchoring, as can be seen in figure 1.5 on the following page.

So is clear that in this test case, where there's a big difference between the total length of the domain and the wall thickness, with a structured grid is impossible to obtain a satisfactory compromise between total number of nodes and adequate spatial resolution: a mesh refinement technique can overcome this limitation, because it makes possible to use a grid with an high spatial resolution in a well enclosed zone and to restrict the number of grid nodes in the remaining part of the domain. A mesh refinement technique, is also very useful in combination with Immersed Volume Method (IVM) technique, already implemented in HeaRT numerical code and successfully validated [Cecere and Giacomazzi, 2014].

1.5 State of The Art

In the past years, a lot of attention has been addressed to the development of multi resolution methods for a large set of numerical simulation, from shock hydrodynamics to climate studies; with this techniques, is possible to obtain a better numerical solution and in characteristic situations also to obtain a decrease of computational costs and a reduction of numerical simulation times.

Berger [Berger and Colella, 1989] developed a two dimensional adaptive mesh refinement strategy for solving hyperbolic conservation laws: by the mean of an error estimation procedure, new refined grid levels are introduced in field zones where an higher spatial resolution is necessary; the communication between different grid levels is obtained with bilinear interpolation (from coarse to fine) and with a weighted sum over fine cells (from fine to coarse).

In [Boersma et al., 1997] is described a numerical algorithm for local grid refinement in Large Eddy Simulation of incompressible flows: the communication from coarse to fine is carried out by a multi linear interpolation of coarse values, that is followed by a correction to ensure that the sum of the mass flux through the fine grid cell interfaces of which the union is a coarse grid cell face, equals the original mass flux through this coarse cell interface. The communication from fine to coarse grid is done in two ways: the first is a simple weighted sum over fine cells, while the second is a more complex modification of subgrid terms in the coarse grid equations (following the work of Sullivan [Sullivan et al., 1996]).

Quéméré [Quéméré et al., 2001] developed a multi-resolution method for large eddy simulation of compressible flows on a collocated numerical grid: as the two papers previous described, the fine to coarse communication is an easy weighted sum over the coarse cell volume. The inverse communication (called "enrichment"), seeks to regenerate some high frequencies, evaluated on the fine field from a comparison between the coarse multi linear interpolated flow field and the extrapolated interpolated and weighted summarized fine flow field.

The use of staggered grids complicates grid communication procedures: for an incompressible flow, Qianlong [Qianlong, 2010] proposed a projection method on the overlapping region between coarse and fine zones, based on multi linear interpolation (corrected to verify that the sum of the fine fluxes is equal to the coarse corresponding flux) of the velocity divergence and of the pressure at the interface of the two different resolution zones.

Although the relevance of the topic, to the author's knowledge, there aren't significant studies in literature about multi-resolution techniques developed for a compressible, staggered LES in-house developed code for the numerical simulations of reacting flows.

1.6 STRUCTURE OF THE THESIS

The present Ph. D. dissertation is organized as following:

1. The chapter 1 on page 2 introduces the background of the doctoral research, the main phenomena studies and the motivations of the doctoral research.

2. The chapter 2 on the following page presents the physical models adopted to study turbulent reacting flows; the governing equations are reported here.

3. The chapter 3 on page 23 shows numerical methods used to solve the governing equations adopted.

4. The chapter 4 on page 36 describes the multi-resolution technique developed for HeaRT numerical code: the coupling procedures between coarse

and fine grids are here illustrated, together with the numerical algorithm chosen for the numerical integration of the conservative equations in a multi-resolution domain.

5. The chapter 5 on page 50 reports the results of the first simple numerical test, necessary to verify the formal accuracy of the developed algorithm.

6. The chapter 6 on page 65 presents the results of an hydrogen/methane/air slot flame simulations in multi-resolution computational grids; also a comparison with the numerical results obtained from a numerical simulation on a single-resolution is shown as a validation test.

7. In the chapter 7 on page 94 all the original results of this doctoral research are summarized.

8. The appendix A on page 97 contains the mathematical passages necessary to obtain the governing equations in cylindrical coordinates system.

9. In the appendix B on page 105 there's a brief overview of the multi-resolution code and the future developments expected for the multi-resolution algorithm.

10. The appendix C on page 112 gives some details of the non reflective boundary conditions implemented in the HeaRT numerical code and describes some possible new easier formulations.

2

Governing Equations

I^{N} this chapter the governing equations of the physical model are described. The model adopted is suitable to describe the turbulent flow in modern combustors. However we note that the fluid characterization for combustors does not affect the general treatment of governing equations since these principles describe the mechanical and thermal behaviour of a generic moving fluid.

2.1 Conservation Laws

The governing equations are written in the form of partial differential equations. This form of the governing equations derives directly from the physical principles of flow dynamics:

- conservation of mass;

- conservation of Linear Momentum;

- conservation of energy.

The conservation laws written in this form relate the flow field variables at a point in the flow, as opposed to governing equations written in integral form that deal with a finite space, the control volume.

2.1.0.1 Conservation of Mass

The conservation of mass principle states that, in absence of mass adduction, the variation in time of the density of the flow field in a point is equal to the variation in space of the product between the density and the velocity vector, that is:

$$\frac{\partial \rho}{\partial t} + \nabla \cdot (\rho \mathbf{u}) = 0 \tag{2.1}$$

where ρ is the density of the fluid.

2.1.0.2 CONSERVATION OF MOMENTUM

The conservation of momentum principle states that in absence of external forces the rate of change of linear momentum in a point in the space is equal to the resultant forces on that point, that is:

$$\frac{\partial \rho \mathbf{u}}{\partial t} + \nabla \cdot (\rho \mathbf{u}\mathbf{u}) = -\nabla \cdot \underline{\mathbf{S}} + \rho \sum_{i=1}^{N_s} Y_i \mathbf{f_i} \tag{2.2}$$

where $\underline{\mathbf{S}}$ is the stress tensor, N_s is the number of chemical species, Y_i is the mass fraction of the ith species and f_i is the body force per mass unit acting on the ith species.

2.1.0.3 CONSERVATION OF ENERGY

The conservation of energy principle states that in absence of energy adduction the rate of change of energy in a point in the space is equal to the heat transfer rate and the total work made by the forces acting on that point, that is:

$$\frac{\partial E}{\partial t} + \nabla \cdot (\rho \mathbf{u}E) = \nabla \cdot (\underline{\mathbf{S}}\mathbf{u}) - \nabla \cdot \mathbf{q} + \rho \sum_{i=1}^{N_s} Y_i \mathbf{f_i} \cdot (\mathbf{u} + \mathbf{V_i}) \tag{2.3}$$

where E is the total energy (internal and kinetic), $\mathbf{q}$ is the heat transfer rate and $\mathbf{V_i}$ is the diffusion velocity of the ith chemical species.

2.2 MULTIFLUIDS MODEL

In a chemical reacting and multispecies flow, an additional equation is necessary to complete the flow description: the conservation of species mass fraction; this principle states that the rate of accumulus of the ith species depends on the convective flux, the diffusive flux and the production (or destruction) rate of the species due to the chemical reactions, that is:

$$\frac{\partial \rho Y_i}{\partial t} + \nabla \cdot (\rho \mathbf{u}Y_i) = -\nabla \cdot \mathbf{J_i} + \rho \dot{\omega}_i \tag{2.4}$$

where $\mathbf{J_i}$ is the diffusive mass flux and $\dot{\omega}_i$ is the production – destruction rate of the ith species.

The last equation used is the thermodynamic state equation that states a relation between the pressure, the density and the temperature of an ideal gas, that is:

$$p = \rho \sum_{i=1}^{N_s} \frac{Y_i}{W_i} \mathcal{R}_u T \tag{2.5}$$

where W_i is the molecular weight of the ith species, $\mathcal{R}_u$ is the universal gas constant, T is the temperature and p is the pressure of the fluid.

The summation of all species transport equations (2.4) yields the conservation of mass equation (2.1): therefore the N_s species mass fraction conservation and mass transport equation are linearly dependent and one of them is redundant. Furthermore, to be consistent with mass conservation, the diffusion fluxes ($J_i = \rho Y_i V_i$) and the chemical source terms must satisfy:

$$\sum_{i=1}^{N_s} J_i = 0 \quad \text{and} \quad \sum_{i=1}^{N_s} \dot{\omega}_i = 0 \tag{2.6}$$

2.3 Chemical Kinetic Mechanisms

Combustion of hydrocarbons contains hundreds of reactions for simple hydrocarbons such as CH_4, thousands of reactions for larger hydrocarbons. The interaction of these elementary reactions governs the whole reaction mechanism. Even though there are large amount of reactions, they have characteristic properties which will be explained further.

2.3.1 Detailed (Skeletal) Mechanism

Detailed mechanisms consist of hundreds of species and from hundreds to thousands of reactions. These mechanisms contain all the important species and elementary reactions. They also contain as much as possible fundamental information.

Generation of reaction mechanisms starts with the estimation of necessary species and reactions which are likely to occur in the observed conditions: reactants, large number of intermediate species and products must be included in the mechanism. Increasing databases of rate parameters of elementary reactions enable to create more detailed "complete" mechanisms which have more complex structures.

The development of detailed mechanisms is time-consuming and iterative, also because validation against experimental data is necessary.

The above detailed mechanism generation is so complex and there may always exist human errors: in order to automate this challenging process, computers have become to play an important role in the last two decades.

After the mechanism is constructed and rate parameters are incorporated, differential rate equations are integrated.

The problem of the simulation of such detailed mechanisms is "stiffness" of the mechanism, which increases the computation time; elementary reactions occur in a reaction mechanism in different time scales: the ratio of fastest time scale to slowest time scale is the stiffness of the system. Because of stiffness, too small time steps are necessary to achieve stability and using standard integration methods such as Runge-Kutta method become inapplicable in detailed mechanisms.

2.3.2 Reduced (Skeletal) Mechanism

Applying detailed reaction mechanisms in CFD applications, and making a detailed investigation on these mechanisms require too much computational time. Coupling physical processes such as transport phenomena in the flow field with the chemical kinetics makes the systems even more complicated to solve.

Some species and reactions in the detailed reaction mechanism have a negligible influence on the combustion process: these species can be defined as redundant. Removing redundant species from the detailed mechanism does not give considerable error on the calculations such as mole fractions of species. These species and reactions are defined by the mechanism simplifying technique adopted: sensitivity analysis, necessity analysis, direct relation graph, etc. . . .

For instance, applying a necessity analysis allows deleting up to 55% of all species from the detailed mechanism.

2.3.3 Global (Reduced) Mechanism

The approaches to generate reduced mechanisms can be classified in to two different categories: static and dynamic approaches. Static approaches are analyses such as reaction flow analysis and sensitivity analysis: sensitivity analysis gives the reactions and species with high sensitivities and defines them as non-redundant, which cannot be removed from the detailed reaction mechanism.

After adding fuel, oxidizer, and products to this non-redundant list, reaction flow analysis gives the atomic mass flow through the given reactions. This is used to detect redundant species that are considered unimportant for the mechanism, due to small amounts of formation and destruction, for differently defined levels of mass flow.

Dynamic approaches take a detailed or skeletal mechanism as reference and then select only the most important species and reactions for the reduced mechanism. Reduced mechanisms can be generated by applying the steady state assumptions to a detailed or skeletal mechanism without any significant loss of accuracy. A measure of species lifetimes is taken from the diagonal elements of the Jacobian matrix of the chemical source terms: the species with a lifetime shorter than and mass fraction below specified limits are assumed to be in steady state and selected for removal from the skeletal or detailed mechanism; these schemes are anyway computationally expensive, since to evaluate global reactions rate they require solving an algebraic-differential system of equations.

Solving such a non-linear algebraic system of equations (generally via iterations) is also a negative critical issue in supercomputing since inevitably produces load unbalancing (e.g., processors solving non-reacting portion of a fluid will have to wait processors solving reacting portions).

2.3.4 Fast Chemistry

The simplest mechanism is the fast chemistry, that is based on a very basic approach: when fuel and oxidizer are mixed together, they burn, so there isn't need of any kinetic information.

2.4 Constitutive Equations

Each material has a different response to an external force, depending on the properties of the material itself: the constitutive equations describe this behaviour.

In particular, they express with simple mathematical models the microscopic molecular diffusion of momentum, energy and mass. For a gas mixture, they should model the stress – strain relation between **S** and **E**, the heat flux **q** and the species mass flux $\mathbf{J}_i$.

2.4.1 The Diffusive Momentum Flux

For all gases that can be treated as continuum it has been observed a linear proportion between viscous stresses that arise from the flow and the local strain rate: that is equivalent to saying that those forces are proportional to the rates of change of the fluid's velocity vector as one moves away from the point in question in various directions; a fluid that behaves in this manner is called Newtonian fluid. With this assumption is possible to derive an expression that relates the stress tensor **S** to the pressure p, the strain rate **E** and the velocity vector **u**, that is:

$$\mathbf{S} = \left(-p + \lambda \boldsymbol{\nabla} \cdot \mathbf{u}\right) \mathbf{I} + 2\mu \mathbf{E} = -p\mathbf{I} + \boldsymbol{\tau} \tag{2.7}$$

where τ is the viscous part of stress tensor, μ is the coefficient of viscosity and λ is the second coefficient of viscosity. These two coefficient of viscosity are related to the coefficient of bulk viscosity μ_b by the $\mu_b = -2/3\mu + \lambda$; with the assumption of the Stoke hypothesis (the sum of the normal stresses is zero), $\mu_b = 0$, so $\lambda = 2/3\mu$ and the viscous stress tensor becomes:

$$\tau_{ij} = \lambda \frac{\partial u_i}{\partial x_i} + 2\mu \left[\frac{1}{2} \left(\frac{\partial u_i}{\partial x_j} + \frac{\partial u_j}{\partial x_i} \right) \right] \tag{2.8}$$

Pressure at the macroscopic level corresponds to the microscopic transport of momentum by means of molecular collisions in the direction of molecules motion. Instead, molecular momentum transport in other directions is what at macroscopic level is called viscosity. They are of different nature, because in terms of work done, when continuous distribution are considered, pressure produces reversible transformations (changes of volume), while viscous stresses produce irreversible transformations (dissipation of energy into heat).

2.4.2 The Diffusive Species Mass Flux

In equation (2.4) the knowledge of diffusive species mass flux $\mathbf{J}_i$ is required: this flux expresses the relative motion of chemical species with respect to the motion of their (moving) center of mass; by the means of a constitutive law this motion can be expressed without an additional momentum equation for chemical species. Both modelling and calculation of individual species diffusive mass flux is not easy; the distribution of N_s chemical species in a multicomponent gaseous mixture is rigorously obtained by the means of kinetic theory [Kuo, 1986]:

$$\nabla X_i = \underbrace{\sum_{i=1,i\neq j}^{N_s} \frac{X_i X_j}{D_{ij}} \left(\mathbf{V}_j - \mathbf{V}_i\right)}_{DV} + \underbrace{(Y_i - X_i)\frac{\nabla p}{p}}_{PG} + \underbrace{\frac{\rho}{p}\sum_{j=1}^{N_s} Y_i Y_j \left(\mathbf{f}_i - \mathbf{f}_j\right)}_{BF}$$
$$+ \underbrace{\sum_{j=1}^{N_s} \frac{X_i X_j}{\rho D_{ij}} \left(\frac{\alpha_j}{Y_j} - \frac{\alpha_i}{Y_i}\right)\frac{\nabla T}{T}}_{SG} \tag{2.9}$$

where D_{ij} is the binary diffusion coefficient of species i into the species j, X_j and Y_j are the molar and the mass fraction of the jth species respectively, $\mathbf{f}_j$ the body force per unit mass, acting on species j, α_j the thermo-diffusion coefficient of species j.

Equations (2.9) are referred to as the Maxwell-Stefan equations, since Maxwell [Maxwell, 1860a,b] suggested them for binary mixtures on the basis of kinetic theory, and Stefan [Stefan, 1871] generalized them to describe the diffusion in a gas mixture with N_s species.

The main feature of equations (2.9) is that they couple inextricably all diffusion velocities $\mathbf{V}_j$ (and thus all fluxes), to all concentrations X_j and Y_j and their gradients. According to equations 2.9, concentrations gradients can be physically created by:

- differences in Diffusion Velocities (DV);

- Pressure Gradients (PG);

- differences in Body Forces (BF) per unit mass acting on molecules of different species;

- thermo-diffusion, or Soret Effect (SE), i.e., mass diffusion due to temperature gradients, driving light species towards hot regions of the flow; this last effect, often neglected, is nevertheless known to be important, in particular for hydrogen combustion, and in general when very light species play an important role.

The linear system of equations (2.9) for the variable $\mathbf{V}_j$ has size $N_s \times N_s$ and requires knowledge of $Ns(Ns-1)/2$ diffusivities. Only $N_s - 1$ equations are independent, since the sum of all diffusion fluxes must be zero. This system must be solved in each direction of the frame of reference (coordinate system), at every computational node and, for unsteady flows, at each time step of numerical integration.

Extracting the diffusion velocities is a very difficult task, therefore in many CFD computations simplified models are preferred; in the present dissertation, Hirschfelder and Curtiss law is used to calculate diffusion velocities in an approximate way:

$$\mathbf{V}_i = -D_i \frac{\nabla X_i}{X_i} \tag{2.10}$$

where

$$D_i = \frac{1 - Y_i}{\sum_{j=1, j \neq i}^{N_s} \frac{X_j}{D_{ji}}} \tag{2.11}$$

The coefficient D_i is an equivalent diffusion coefficient of species i into the whole remaining mixture of $N_s - 1$ species.

When approximated expressions (like Hirschfelder and Curtiss law) are used to obtain diffusion velocities, mass conservation problems can occur: in fact the diffusion velocities do not necessarily satisfy the constrain

$$\sum_{i=1}^{N_s} \mathbf{J}_i = \sum_{i=1}^{N_s} \rho Y_i \mathbf{V}_i = 0$$

A simple empirical remedy to impose global mass conservation consists in subtracting any residual artificial diffusional velocity from the flow velocity in the species transport equations. In fact, summing all species transport equations, the mass conservation equation must be obtained, while it is found:

$$\frac{\partial \rho}{\partial t} + \nabla \cdot (\rho \mathbf{u}) = -\nabla \cdot (\rho \sum_{i=1}^{N_s} Y_i \mathbf{V}_i) \tag{2.12}$$

Thus, in order for the conservation of mass to be respected, a term $\rho_f \mathbf{V}^c$ involving a correction velocity $\mathbf{V}^c$ must be introduced. $\mathbf{V}^c$ is defined as

$$\mathbf{V}^c = -\sum_{i=1}^{N_s} Y_i \mathbf{V}_i$$

and assuming Hirschfelder's law holds, it becomes

$$\mathbf{V}^c = \sum_{i=1}^{N_s} \frac{W_i}{W_{mix}} D_i \nabla X_i \tag{2.13}$$

The correction velocity must be computed at each time step and added to the flow velocity in the species convective term. The corrected convective term of species transport equations must then become

$$\nabla(\rho_f \mathbf{u}_f Y_i) \rightarrow \nabla(\rho_f (\mathbf{u}_f + \mathbf{V}^c) Y_i) \tag{2.14}$$

With this "trick", any artificial flow due to the nonzero diffusional mass flux is thereby cancelled. Furthermore, the constrain $\sum_{i=1}^{N_s} Y_i = 1$ is strictly ensured by the

$$Y_i = \frac{Y_i}{\sum_{i=1}^{N_s} Y_i} (1 - Y_i) + Y_i \tag{2.15}$$

2.4.3 The Diffusive Heat Flux

The heat flux $\mathbf{q}$ for a gaseous mixture of N_s chemical species can be split in three contributions:

1. the heat transfered by conduction, modeled by the Fourier's law; at a microscopic level, this flux is due to molecular collision: molecules with an higher level of kinetic energy (with higher temperature) transfer energy by molecular collision to the ones with a lower level of kinetic energy (with a lower temperature); in the continuum view, the heat flux arises from temperature gradients;

2. the heat transfered by molecular diffusion in a multi–species mixture, due to concentration gradients; when $\nabla Y_i \neq 0$, each species diffuses with its own velocity V_i; this means that can be energy transfer even in a gas at uniform temperature or in a rarefied gas (where conduction is negligible);

3. the heat transfered by Dufour effect: the Onsager principle of microscopic reversibility in the thermodynamics of irreversible processes implies that if temperature gradients cause species diffusion (thermo-diffusive or Soret effect), concentration gradients must cause a reciprocal (Dufour effect) heat flux; the Dufour effect is neglected [Kuo, 1986].

The total heat flux $\mathbf{q} = \mathbf{q}_F + \mathbf{q}_{V_i} + \mathbf{q}_D$, where $\mathbf{q}_D$ is the thermal flux due to Dufour effect (neglected) is:

$$\mathbf{q} = -k\nabla T + \rho \sum_{i=1}^{N_s} \mathcal{H}_i Y_i \mathbf{V}_i \tag{2.16}$$

where k is the thermal conductivity and $\mathcal{H}_i$ is the enthalpy of the ith species.

2.5 LES Model

Large eddy simulations are based on the assumption that small-scale turbulent eddies are more isotropic than the large ones, and are responsible mostly for energy dissipation in the mean. Modelling the small scales, while resolving the large eddies, may be very beneficial: first, since most of the momentum transport is due to the large eddies, model inaccuracies are less critical; secondly, the modelling of the unresolved scales is easier, since they tend to be more homogeneous and isotropic than the large ones, which depend on the boundary conditions.

Thus, LES is based on the use of a filtering operation: a filtered (or resolved) large-scale variable is defined by:

$$\bar{f}(\mathbf{x}) = \int_D f(\mathbf{x}') G(\mathbf{x}, \mathbf{x}', \overline{\Delta}) \, d\mathbf{x}' \tag{2.17}$$

where D is the entire domain and G is the filter function. The size of the smallest eddies that are resolved in LES is clearly related to the filter width, denoted by $\overline{\Delta}$: the grid spacing h should be sufficiently fine to represent accurately eddies of size $\overline{\Delta}$. There has been considerable discussion on the appropriate value

of filter width; in most cases, the filter width is chosen proportional to the grid size ($\overline{\Delta} = nh$), but if the mesh is anisotropic, an appropriate average is used to determine h:

$$h = (h_x h_y h_z)^{1/3} \quad \text{or} \quad h = \left(h_x^2 + h_y^2 + h_z^2\right) \tag{2.18}$$

When complex geometries are studied, is preferable relating the filter width to physical quantities, rather than the grid. The most commonly used filter function are the sharp Fourier cutoff filter, defined in the wave space, that is:

$$\widehat{G}(k) = \begin{cases} 1, & \text{if } k \leqslant \pi/\overline{\Delta} \\ 0, & \text{otherwise} \end{cases} \tag{2.19}$$

the Gaussian filter in the physical space, that is:

$$G(\mathbf{x}) = \sqrt{\frac{6}{\pi\overline{\Delta}^2}} \exp\left(-\frac{6\mathbf{x}^2}{\overline{\Delta}^2}\right) \tag{2.20}$$

and the top hat filter in physical space, that is

$$G(\mathbf{x}) = \begin{cases} 1/\overline{\Delta}, & \text{if } |\mathbf{x}| \leqslant \overline{\Delta}/2 \\ 0, & \text{otherwise} \end{cases} \tag{2.21}$$

In this work, the filter operation is implicitly defined by the mesh size. The uncertainties related to the procedure of exchanging the order of the filter and differential operators (commutation errors), are neglected and assumed to be incorporated in the sub-grid scale modeling.

2.5.1 Filtered Conservation Equations

In compressible flows, it is convenient to use Favre-filtering to avoid the introduction of subgrid-scale terms in the equation of conservation of mass: when the mass balance equation is averaged (with this operation a generic variable ϕ is split into a mean value $\overline{\phi}$ and a deviation from the mean denoted by ϕ'), indeed, velocity/density fluctuation correlation appears; to avoid the explicit modelling of such correlation, a Favre average is introduced: a Favre-filtered variable is defined by the

$$\widetilde{f} = \frac{\overline{\rho f}}{\overline{\rho}} \tag{2.22}$$

The Favre-filtered equations of motion can be written in the form:

$$\frac{\partial \overline{\rho}}{\partial t} + \frac{\partial \left(\overline{\rho} \widetilde{u}_j \right)}{\partial x_j} = 0 \tag{2.23}$$

$$\frac{\partial \left(\overline{\rho} \widetilde{u}_j \right)}{\partial t} + \frac{\partial \left(\overline{\rho} \widetilde{u}_i \widetilde{u}_j \right)}{\partial x_j} = -\frac{\partial \overline{p}}{\partial x_i} + \frac{\partial \overline{\tau}_{ji}}{\partial x_j} - \frac{\partial \tau_{ji}^{SGS}}{\partial x_j} + \overline{\rho} \sum_{i=1}^{N_s} \widetilde{Y_i \mathbf{f}_i} \tag{2.24}$$

$$\frac{\partial \left(\overline{\rho} \widetilde{\mathcal{H}} \right)}{\partial t} + \frac{\partial \overline{\rho} \widetilde{\mathcal{H} u}}{\partial x_j} = \frac{D\overline{p}}{Dt} - \frac{\partial \left(\overline{q}_j + q_j^{SGS} \right)}{\partial x_j} + \overline{\rho} \sum_{i=1}^{N_s} \widetilde{Y}_i \widetilde{f}_{ij} \widetilde{V}_{ij} \tag{2.25}$$

where

$$\overline{\tau}_{ij} = \overline{\mu} \left(\frac{\partial \widetilde{u}_i}{\partial x_j} + \frac{\partial \widetilde{u}_j}{\partial x_i} \right) - \frac{2}{3} \overline{\mu} \delta_{ij} \frac{\partial \widetilde{u}_k}{\partial k}$$

and

$$\tau_{ij}^{SGS} = \overline{\rho \widetilde{u_i u_j}} - \overline{\rho} \widetilde{u}_i \widetilde{u}_j \tag{2.26}$$

$$q_j^{SGS} = \overline{\rho \widetilde{\mathcal{H} u_j}} - \overline{\rho} \widetilde{\mathcal{H}} \widetilde{u}_j \tag{2.27}$$

The subgrid-scale heat flux due to diffusion effects has been considered negligible with respect to SGS heat flux q_{ij}^{SGS}.

The Favre-filtered equations of species and state can be written in the form:

$$\frac{\partial \left(\overline{\rho} \widetilde{Y}_i \right)}{\partial t} + \frac{\partial \left(\overline{\rho \widetilde{Y}_i \widetilde{V}_{ij}} \right)}{\partial x_j} = -\frac{\partial \left(\overline{\rho} \widetilde{Y}_i \widetilde{V}_{ij} \right)}{\partial x_j} + \overline{\rho} \widetilde{\omega} - \frac{\partial J_{ij}^{SGS}}{\partial x_j} \tag{2.28}$$

$$\overline{p} = \overline{\rho} \sum_{i=1}^{N_s} \mathcal{R}_u \widetilde{\frac{Y_i}{W_i}} T \tag{2.29}$$

where

$$J_{ij}^{SGS} = \overline{\rho \widetilde{Y_i u_j}} - \overline{\rho \widetilde{Y}_i \widetilde{u}_j} \tag{2.30}$$

Also in this case, the subgrid-scale effects due to diffusion, arising from $\widetilde{J}_{ij}$, may be neglected with respect to SGS species transport $\mathbf{J}_i^{SGS}$.

2.5.2 Subgrid-scale Modelling

The main role of subgrid-scale model must be to remove energy from the resolved scales, mimicking the drain that is usually associated with the energy cascade. It may not be necessary for a model to represent the "exact" SGS stresses accurately at each point in space and time, but only to account for their global effect; the resolved scales exchange energy with the unresolved scales and the surroundings through several mechanisms.

In the Fractal Model (FM), the eddy viscosity (that has to dissipate energy from the resolved scales) is given by:

$$\mu_T = \frac{1}{\pi}\mu_\Delta \left[\left(\frac{\Delta}{\eta}\right)^2 - 1\right] \tag{2.31}$$

where Δ is the characteristic cell dimension (for example the cube root of the cell volume), η is the dimension of the dissipative scale and μ_Δ is the viscosity value in the cell; this expression yields automatically $\mu_T = 0$ when $\Delta/\eta = 1$ (i. e. in laminar regions and in particular at walls), or when the computational cell Reynolds turbulent number is of order 1.

In this equation, Δ/η is related to the local turbulent Reynolds number based on the local filter size and a velocity fluctuation $u'_\Delta = (2/3k^{sgs})^{1/2}$: so in each computational cell the value of subgrid kinetic energy is required.

This value is obtained from a transport equation of k^{sgs}, defined as $k^{sgs} = \frac{1}{2}(\widetilde{u_i^2} - \widetilde{u}_i^2)$:

$$\begin{aligned}
\frac{\partial(\overline{\rho}k^{sgs})}{\partial t} + \frac{\partial(\overline{\rho}\widetilde{u}_i k^{sgs})}{\partial x_i} = &-\overline{\rho}c_\epsilon \frac{(k^{sgs})^{3/2}}{\Delta} + \tau_{ij}^{sgs}\frac{\partial(\widetilde{u}_j)}{\partial x_i} \\
&+ \frac{\partial\left[(\mu+\mu_t)\frac{\partial k^{sgs}}{\partial x_i}\right]}{\partial x_i} + \frac{\partial\left(\frac{\mu_t \widetilde{R}}{Pr_t}\frac{\partial \widetilde{T}}{\partial x_i}\right)}{\partial x_i}
\end{aligned} \tag{2.32}$$

where the terms on the right hand side are, respectively:

- dissipation of subgrid kinetic energy;

- subgrid stress work;

- diffusion due to subgrid pressure fluctuations in kinetic energy;

- k^{sgs} diffusion due to subgrid pressure fluctuations modelled adopting an eddy-viscosity assumption.

The coefficient c_ϵ is assumed constant (and set to 0.916). Once the turbulent viscosity is known, the subgrid stresses τ_{ij}^{sgs} can be modelled as:

$$\tau_{ij}^{sgs} = 2\mu_t\left(\widetilde{S}_{ij} - \frac{1}{3}\widetilde{S}_{kk}\delta_{ij}\right) - \frac{2}{3}\overline{\rho}k^{sgs}\delta_{ij} \tag{2.33}$$

The subgrid heat flux can be modelled as:

$$q_j^{sgs} = -\alpha_T\nabla H \tag{2.34}$$

where $\alpha_T = \frac{\mu_T}{\rho Pr_T}$ and the subgrid diffusive flux can be modelled as:

$$J_{ij}^{SGS} = -D_T\nabla Y_i \tag{2.35}$$

where $D_T = \frac{\nu_T}{Sc_T}$.

2.5.3 LTSM Model

The Favre filtered chemical source term in the energy and single species transport equation is here modelled as

$$\widetilde{\omega_i} \simeq \gamma^* \omega_i^*$$

where γ^* is the local reacting volume fraction of the computational cell and ω_i^* is the reaction rate of the ith chemical species.

The local reacting volume fraction is defined as

$$\gamma^* = \frac{\mathcal{V}_{\mathcal{F}}^*}{\mathcal{V}_\Delta}$$

where $\mathcal{V}_{\mathcal{F}}^*$ is the reacting volume and $\mathcal{V}_\Delta$ is the total volume of the computational cell.

The Localized Turbulent Scales Model (LTSM) is developed under the following two assumptions:

- within a wrinkled flame front the iso-surfaces of the progress variables are parallel;

- the ratio between the turbulent and the laminar flame surface areas scales as the ratio between the associated flame speeds, that is:

$$\mathcal{A}_{\mathcal{F}}/\mathcal{A}_{\mathcal{L}} \equiv \mathcal{A}_{\mathcal{T}}/\mathcal{A}_{\mathcal{L}} \approx \mathcal{S}_{\mathcal{T}}/\mathcal{S}_{\mathcal{L}}$$

This model estimates the value of γ^* assuming that a flame front having a surface area $\mathcal{A}_{\mathcal{F}}$ and thickness $\delta_{\mathcal{F}}$ is contained in a computational cell volume of characteristic size $\Delta = \mathcal{V}_\Delta^{1/3}$

$$\gamma^* = \frac{\mathcal{V}_{\mathcal{F}}^*}{\mathcal{V}_\Delta} \approx \frac{\mathcal{A}\delta_{\mathcal{F}}}{\mathcal{V}_\Delta} \approx \frac{\mathcal{S}_{\mathcal{T}}}{\mathcal{S}_{\mathcal{L}}}\mathcal{A}_{\mathcal{L}}\frac{\delta_{\mathcal{F}}}{\mathcal{V}_\Delta} \approx \frac{\mathcal{S}_{\mathcal{T}}}{\mathcal{S}_{\mathcal{L}}}\Delta^2\frac{\delta_{\mathcal{F}}}{\Delta^3} = \frac{\mathcal{S}_{\mathcal{T}}}{\mathcal{S}_{\mathcal{L}}}\frac{\delta_{\mathcal{F}}}{\Delta} \qquad (2.36)$$

So the problem of γ^* estimation becomes the problem of estimating the characteristic of the local flame front in terms of its turbulent flame speed, laminar flame speed and thickness (turbulent or laminar) from the filtered conditions of the flow and depending on the related local premixed combustion regime.

Introducing an extinction or flame stretch factor $\mathcal{G}_{ext} \leqslant 1$, γ^* can be finally evaluated from the:

$$\gamma^* = \mathcal{G}_{ext}\frac{\mathcal{S}_{\mathcal{T}}}{\mathcal{S}_{\mathcal{L}}}\frac{\delta_{\mathcal{F}}}{\Delta} \qquad (2.37)$$

When $\mathcal{G}_{ext} = 1$ at subgrid level does not imply that stretching is not experienced by the flame at all: it means that the subgrid turbulence is very weak and so it doesn't effectively stretch the subgrid flamelets, but the resolved velocity fluctuations may be high enough to effectively stretch the resolved flame front.

The model used to predict quenching is the so called *quenching cascade model* [Meneveau and Poinsot, 1991], that compares quite well with experimental and direct numerical simulation data on quenching.

3

Numerical Methods

I<small>N</small> this chapter the numerical methods used to integrate the governing equations presented in chapter 2 on page 11 are presented. The methods adopted can be considered at the state of the art for LES of compressible reacting flows.

3.1 Numerical Schemes

In the HeaRT code, described in detail in section 3.2 on page 30 are used the following numerical schemes and methods:

1. AUSM numerical scheme combined with quadratic upstream interpolation developed for the QUICK numerical scheme;

2. finite difference numerical scheme;

3. Newton-Raphson method;

4. Runge-Kutta method.

3.1.1 AUSM Numerical Scheme

The develop of this numerical scheme was motivated by the desire to combine the efficiency of FVS and the accuracy of FDS [Liou and Steffen, 1993]. Considering the two-dimensional system of Euler equation for a perfect gas

$$\frac{\partial \mathbf{U}}{\partial t} + \frac{\partial \mathbf{F}}{\partial x} + \frac{\partial \mathbf{G}}{\partial y} = 0 \tag{3.1}$$

where the inviscid flux vector $\mathbf{F}$ consists of two physically distinct parts, namely convective and pressure terms:

$$\mathbf{F} = \begin{pmatrix} \rho \\ \rho u \\ \rho v \\ \rho H \end{pmatrix} u + \begin{pmatrix} 0 \\ p \\ 0 \\ 0 \end{pmatrix} = F^{(c)} + \begin{pmatrix} 0 \\ p \\ 0 \\ 0 \end{pmatrix} \tag{3.2}$$

The convective terms can now be considered as a passive scalar quantities convected by a velocity u at the cell interface: the pressure flux terms are governed by the acoustic wave speed. So the two components can be discretized separately: at an interface $L < 1/2 < R$ the convective terms can be written as:

$$\mathbf{F}^{(c)}_{1/2} = u_{1/2} \begin{pmatrix} \rho \\ \rho u \\ \rho v \\ \rho H \end{pmatrix}_{L/R} = M_{1/2} \begin{pmatrix} \rho a \\ \rho a u \\ \rho a v \\ \rho a H \end{pmatrix}_{L/R} \tag{3.3}$$

where

$$(\bullet)_{L/R} = \begin{cases} (\bullet)_L & \text{if} \quad M_{1/2} \geqslant 0 \\ (\bullet)_R & \text{otherwise} \end{cases} \tag{3.4}$$

The advective velocity $M_{1/2}$ can be expressed as a combination of the wave speeds $(M \pm 1)$ traveling towards the interface $\left(\frac{1}{2}\right)$ from the adjacent L and R cells:

$$M_{1/2} = M^+_L + M^-_R \tag{3.5}$$

where the split Mach number $M^\pm$ is defined according Van Leer splitting:

$$M^\pm = \begin{cases} \pm\frac{1}{4}(M \pm 1)^2 & \text{if} \quad |M| \leqslant 1 \\ \frac{1}{2}(M \pm |M|) & \text{otherwise} \end{cases} \tag{3.6}$$

The pressure term can be written, following equation (3.5):

$$p_{1/2} = p^+_L + p^-_R \tag{3.7}$$

and the pressure splitting is weighted using the polynomial expansion of the characteristic speeds $(M \pm 1)$. The pressure splitting can be expressed in terms of first order polynomials $(M \pm 1)$:

$$p^\pm = \begin{cases} \frac{p}{2}(1 \pm M) & \text{if} \quad |M| \leqslant 1 \\ \frac{p}{2}(M \pm |M|)/M & \text{otherwise} \end{cases} \tag{3.8}$$

or in terms of second order polynomials $(M \pm 1)^2$:

$$p^\pm = \begin{cases} \frac{p}{4}(M \pm 1)^2(2 \mp M) & \text{if} \quad |M| \leqslant 1 \\ \frac{p}{2}(M \pm |M|)/M & \text{otherwise} \end{cases} \tag{3.9}$$

All the above formulas can be recast in the form:

$$
\begin{pmatrix} \rho u \\ \rho u u + p \\ \rho u v \\ \rho u H \end{pmatrix}_{1/2} = M_{1/2} \frac{1}{2} \left[\begin{pmatrix} \rho a \\ \rho a u \\ \rho a v \\ \rho a H \end{pmatrix}_L + \begin{pmatrix} \rho a \\ \rho a u \\ \rho a v \\ \rho a H \end{pmatrix}_R \right]
$$

$$
- \frac{1}{2} \left| M_{1/2} \right| \Delta_{1/2} \begin{pmatrix} \rho a \\ \rho a u \\ \rho a v \\ \rho a H \end{pmatrix} \tag{3.10}
$$

$$
+ \begin{pmatrix} 0 \\ p_L^+ + p_R^- \\ 0 \\ 0 \end{pmatrix}
$$

where $\Delta_{1/2}\{\bullet\} = \{\bullet\}_R - \{\bullet\}_L$. The first term on the right hand side is a Mach-number-weighted average of L and R states; the second term is the numerical dissipation.

Summarizing, this numerical scheme (AUSM - Advection Upstream Splitting Method) treats the convective and the pressure terms separately:

- convective terms are biased from the upstream using a properly definite cell-interface velocity;

- pressure term is dealt with convective terms using acoustic waves.

3.1.1.1 QUICK RECONSTRUCTION

In HeaRT code, "L" and "R" convective terms of equation (3.10) are evaluated by the mean of a quadratic upstream interpolation developed in the QUICK (QUadratic Interpolation for Convective Kinetics) numerical scheme [Leonard, 1979]; the method can be expressed as a linear interpolation corrected by a term proportional to the upstream-weighted curvature (see figure 3.1 on the following page):

$$
\begin{aligned}
\phi_l^* &= \frac{1}{2}\left(\phi_L + \phi_C\right) - \frac{\Delta x_l^2}{8}\frac{1}{\Delta x_L}\left(\frac{\phi_C - \phi_L}{\Delta x_l} - \frac{\phi_L - \phi_{FL}}{\Delta x_{fl}}\right) \\
\phi_r^* &= \frac{1}{2}\left(\phi_C + \phi_R\right) - \frac{\Delta x_r^2}{8}\frac{1}{\Delta x_C}\left(\frac{\phi_R - \phi_C}{\Delta x_r} - \frac{\phi_C - \phi_L}{\Delta x_l}\right)
\end{aligned} \tag{3.11}
$$

where subscripts FL, L, C, R and FR refer to the far left, left, central, right and far right nodes; subscripts l and r refer to the left and right faces.

The general formula for the QUICK scheme is the following:
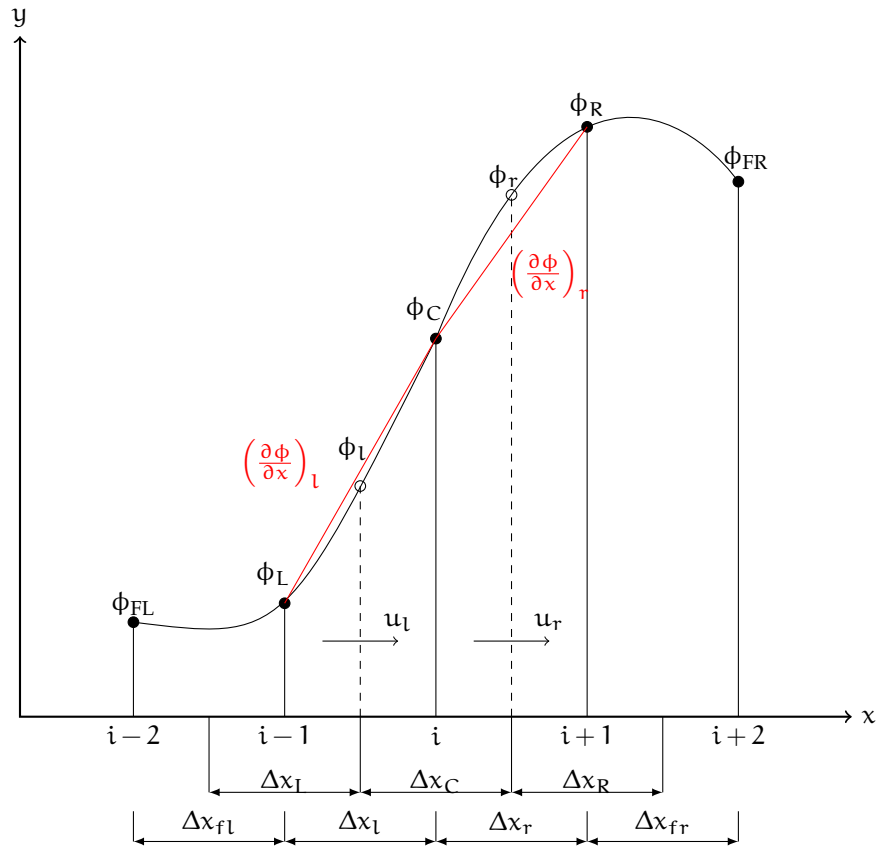
Figure 3.1. Schematic showing a control volume for node i, variables ϕ at upstream and downstream nodes, grid spaces, faces velocities u_* and face gradients $(\partial\phi/\partial x)_*$

$$\phi_l^* = \frac{1}{2}\left(\phi_L + \phi_C\right) - \frac{\Delta x_l^2}{8}Curv_l$$

$$= \frac{1}{2}\left(\phi_L + \phi_C\right) - \frac{\Delta x_l^2}{8}\left[\frac{1}{\Delta x_L}\left(Grad_l - Grad_{fl}\right)\right]$$

$$\phi_r^* = \frac{1}{2}\left(\phi_C + \phi_R\right) - \frac{\Delta x_r^2}{8}Curv_r$$

$$= \frac{1}{2}\left(\phi_C + \phi_R\right) - \frac{\Delta x_r^2}{8}\left[\frac{1}{\Delta x_C}\left(Grad_r - Grad_l\right)\right]$$

(3.12)

where "Curv" represents (upstream-weighted) ϕ curvatures and "Grad" ϕ gradients.

3.1.2 Finite Difference Numerical Scheme

The idea of a finite-difference representation for a derivative can be introduced by recalling the definition of the derivative for the function $u(x, y)$ at $x = x_0$ and $y = y_0$, that is:
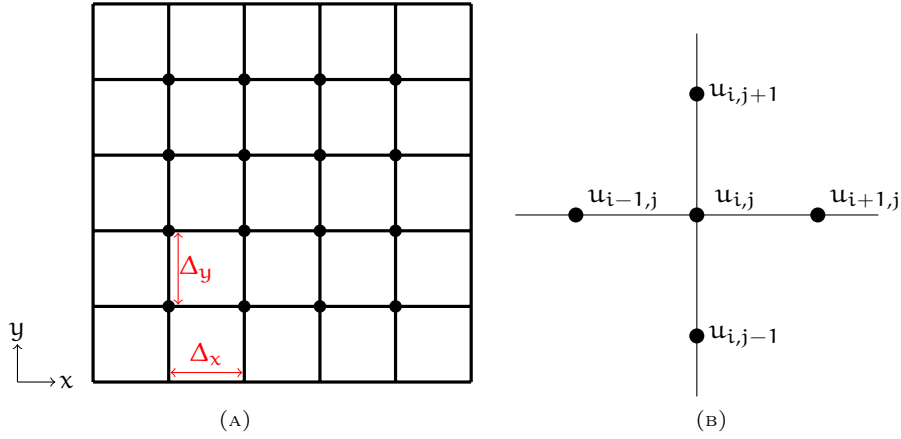
FIGURE 3.2. A typical finite-difference grid

$$\frac{\partial u}{\partial x} = \lim_{\Delta x \to 0} \frac{u\left(x_0 + \Delta x, y_0\right) - u\left(x_0, y_0\right)}{\Delta x}$$

(3.13)

If the function u is continuous and Δx is "sufficiently" small but finite, is expected that $\left[u\left(x_0 + \Delta x, y_0\right) - u\left(x_0, y_0\right)\right]/\Delta x$ will be a good approximation to $\partial u/\partial x$. Developing a Taylor-series expansion for $u\left(x_0 + \Delta x, y_0\right)$ about (x_0, y_0) gives (see figure 3.2)

$$u\left(x_0 + \Delta x, y_0\right) = u\left(x_0, y_0\right) + \left.\frac{\partial u}{\partial x}\right|_0 \Delta x + \left.\frac{\partial^2 u}{\partial x^2}\right|_0 \frac{(\Delta x)^2}{2!} + \ldots$$
$$+ \left.\frac{\partial^{n-1} u}{\partial x^{n-1}}\right|_0 \frac{(\Delta x)^{n-1}}{(n-1)!} + \left.\frac{\partial^n u}{\partial x^n}\right|_\xi \frac{(\Delta x)^n}{n!}$$

(3.14)

where $x_0 \leqslant \xi \leqslant (x_0 + \Delta x)$. Thus we can form the "forward" difference by rearranging equation (3.14), switching to the i, j notation:

$$\left.\frac{\partial u}{\partial x}\right|_{i,j} = \frac{u_{i+1,j} - u_{i,j}}{\Delta x} + \mathcal{O}\left(\Delta x\right) \tag{3.15}$$

An infinite number of difference representations can be found for $\partial u / \partial x|_{i,j}$, for example we could expand "backward":

$$\left.\frac{\partial u}{\partial x}\right|_{i,j} = \frac{u_{i,j} - u_{i-1,j}}{\Delta x} + \mathcal{O}\left(\Delta x\right) \tag{3.16}$$

or subtracting equations (3.15) and (3.16), to obtain the "central" difference:

$$\left.\frac{\partial u}{\partial x}\right|_{i,j} = \frac{u_{i+1,j} - u_{i-1,j}}{2\Delta x} + \mathcal{O}\left(\Delta x\right)^2 \tag{3.17}$$

or adding equations (3.15) and (3.16), to obtain an approximation of the second derivative:

$$\left.\frac{\partial^2 u}{\partial x^2}\right|_{i,j} = \frac{u_{i+1,j} - 2u_{i,j} + u_{i-1,j}}{\left(\Delta x\right)^2} + \mathcal{O}\left(\Delta x\right)^2 \tag{3.18}$$

The mixed derivative approximation can be obtained from the Taylor-series expansion for two variables:

$$
\begin{aligned}
u\left(x_0 + \Delta x, y_0 + \Delta_y\right) = {} & u\left(x_0, y_0\right) + \left(\Delta x \frac{\partial}{\partial x} + \Delta y \frac{\partial}{\partial y}\right) u\left(x_0, y_0\right) + \\
& + \frac{1}{2!}\left(\Delta x \frac{\partial}{\partial x} + \Delta y \frac{\partial}{\partial y}\right)^2 u\left(x_0, y_0\right) + \dots \\
& + \frac{1}{n!}\left(\Delta x \frac{\partial}{\partial x} + \Delta y \frac{\partial}{\partial y}\right)^n u\left(x_0 + \theta \Delta x, y_0 \theta \Delta y\right)
\end{aligned}
\tag{3.19}
$$

where $0 \leqslant \theta \leqslant 1$; rearranging equation (3.19), switching to the i, j notation:

$$\left.\frac{\partial^2 u}{\partial x \partial y}\right|_{i,j} = \frac{1}{\Delta x}\left(\frac{u_{i+1,j} - u_{i+1,j-1}}{\Delta y} - \frac{u_{i,j} - u_{i,j-1}}{\Delta x}\right) + \mathcal{O}\left(\Delta x, \Delta y\right) \tag{3.20}$$

In this manner is possible to obtain all derivatives that appear in Navier-Stokes equations described in chapter 2, for cylindrical and Cartesian structured grids.

3.1.3 NEWTON-RAPHSON METHOD

Newton–Raphson method is a method for finding successively better approximations to the roots (or zeroes) of a real-valued function. Assuming that an initial estimate x_0 is known for the desired root α of $f(x) = 0$, Newton-Raphson method will produce a sequence of iterates which will converge to α. Since x_0 is assumed close to α, the function $f(x)$ can be approximated by constructing its tangent line at $(x_0, f(x_0))$, as can be seen in figure 3.3 on the next page.
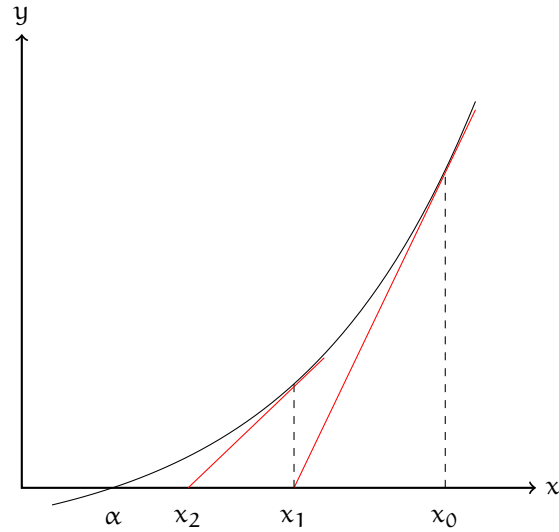
Figure 3.3. Newton's method

Then the root of this tangent line can be used to approximate α, calling this approximation x_1. This process can be repeated to obtain a sequence of iterates x_n with the following iteration formula:

$$x_{n+1} = x_n - \frac{f(x_n)}{f'(x_n)} \quad \text{with} \quad n \geqslant 0 \tag{3.21}$$

Newton-Raphson method can be explained also starting with a Taylor series development: expanding $f(x)$ about x_n:

$$f(x) = f(x_n) + (x - x_n) f'(x_n) + \frac{(x - x_n)^2}{2} f''(\xi) \tag{3.22}$$

with ξ between x and x_n. Letting $x = \alpha$ and using $f(\alpha) = 0$, solving for α we obtain:

$$\alpha = x_n - \frac{f(x_n)}{f'(x_n)} - \frac{(\alpha - x_n)^2}{2} \cdot \frac{f''(\xi_n)}{f'(x_n)} \tag{3.23}$$

with ξ_n between x_n and α. Recalling equation (3.21):

$$\alpha - x_{n+1} = -(\alpha - x_n)^2 \cdot \frac{f''(\xi_n)}{2f'(x_n)} \quad \text{with} \quad n \geqslant 0 \tag{3.24}$$

Using equations (3.23) and (3.24), Newton-Raphson method has a quadratic order of convergence ($p = 2$) in:

$$|\alpha - x_{n+1}| \leqslant c |\alpha - x_n|^p \quad \text{with} \quad n \geqslant 0, c > 0 \tag{3.25}$$

29

3.1.4 Runge-Kutta Method

Runge-Kutta method is a numerical scheme commonly used to solve initial value problems for ODE's. This scheme was developed around 1900 by the German mathematicians C. Runge and M. W. Kutta and essentially utilizes the weighted average of several solutions over the interval Δt in order to improve accuracy of solution. A generic Runge-Kutta scheme can be expressed by the:

$$\begin{cases} u^{n+1} = u^n + h \sum_{i=1}^{s} b_i k_i^n & n = 0, .., N-1 \\ u^0 = u(t_0) \end{cases} \tag{3.26}$$

where

$$h = t^{n+1} - t^n \tag{3.27}$$

$$k_i^n = F\left(t_n + c_i h, u^n + h \sum_{j=1}^{i-1} a_{ij} k_j^n\right) \qquad i = 1, .., s \tag{3.28}$$

$$c_1 = 0 \tag{3.29}$$

$$\sum_{j=1}^{i-1} a_{ij} = c_i \quad \text{for} \quad i = 2, \ldots, s \tag{3.30}$$

and a_{ij}, c_i, b_i are coefficients to be determined and s are the substeps of Runge-Kutta scheme.

3.2 HeaRT Code

Into the chapter we have pointed out that in order to perform a LES numerical simulation of an energy burner, Navier-Stokes conservation laws are suitable. The Navier-Stokes system is the first component of our CFD study: our aim is to find the solution of the Navier-Stokes system (conveniently modified) when the initial and boundary conditions are imposed to it. In this section the numerical model used to find this solution is presented.

HeaRT (Heat Release and Turbulence) numerical code, developed by UTTEI (Technical Unit for Advanced Technologies for Energy and Industry) of ENEA, in collaboration with DIMA (Mechanical and Aerospace Engineering Department) of Sapienza University of Rome, is an unsteady numerical solver for turbulent reacting and non reacting flows, at low Mach number, in three-dimensional cartesian and cylindrical geometries, discretized by the means of structured grids. Navier-Stokes equation are implemented in the compressible formulation, in order to highlight wave propagation phenomena that are very important for combustion instability analysis.

Governing equations are solved, in HeaRT code, on a staggered grid scheme: scalars (density, temperature, pressure, total energy and mass fractions) are set in the cell center, while the three mass fluxes are staggered in space by half grid

(A) Scalars and Mass Fluxes
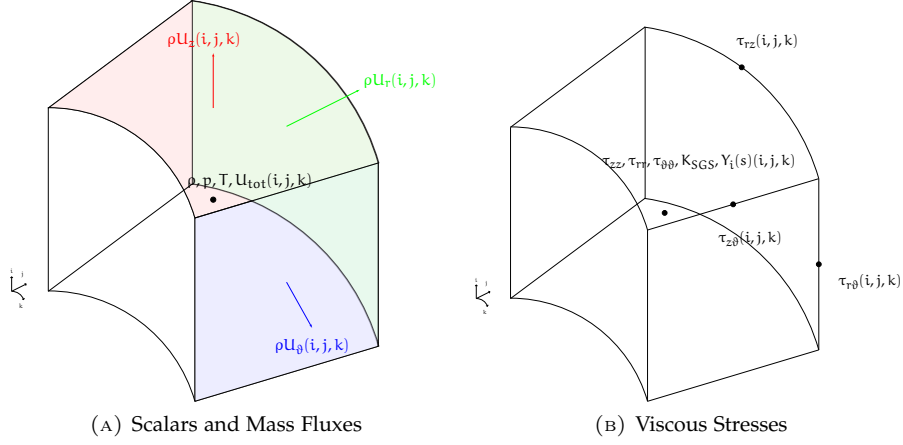
(B) Viscous Stresses

FIGURE 3.4. Variables Position in a Cell

$$i-1 \qquad i \qquad i+1 \qquad i+2$$
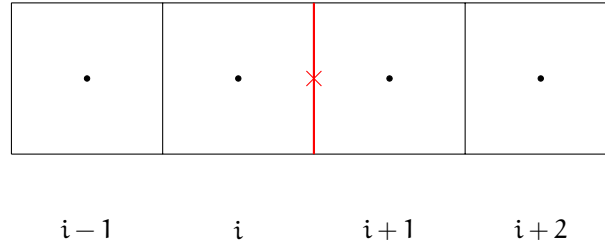
FIGURE 3.5. AUSM grid

width and collocated in the "positive" faces of the cell (see figure 3.4a). Viscous stresses are set in the cell center and in the edges of the cell (see figure 3.4b).

Summarizing, HeaRT code is a staggered numerical code that uses:

- AUSM numerical scheme with QUICK reconstruction for convective fluxes of scalar variables (ρ, U_{tot}, Y_i, k_{sgs}); the numerical algorithm, for evaluation of convective mass flux in a generic direction, is the following:

   1. left and right sound velocities are evaluated on the red face in figure 3.5 by the mean of a quadratic upstream interpolation

   $$a_L = Q_1^+ a(i+1) + Q_2^+ a(i) + Q_3^+ a(i-1)$$
   $$a_R = Q_1^- a(i+2) + Q_2^- a(i+1) + Q_3^- a(i) \tag{3.31}$$

   where Q_i^+ and Q_i^-, with $i = 1, \cdots 3$ are grid spacing depending metric terms;

   2. Mach number on the red face in figure 3.5 is evaluated from the

   $$M = U(i) \frac{a_L + a_R}{2 a_L a_R} \tag{3.32}$$

31
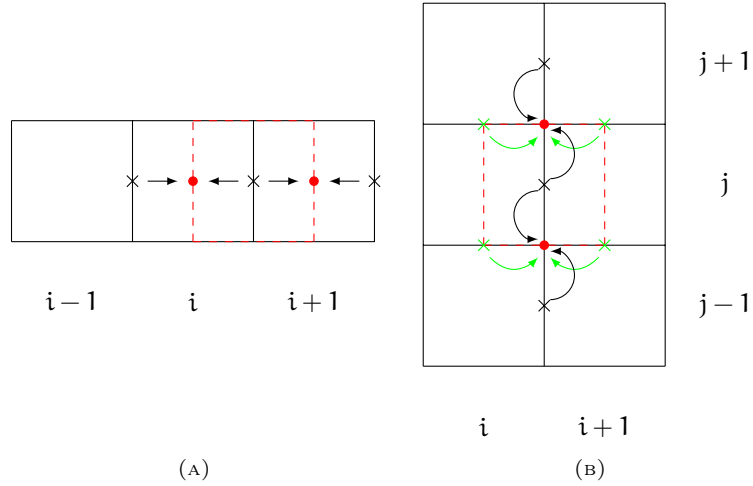
FIGURE 3.6. Interpolation scheme for "axial" and "orthogonal" mass fluxes and velocities

where $U(i)$ is the flow velocity orthogonal to the red face, where is collocated due to the staggered formulation;

3. the convective mass flux is evaluated from

$$F_c = \frac{1}{2}M\left(\rho a_L + \rho a_R\right) + |M|\left(\rho a_L - \rho a_R\right) \tag{3.33}$$

where ρa_L and ρa_R are the product of density and sound velocity evaluated by the means of equation (3.31);

the same algorithm is used for the other two directions and for convective energy fluxes $\rho U_{tot} + p$ and convective species fluxes ρY_i.

- second order centered finite difference numerical scheme for momentum (ρU_z, ρU_r, ρU_θ) and for diffusive fluxes of scalar variables; due to the staggered formulation adopted, some interpolations are necessary to obtain all the required variables in the right place; for "axial" momentum flux, mass flow and velocity have to be re-collocated in the cell center by the means of a linear interpolation from the two cell faces: as can be seen in figure 3.6a, staggered velocities and mass fluxes (the black crosses) are interpolated in the momentum cell faces (the red dotted cell) to compute momentum flux balance, with the following equation:

$$\phi(i) = c_i\phi(i + 1/2) + (1 - c_i)\phi(i - 1/2) \tag{3.34}$$

where due to the staggered formulation $c_i = 1/2$; after that, axial convective momentum flux $p + \rho uu$ can be computed, because the pressure is collocated on the cell center;

for "orthogonal" momentum flux, mass flux and velocity have to be re-collocated on the corners of the scalar cell (the red dots in figure 3.6b on the preceding page); orthogonal velocities (green crosses) are interpolated in the momentum cell face with the equation:

$$\phi(i+1/2) = c_i\phi(i+1) + (1-c_i)\phi(i) \tag{3.35}$$

but otherwise from "axial" flux, $c_i = \frac{x_{i+1/2}-x_i}{x_{i+1}-x_i}$; axial mass fluxes (black crosses) are interpolated in the momentum cell face with the equation:

$$\phi(j+1/2) = c_j\phi(j+1) + (1-c_j)\phi(j) \tag{3.36}$$

where $c_j = \frac{y_{j+1/2}-y_j}{y_{j+1}-y_j}$. After these simple interpolations, the other convective flux ($\rho u_a u_o$, where subscript "a" is for "axial" component and subscript "o" is for "orthogonal" component of flow velocity); viscous terms in the momentum equation, due to the staggered formulation adopted (see figure 3.4b on page 31), don't need any interpolation and the derivatives of these terms can be easily calculated by the equation (3.15).

For energy equation, viscous work terms and heat fluxes are evaluated from equation (3.15) as for diffusive terms in species equation.

- Newton-Raphson procedure for temperature calculation; the temperature is evaluated, starting from its old value (at the previous time-step), as the value for which the equation $nRT + E_{tot} - H_{tot} = 0$, where R is the universal gas constant, E_{tot} is the internal energy and H_{tot} is the standard formation enthalpy of the mixture.

- Runge-Kutta third order numerical scheme for time integration; in order to obtain a III order accurate scheme $s = 3$ must be chosen in equation (3.30); in the scheme here adopted [Shu and Osher, 1989] the coefficients are set to:

$$c_2 = c_3 = 0$$
$$b_1 = b_2 = \tfrac{1}{6} \quad b_3 = \tfrac{2}{3}$$
$$a_{21} = 1 \quad a_{31} = a_{32} = \tfrac{1}{4}.$$

In order to ensure the calculation stability two conditions must be respected: the condition on the *Courant-Friedricks-Lewy* (CFL) condition and the condition on the *Von Neumann* number VNN for the stability of transport-diffusion systems. The CFL (or *Courant*) number is defined as

$$CFL = \lambda_j^{MAX}\frac{\Delta t}{\Delta x_j} \tag{3.37}$$

where λ_j^{MAX} is the maximum local eigenvalue in the jth direction. The physical meaning of this condition can be explained with reference to Figure 3.7. CFL $= 1$ implies that Δt is the time by which the signal entering the control
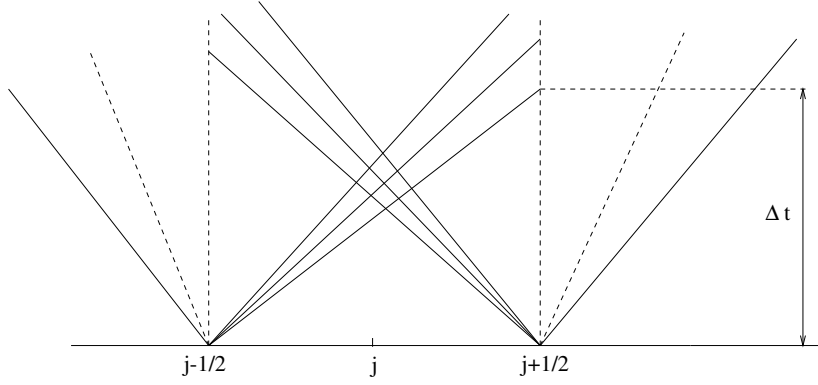
FIGURE 3.7. Physical interpretation of the CFL condition

volume crosses it reaching the opposite interface. Δt is therefore the time by which the flux estimate should be updated, unless the initial estimate already takes into account the outgoing flux variation.

The non-linear stability of this scheme, in conjunction with a ENO reconstruction is reported in [Shu and Osher, 1989] to be given by the condition CFL < 1. Nevertheless, the application of III order R-K schemes, in conjunction with the staggered discretization described in section (3.2 on page 30), to compressible flow LES is reported in [Nagarajan et al., 2003] to be performed using CFL = 0.29 in order to limit the effects of the truncation error.

The condition on the VNN defined as

$$VNN = \nu \frac{\Delta t}{(\Delta x)^2} \tag{3.38}$$

for a Forward-Time-Centered-Space (FTCS) it is reported to be VNN < 0.5 proven that a condition for the cell Reynolds number Re_Δ is satisfied. The complete analysis of the FTCS scheme stability is reported in [Thompson et al., 2005].

3.2.1 Boundary Conditions

For inlet and outlet boundary conditions, NSCBC (Navier-Stokes Characteristic Boundary Conditions) is adopted: in this way Navier-Stokes equation on the boundaries are solved with in terms of acoustical waves amplitude on the boundary itself [Poinsot and Veynante, 2005]. This boundary conditions are described in appendix C.

Because of the particular variables location, in a cylindrical geometry the axis is treated as a boundary condition: all the quantities are staggered with respect to the centerline in the radial direction (i.e. they lie at $\Delta/2$ from the axis), except u_r, that is collocated on the axis. The values of u_r at the centerline are obtained averaging the values of u_r near the axis as described below:

$$u_r(r=0,\vartheta) = \frac{1}{2}[u_r(\Delta r,\vartheta) + u_r(\Delta r, \vartheta + \pi)] \tag{3.39}$$

The angular distribution of u_r on the point near the axis of symmetry does not ensure a single value of u_r on the axis.

For wall boundary condition, eulerian wall, adiabatic wall, viscous wall and fixed temperature wall are available.

4

multi-resolution Technique for HeaRT Code

In this chapter, the original multi-resolution technique developed for HeaRT code during the present doctoral research is described. This method, based on joined-grids approach, require to prepare reliable procedures for variables values transfers and is been developed for cartesian or cylindrical three-dimensional non-uniform grids.

4.1 Parallel Computing and Domain Decomposition

Large parallel computers are become very popular in the last thirty years, and the number of processors available in these big clusters grows up very quickly. In this scenario, numerical simulation of big computational domains with a huge number of grid points can be performed, in a parallel environment with shared memory, with the assistance of the domain decomposition techniques. In particular, these techniques divide the computational grid into many overlapping sub domains (equal to the number of processor being used), and each processor solves its local sub domain independently from the other processors, yielding an apparently perfect parallel algorithm.

For a number of reasons, this is an illusion: in particular, any domain decomposition algorithm involves some communication and coordination between the computations on each domain, and the heaviest procedure is without doubt the communication with neighboring domains. With the use of explicit solvers and structured grids, communication between a generic sub domain and its neighbours is performed at every substep of the time integration algorithm by means of a simple copy of values, from "real" cells of a sub zone to the "ghost" cells of the neighbour sub zone.

These ghost cells are necessary for the grid cells near to the sub domain edge to perform a correct numerical integration of the conservative equations: for example, Finite Difference numerical scheme described in 3.1.2 on page 27, combined with a staggered grid, need a stencil of two points in the upstream direction for variable evaluation. As example, in figure 4.1 on the following page, a coarse

and a fine sub zone, joined in the j direction, are represented: the coarse sub zone (blue grid) requires two ghost cells in j direction (yellow colored, dashed blue cells in figure 4.1a), that are overlapped to the corresponding real cells of the neighbour fine zone; the fine sub zone (red grid) requires two ghost cells in j direction (yellow colored, dashed red cells in figure 4.1b), that are overlapped to the corresponding real cells of the coarse zone.
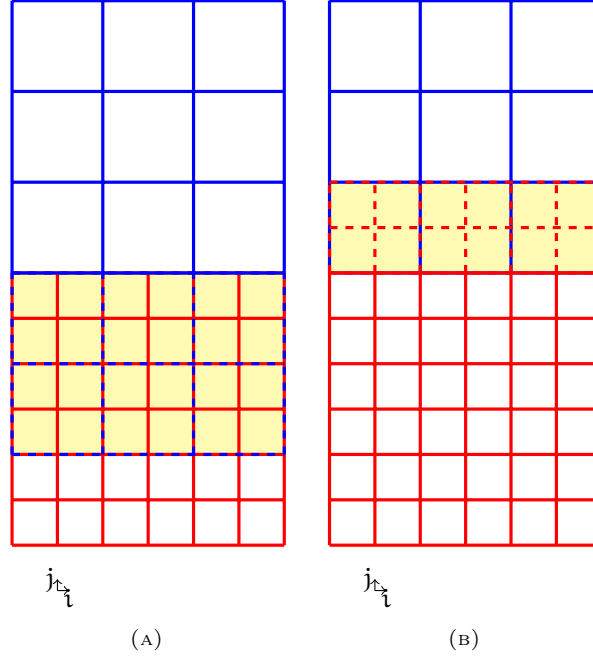
FIGURE 4.1. Example of ghost cells for a coarse block (a) and for a fine block (b)

4.2 Joined-Grids Approach

With the joined-grids approach, on the computational domain, multiblock grids with different spatial resolution can be placed side by side. The resolution of the block is identified from a parameter, named *level*: a grid block of level 1 is the coarsest, a grid block of level n is the finest (where n is the maximum number of levels that are present in the computational grid).

Another important parameter is the *refinement ratio*, defined as

$$r = \frac{\Delta x_{n-1}}{\Delta x_n} \tag{4.1}$$

where x is an arbitrary Cartesian or cylindrical grid direction and Δx_n is the grid step in x direction for level n. For the sake of simplicity, this refinement ratio is assumed constant for all three coordinates and equal to 2.

There's no limit to grid block junction: a grid block of level n can be next to a grid block of level $n + 2$; in such case is useful to combine level and refinement ratio informations, to obtain the number p of cells of the fine grid block that are contained in the neighbouring coarse grid block

$$p = r^{(n+2)-n} \tag{4.2}$$

If only one grid level is present (no mesh refinement adopted), variable values on ghost cells are obtained from a simple copy of the corresponding "real" cells of the neighboring grid block.

With the joined-grids approach, copy isn't the appropriate operation for the communication between grid blocks with different spatial resolution, so two new reliable procedures have been developed: the first, that transfer variable values from fine to coarse grid is called *restriction* and the second, that makes the opposite way is called *prolongation*.

4.2.1 Solution Algorithm

In the solution algorithm, each grid block solves conservation equations independently from other grid blocks, but the time step chosen in order to satisfy CFL condition is the same for all grids: minimum value is selected, as can be seen in figure 4.2 (where, for the sake of simplicity, only 3 zones of 3 different spatial resolutions - or levels - are illustrated).
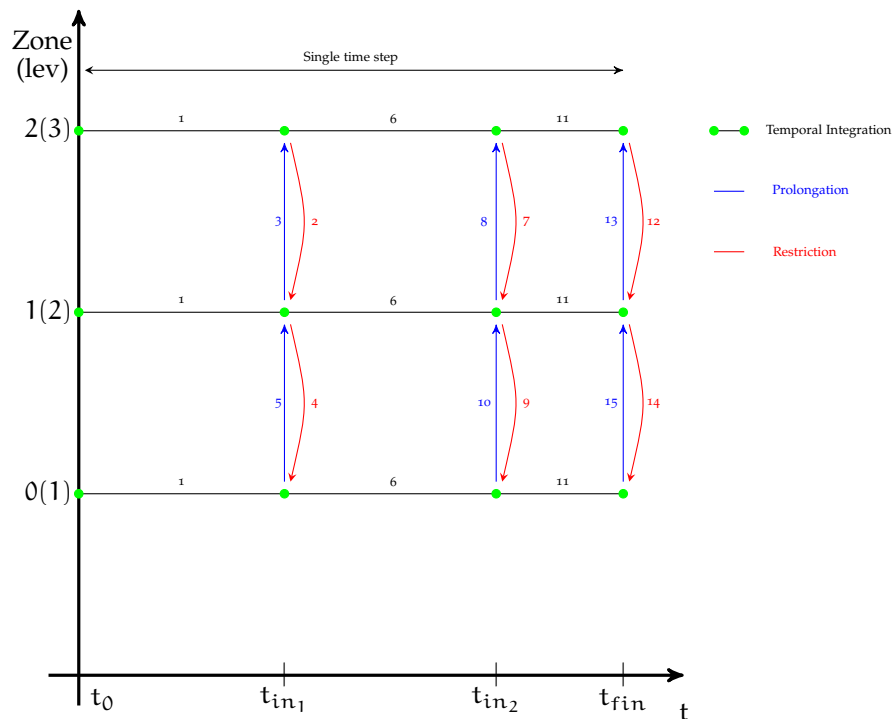
FIGURE 4.2. Scheme of temporal advance on all grid levels

38

Time integration procedure is here described:

1. *First RK Substep* of all zones, from t_0 to t_{in_1};

2. *Restriction* of boundary conditions at time t_{fin_1} from zone 2 to zone 1;

3. *Prolongation* of boundary conditions at time t_{fin_1} from zone 1 to zone 2;

4. *Restriction* of boundary conditions at time t_{fin_1} from zone 1 to zone 0;

5. *Prolongation* of boundary conditions at time t_{fin_1} from zone 0 to zone 1;

6. *Second RK Substep* of all zones, from t_{in_1} to t_{in_2};

7. *Restriction* of boundary conditions at time t_{fin_2} from zone 2 to zone 1;

8. *Prolongation* of boundary conditions at time t_{fin_2} from zone 1 to zone 2;

9. *Restriction* of boundary conditions at time t_{fin_2} from zone 1 to zone 0;

10. *Prolongation* of boundary conditions at time t_{fin_2} from zone 0 to zone 1;

11. *Third RK Substep* of all zones, from t_{in_2} to t_{fin};

12. *Restriction* of boundary conditions at time t_{fin_3} from zone 2 to zone 1;

13. *Prolongation* of boundary conditions at time t_{fin_3} from zone 1 to zone 2;

14. *Restriction* of boundary conditions at time t_{fin_3} from zone 1 to zone 0;

15. *Prolongation* of boundary conditions at time t_{fin_3} from zone 0 to zone 1;

At the end of any Runge-Kutta substep, finest zones start to transfer variables values on ghost cells of neighboring coarser zones, that subsequently transfer variables values on ghost cells of the finest zones; this couple of operations (prolongation and restriction) is repeated until coarsest zones are reached, and all ghost cells of all zones have updated their values. At this point, a new Runge-Kutta substep begins for all the zones of the domain.

Communications between zones of different spatial resolution are very important, because a correct variables transfer on ghost cells is essential to obtain a continuous solution on the entire domain.

4.2.2 Communication Procedures

For the sake if simplicity, communication procedures hereafter illustrated are related to a Cartesian uniform bi-dimensional grid: their form and structure can be easily extended to a three-dimensional cylindrical or Cartesian non-uniform grid.
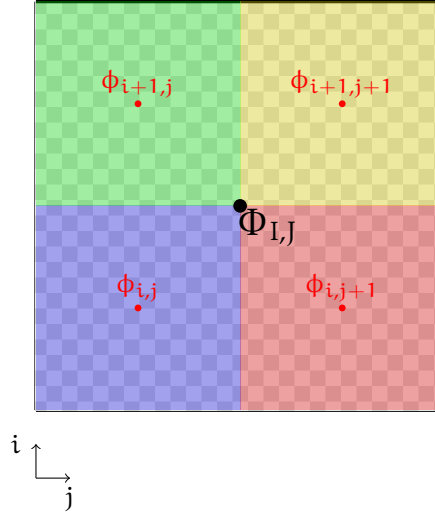
FIGURE 4.3. Scalar positions in a bidimensional grid

4.2.2.1 RESTRICTION

Restriction procedure is used for communication of numerical solution from level l to level $l-1$. For scalar variables (collocated at the centre of the cell, see figure 4.3), coarse value is obtained from fine values by the means of:

$$\Phi(I,J) = \frac{\Phi_{I,J}A_{I,J}}{A_{I,J}} \tag{4.3}$$

where

$$\Phi_{I,J}A_{I,J} = \phi(i,j)A(i,j) + \phi(i,j+1)A(i,j+1)$$
$$+ \phi(i+1,j)A(i+1,j) + \phi(i+1,j+1)A(i+1,j+1)$$
$$A_{I,J} = A(i,j) + A(i,j+1) + A(i+1,j) + A(i+1,j+1)$$

and $A_{I,J} = A(I,J)$; variables $A(i,j)$, $A(i,j+1)$, $A(i+1,j)$, $A(i+1,j+1)$ are fine cell areas (colored areas in figure 4.3), contained in coarse cell $A(I,J)$ (checkerboard zone in figure 4.3). Essentially a scalar value is a weighted sum of fine value, where the weight is the area fraction of each fine cell contained in the coarse one. Is straightforward that for a three-dimensional case coarse value is calculated with:

$$\Phi(I,J,K) = \frac{\sum\limits_{i=1}^{l}\sum\limits_{j=1}^{m}\sum\limits_{k=1}^{n} \phi(i,j,k)V(i,j,k)}{\sum\limits_{i=1}^{l}\sum\limits_{j=1}^{m}\sum\limits_{k=1}^{n} V(i,j,k)} \tag{4.4}$$

where l, m and n are the numbers of fine scalar cells contained in a scalar coarse cell for i, j and k direction respectively.
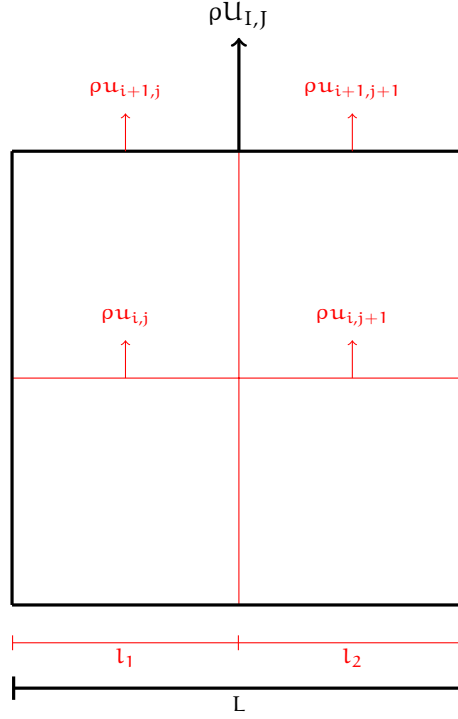
FIGURE 4.4. Momentum restriction

For momentum ρU, collocated at the positive edges (in a bi-dimensional grid) of a cell (see figure 4.4, coarse grid value is obtained from fine values by the means of:

$$\Phi(I, J) = \frac{\phi(i+1, j)l_1 + \phi(i+1, j+1)l_2}{l_1 + l_2} \tag{4.5}$$

where $L = l_1 + l_2$. For a three-dimensional grid, coarse scalar value is calculated from:

$$\Phi(I, J, K) = \frac{\displaystyle\sum_{j=1}^{m} \sum_{k=1}^{n} \phi(i_n, j, k) A(i_n, j, k)}{\displaystyle\sum_{j=1}^{m} \sum_{k=1}^{n} A(i_n, j, k)} \tag{4.6}$$

where $A(i_n, j, k)$ are the face areas of fine cell where are collocated $\phi(i_n, j, k)$ momentum and $\mathcal{A} = \displaystyle\sum_{j=1}^{m} \sum_{k=1}^{n} A(i_n, j, k)$ is the face area of coarse cell where $\Phi(I, J)$ is collocated.

RESTRICTION OBSERVATIONS   From the previous section it's clear that the restriction treatment for momentum is different from the restriction treatment for scalar,
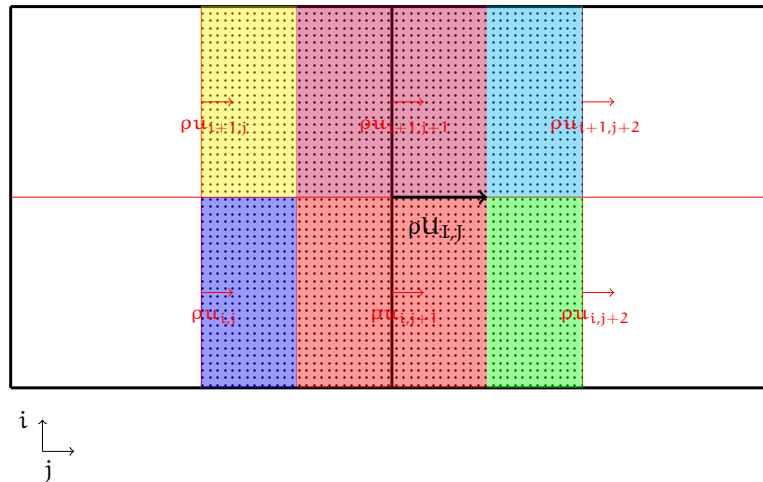
FIGURE 4.5. Momentum control volumes for coarse (area with points) and fine (colored areas) cells

not much for the procedure itself (in both cases a "weighted" sum is used), but for the diverse approach: the scalar restriction, indeed, is obtained by the mean of a sum of all the fine variables that have their control volumes are enclosed in the control volume of the coarse scalar; when a cell is refined (and therefore divided in several little cells), the scalar control volumes for a single coarse is shared between all the fine cells that are contained in the biggest one, as can be seen in figure 4.3 on page 40, where the coarse cell control volume is the checkerboard zone and th fine cells control volumes are the colored zones. So the restriction procedure for scalar variables is fully conservative, because it takes place on the exact control volumes.

Momentum restriction follow a different approach: in a staggered grid, the computational cell coincide with the scalar control volume, while the momentum control volume is shared between two adjacent cells, as can be seen from figure 4.5; so, when the grid is refined, the coarse momentum control volume is constituted by (in the streamlined picture) two entire fine momentum control volumes (red and pink squares) and four fine momentum control volume fractions (yellow, purple, green and cyan rectangles).

If for momentum restriction is adopted the same criterion used for scalar restriction, a paradox can occur: the momentum $\rho U_{I,J}$ could not be the sum of the two $\rho u_{i,j+1}$ and $\rho u_{i+1,j+1}$ fine momentum; this is impossible, because the momentum ρu is clearly a mass flux in a proper direction, and therefore, from a "local" conservation point of view, the mass flux that pass through a surface in common between fine and coarse grid must be the same. So for momentum restriction the procedure described in the previous section is based on the sum over the surfaces and not over the volumes.

4.2.2.2 Prolongation

For prolongation, an accurate interpolation algorithm is been chosen, and therefore the communication "operator" has a big complexity.

The selected algorithm is the same for both scalar and momentum prolongation: least squares interpolation, that conserves mean value in the control volumes. To compute the fine cell interpolated value a Taylor series expansion about the coarse value c_i that belongs to the corresponding coarse cell (the "centroid"):

$$
\begin{aligned}
\phi_{c_i}^{INT}(\mathbf{x}) = \phi_{c_i} &+ \left.\frac{\partial \phi}{\partial x}\right|_{c_i} \Delta x + \left.\frac{\partial \phi}{\partial y}\right|_{c_i} \Delta y + \left.\frac{\partial \phi}{\partial z}\right|_{c_i} \Delta z + \\
&+ \left.\frac{\partial^2 \phi}{\partial x^2}\right|_{c_i} \frac{\Delta x^2}{2} + \left.\frac{\partial^2 \phi}{\partial y^2}\right|_{c_i} \frac{\Delta y^2}{2} + \left.\frac{\partial^2 \phi}{\partial z^2}\right|_{c_i} \frac{\Delta z^2}{2} + \\
&+ \left.\frac{\partial^2 \phi}{\partial x \partial y}\right|_{c_i} \Delta x \Delta y + \left.\frac{\partial^2 \phi}{\partial x \partial z}\right|_{c_i} \Delta x \Delta z + \left.\frac{\partial^2 \phi}{\partial y \partial z}\right|_{c_i} \Delta y \Delta z
\end{aligned}
\tag{4.7}
$$

where $\Delta x = x - x_{c_i}, \Delta y = y - y_{c_i}, \Delta z = z - z_{c_i}$ being the distances, along the three Cartesian coordinates, between the reconstruction point and the centroid c_i where derivatives in equation (4.7) are calculated. If first order interpolation is chosen, only the first 4 must be maintained in equation (4.7). In a three-dimensional case, for a third order interpolation, there are 9 unknowns (the derivatives in the equation (4.7)), so for the sake of simplicity of the numerical algorithm, a total number of 26 neighboring points to the centroid are used to construct the stencil of least squares interpolation.

To conserve the mean value in the control volume of the interpolating function $\phi_{c_i}^{INT}(\mathbf{x})$, the following equation must be forced:

$$
\overline{\phi}_i = \frac{1}{V_i} \int_{V_i} \phi_{c_i}^{INT}(\mathbf{x}) dV
\tag{4.8}
$$

Substituting equation (4.7) in (4.8) and computing the mean value in a volume V_j of the interpolation stencil gives:

$$
\begin{aligned}
\phi_j = \overline{\phi}_i &+ \left.\frac{\partial \phi}{\partial x}\right|_{c_i} \frac{1}{V_j} \int_{V_j} \Delta x \, dV + \left.\frac{\partial \phi}{\partial y}\right|_{c_i} \frac{1}{V_j} \int_{V_j} \Delta y \, dV + \\
&+ \left.\frac{\partial \phi}{\partial z}\right|_{c_i} \frac{1}{V_j} \int_{V_j} \Delta z \, dV + \\
&+ \left.\frac{\partial^2 \phi}{\partial x^2}\right|_{c_i} \frac{1}{2V_j} \int_{V_j} \Delta x^2 \, dV + \left.\frac{\partial^2 \phi}{\partial y^2}\right|_{c_i} \frac{1}{2V_j} \int_{V_j} \Delta y^2 \, dV + \\
&+ \left.\frac{\partial^2 \phi}{\partial z^2}\right|_{c_i} \frac{1}{2V_j} \int_{V_j} \Delta z^2 \, dV + \\
&+ \left.\frac{\partial^2 \phi}{\partial x \partial y}\right|_{c_i} \frac{1}{V_j} \int_{V_j} \Delta x \Delta y \, dV + \left.\frac{\partial^2 \phi}{\partial x \partial z}\right|_{c_i} \frac{1}{V_j} \int_{V_j} \Delta x \Delta z \, dV + \\
&+ \left.\frac{\partial^2 \phi}{\partial y \partial z}\right|_{c_i} \frac{1}{V_j} \int_{V_j} \Delta y \Delta z \, dV
\end{aligned}
\tag{4.9}
$$

To avoiding calculation of $x - x_{c_i}$, etc...., integrals for each control volume V_j with respect to c_i [Ollivier-Gooch, 1997], values $x - x_{c_i}$, $y - y_{c_i}$, $z - z_{c_i}$ in equation (4.9) are replaced with $\left(x - x_{c_j}\right) + \left(x_{c_j} - x_{c_i}\right)$, $\left(y - y_{c_j}\right) + \left(y_{c_j} - y_{c_i}\right)$, $\left(z - z_{c_j}\right) + \left(z_{c_j} - z_{c_i}\right)$:

$$
\overline{\phi}_j = \overline{\phi}_i + \left.\frac{\partial \phi}{\partial x}\right|_{c_i} \widehat{x} + \left.\frac{\partial \phi}{\partial y}\right|_{c_i} \widehat{y} + \left.\frac{\partial \phi}{\partial z}\right|_{c_i} \widehat{z} + \left.\frac{\partial^2 \phi}{\partial x^2}\right|_{c_i} \widehat{x^2} + \left.\frac{\partial^2 \phi}{\partial y^2}\right|_{c_i} \widehat{y^2} + \left.\frac{\partial^2 \phi}{\partial z^2}\right|_{c_i} \widehat{z^2}
$$
$$
+ \left.\frac{\partial^2 \phi}{\partial xy}\right|_{c_i} \widehat{xy} + \left.\frac{\partial^2 \phi}{\partial xz}\right|_{c_i} \widehat{xz} + \left.\frac{\partial^2 \phi}{\partial yz}\right|_{c_i} \widehat{yz}
$$

$$(4.10)$$

with

$$
x^n \widehat{y^m} z^p = \frac{1}{V_i} \int_{V_i} \left[\left(x - x_{c_j}\right)\left(x_{c_j} - x_{c_i}\right)\right]^n \left[\left(y - y_{c_j}\right)\left(y_{c_j} - y_{c_i}\right)\right]^m
$$
$$
\left[\left(z - z_{c_j}\right)\left(z_{c_j} - z_{c_i}\right)\right]^p dV
$$
$$
= \sum_{k=0}^{n} \frac{n!}{k!\,(n-k)!} \left(x_{c_j} - x_{c_i}\right)^k \sum_{l=0}^{m} \frac{m!}{l!\,(m-l)!} \left(y_{c_j} - y_{c_i}\right)^l \qquad (4.11)
$$
$$
\sum_{r=0}^{p} \frac{p!}{r!\,(p-r)!} \left(y_{c_j} - y_{c_i}\right)^r \overline{x^{n-k} y^{m-l} z^{p-r}}
$$

and

$$
\overline{x^m y^n z^p} = \frac{1}{V_i} \int_{V_i} \left(x - x_{c_i}\right)^m \left(y - y_{c_i}\right)^n \left(z - z_{c_i}\right)^p dV \qquad (4.12)
$$

Writing equation (4.10) for any coarse point that belongs to the interpolation stencil, an overdetermined system of equations can be obtained:

$$
\Delta\phi = \mathbf{S} d\phi \qquad (4.13)
$$

where

$$
\Delta\phi = \begin{bmatrix} w_{i1}\left(\overline{\phi}_1 - \overline{\phi}_{c_i}\right) \\ w_{i2}\left(\overline{\phi}_2 - \overline{\phi}_{c_i}\right) \\ \cdots \\ \cdots \\ w_{iN}\left(\overline{\phi}_{N_i} - \overline{\phi}_{c_i}\right) \end{bmatrix} \qquad (4.14)
$$

$$
\mathbf{S} = \begin{bmatrix} \widehat{x}_1 & \widehat{y}_1 & \widehat{z}_1 & \widehat{x^2}_1 & \widehat{y^2}_1 & \widehat{z^2}_1 & \widehat{xy}_1 & \widehat{yz}_1 & \widehat{xz}_1 \\ \widehat{x}_2 & \widehat{y}_2 & \widehat{z}_2 & \widehat{x^2}_2 & \widehat{y^2}_2 & \widehat{z^2}_2 & \widehat{xy}_2 & \widehat{yz}_2 & \widehat{xz}_2 \\ & & & & \cdots & & & & \\ & & & & \cdots & & & & \\ \widehat{x}_{N_i} & \widehat{y}_{N_i} & \widehat{z}_{N_i} & \widehat{x^2}_{N_i} & \widehat{y^2}_{N_i} & \widehat{z^2}_{N_i} & \widehat{xy}_{N_i} & \widehat{yz}_{N_i} & \widehat{xz}_{N_i} \end{bmatrix} \qquad (4.15)
$$

$$d\phi = \begin{bmatrix} \frac{\partial \phi}{\partial x} & \frac{\partial \phi}{\partial y} & \frac{\partial \phi}{\partial z} & \frac{\partial^2 \phi}{\partial x^2} & \frac{\partial^2 \phi}{\partial y^2} & \frac{\partial^2 \phi}{\partial z^2} & \frac{\partial \phi}{\partial xy} & \frac{\partial \phi}{\partial yz} & \frac{\partial \phi}{\partial xz} \end{bmatrix} \tag{4.16}$$

and

$$w_{ij} = \frac{1}{\left| \overrightarrow{x}_j - \overrightarrow{x}_i \right|^2} \tag{4.17}$$

The system of equations (4.13) can be rearranged in the form:

$$d\phi = \mathbf{S}^{-1} \mathbf{\Delta} \phi \tag{4.18}$$

where $\mathbf{S}$ matrix contains only geometrical constants and so can be calculated once.

After the interpolation, to ensure local conservation, the interpolated scalar values are modified as:

$$\phi = \frac{\Phi V}{\sum \phi_i' \nu_i} \phi' \tag{4.19}$$

where ϕ' is the original fine interpolated value, Φ is the centroid coarse value, V is the coarse cell volume and ϕ_i' and ν_i are respectively the fine interpolated values and the fine cells volumes of all the fine cells that form the centroid coarse cell. The interpolated momentum values are modified as:

$$\phi = \frac{\Phi A}{\sum \phi_i' a_i} \phi' \tag{4.20}$$

where ϕ' is the original fine interpolated value, Φ is the centroid coarse value, A is the coarse cell surface area in a coordinate direction and ϕ_i' and a_i are respectively the fine interpolated values and the fine cells surface areas of all the fine cells that form the centroid coarse cell.

Interpolation Stencil   The neighboring points are, of course, points that belong both to coarse and to fine grids: in this way, also if the complexity of the interpolation algorithm increases, only "true" integrated points are used to obtain the fine value and for this reason restriction and prolongation operations are decoupled.

In figure 4.6 on the next page interpolation domain for scalar value in a bidimensional Cartesian grid is illustrated: the interpolation stencil is composed by only coarse points, the green dot is the centroid, the red cross is the fine value that has to be calculated and the black dots are all coarse points that belong to the interpolation stencil; with the blue line the grid border is represented. Yellow color cells in figure, that belong to the interpolation stencil, lie on the fine grid and therefore their variable values are obtained by means of a restriction of corresponding "true" fine grid points: so the prolongation depends on restriction and the whole operation is like a closed loop.

In figures 4.7 on page 47 are illustrated the stencils adopted for scalar and momentum values in a bidimensional Cartesian grid: the green dot is the centroid, the red cross is the fine value that has to be calculated and the black dots are all coarse and fine points that belong to the interpolation stencil. As can be seen,
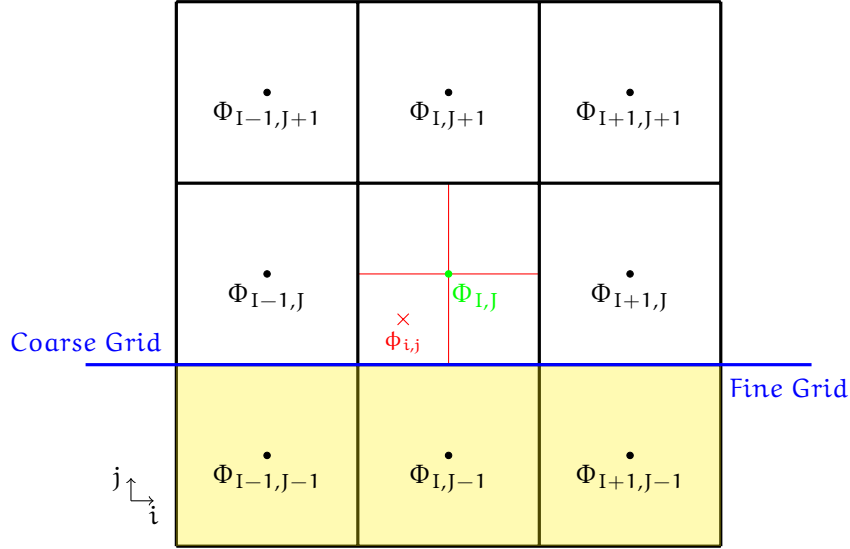
Figure 4.6. Interpolation stencil with only coarse points

also if the complexity of the stencil (and so the identification of all the points that belong to it) is increased, only "true" grid points (where the numerical solution is derived from the integration of the conservation equations) are used for the evaluation of fine grid ghost cells, and so the stencil of the interpolation is composed by both coarse and fine grid points.

The only one case where the stencil is composed only by coarse grid points is the interpolation of a fine ghost cell that lies beyond the limits of r (refinement ratio) fine cells after fine grid boundary, in each direction (see figure 4.7d on the next page): in this case there isn't any fine grid point available.

4.2.2.3 Variable Treatment

Into HeaRT numerical code, conservative variables (ρ, ρu_x, ρu_y, ρu_z, ρe_{tot} and ρY_i) are evaluated by means of numerical integration of the conservation equations described in 2 on page 11; the temperature of the fluid is evaluated from the conservative variables by means of Newton-Raphson Method (see 3.1.3 on page 28), and the fluid pressure is evaluated from the density and the temperature by means of the equation of state of gas.

The same procedure was earlier adopted for restriction and prolongation: the conservative variables were added or interpolated and then the temperature and the pressure were evaluated; this approach, however, often has lead to an oscillatory trend for the pressure evaluated on fine ghost cells, also if all the conservative variables, the temperature, the molecular weight of the mixture and the gas constant were smooth. So, for the evaluation of the variables on the "ghost" cells is been putted in place: not all the conservative variables are interpolated (or summed), and the equation of state is used for ρ evaluation; for the sake of

(A) Interpolation stencil for an edge

(B) Interpolation stencil for a corner

(C) Interpolation stencil for a corner

(D) Interpolation stencil for an "external" ghost cell
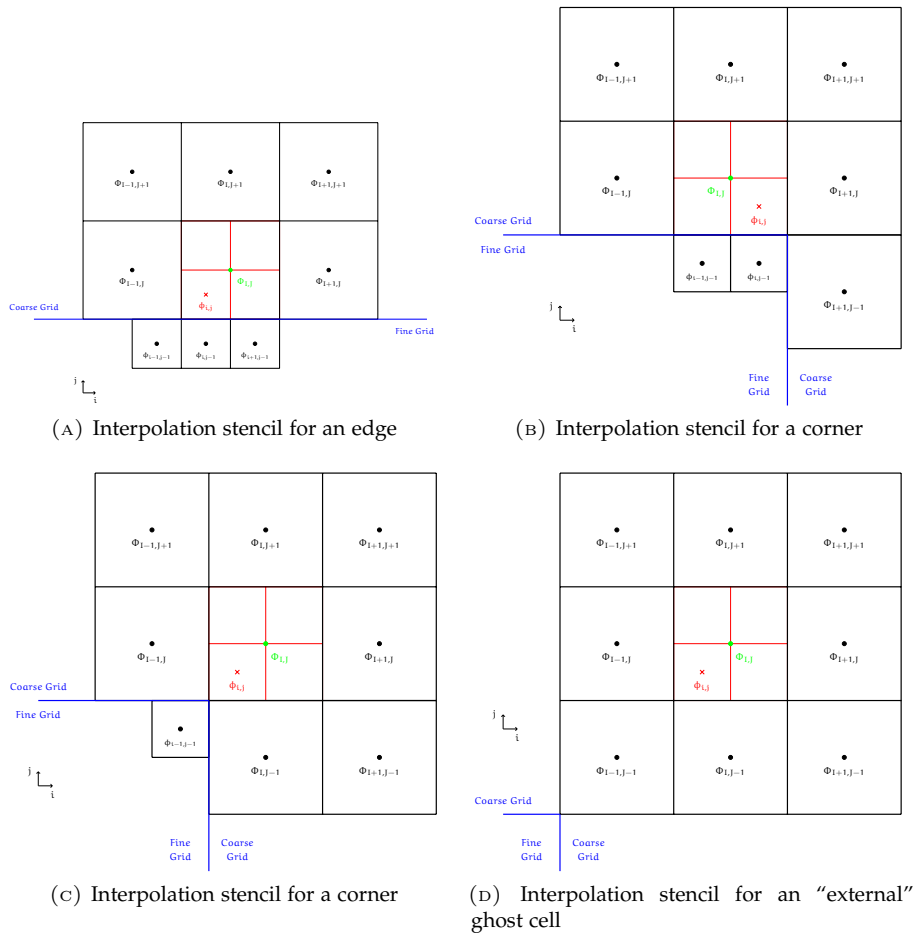
FIGURE 4.7.   Interpolation stencils adopted

47

simplicity, operation detail shown below is related to the prolongation, but the operation sequence is the same for the restriction:

- ρu_x, ρu_y, ρu_z and ρY_i are interpolated;

- p and T are interpolated;

- ρ is evaluated from p and T by means of equation of state of gas;

- ρe_{tot} is evaluated by means of the sum of kinetic and internal energy.

Part II

Research Results

5

Preliminary Validation

I~n~ this chapter a preliminary validation of multi-resolution technique developed for HeaRT code is described: this validation is performed by the mean of two simple numerical test cases, to highlight the formal accuracy of the procedures described in the chapter 4.

5.1 Rankine Vortex

The Rankine vortex is a simple model for a vortex, that is represented by a core rotating with a constant angular velocity and an external zone with an asymptotic decreasing velocity:

$$v_t(r) = \begin{cases} \omega r, & r \leqslant a \\ \dfrac{\omega a^2}{r}, & r > a \end{cases} \tag{5.1}$$

For an incompressible fluid, neglecting gravity force, the pressure follows the equation:

$$p(r) = \begin{cases} \rho \omega^2 \dfrac{r^2}{2}, & r \leqslant a \\ -\dfrac{\rho \omega^2 a^4}{2r^2} + \rho \omega^2 a^2, & r > a \end{cases} \tag{5.2}$$

Tangential velocity and pressure trends are represented in figure 5.1

The simulation parameters are summarized in table 5.1. Initial conditions of the numerical simulation, for pressure and tangential velocity are represented in figures 5.2b and 5.2c: for the sake of simplicity, the flow field is initialized with only the rotating core).

The computational domain is represented in figure 5.2a (with the red color the fine zone, with gray color the coarse zone): for all the edges, NSCBC are imposed.

(A) Tangential Velocity   (B) Pressure
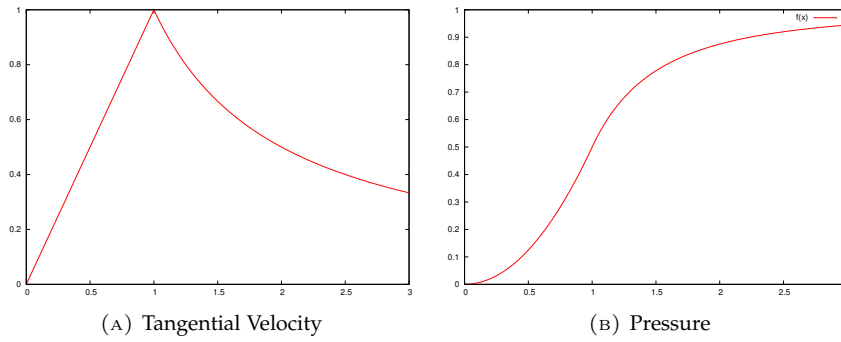
Figure 5.1.   Tangential Velocity and Pressure for a Rankine Vortex with $\omega = a = 1$

Cylinder radius (r)	$15\,cm$
Cylinder height (h)	$1\,cm$
Total grid points	$185\,600$
Fine grid points	$153\,600$
Fine grid radius (r_f)	$5.5\,cm$
Level 1 grid space in j and i directions	$3.75\,mm$, $1\,mm$
Level 2 grid space in j and i directions	$1.875\,mm$, $0.5\,mm$
Level 1 grid nodes in θ direction	128
Level 2 grid nodes in θ direction	256
Angular velocity	$25\,rad\,s^{-1}$

Table 5.1.   Simulation Setup

(A) Computational Grid   (B) Pressure   (C) Tangential Velocity
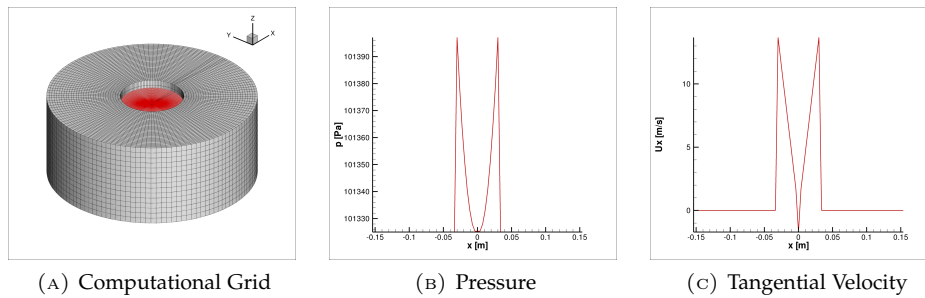
Figure 5.2.   Initial Conditions

5.1.1 Simulation Results

In figures 5.3 and 5.4 are illustrated the pressure and tangential velocity pro-files along a radius: the connection between the two zones is well represented and none spurious oscillation appears. At the beginning of the simulation, the imposed discontinuity on pressure produces some spurious oscillations that, be-cause of the high resolution of the numerical grid, quickly disappear from the flow field.

The flow viscosity, moreover, reduces gradually the tangential velocity peak, that diminishes from $\sim 12\,\mathrm{m\,s^{-1}}$ (figure 5.3b) to $\sim 10\,\mathrm{m\,s^{-1}}$ (figure 5.4d).

(A)   (B)

(C)   (D)

(E)   (F)
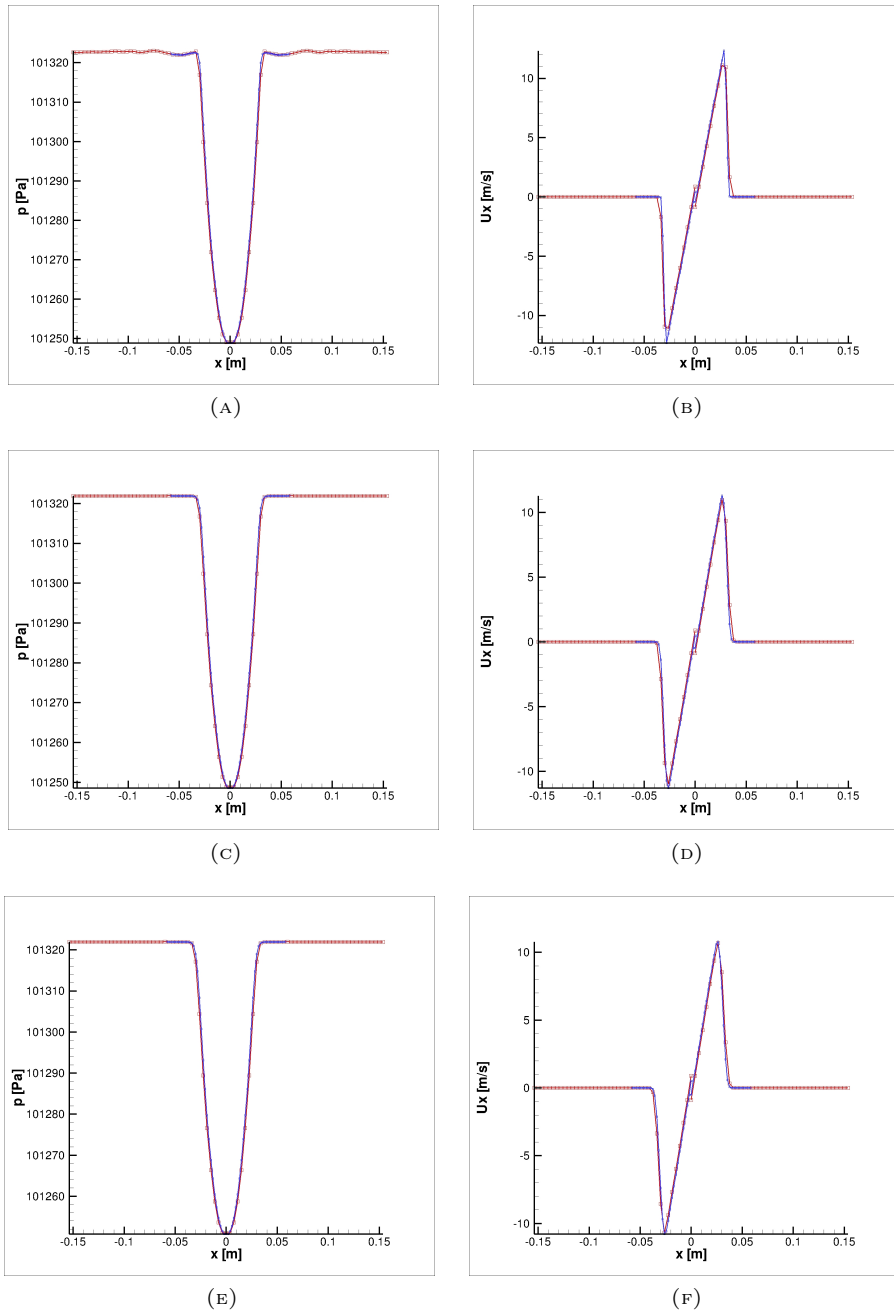
FIGURE 5.3.   Pressure and tangential velocity profiles

FIGURE 5.4. Pressure and tangential velocity profiles

5.2 JET SIMULATIONS

The numerical simulation of simple jets in a squared duct, also if it is very simple, can emphasize some numerical bugs and algorithm errors. Three numerical simulations have been performed, with an N_2 jet that flows in a squared duct where the nitrogen is stillness: two with a one dimensional jet, the first on an eulerian flow, the second on a viscous flow, the third with a parabolic jet.

For all the three simulations, the temperature of the gas is 300 K and its pressure is 101 325 Pa; for the one dimensional jet, the axial velocity at the inlet is increased from the null initial value to 7.41 m s^{-1}, with the time law illustrated in figure 5.5a on the following page, and it's the same for the whole xy inlet plane. For the parabolic jet, the velocity increasing vs time follows the same trend of figure 5.5a, while the final velocity profile in the xy plane is illustrated in figure 5.5b.

The computational grid is the same for all the three simulations and is illustrated in figure 5.6a on page 55, where the finest zone (red mesh in the picture, level 2) is surrounded, in every direction, by coarsest zones (black mesh in the picture, level 1), in order to test communication procedures in all the three coordinate directions. The simulation parameters are summarized in the table 5.2:

(A) Time Law

(B) Parabolic Velocity Profile
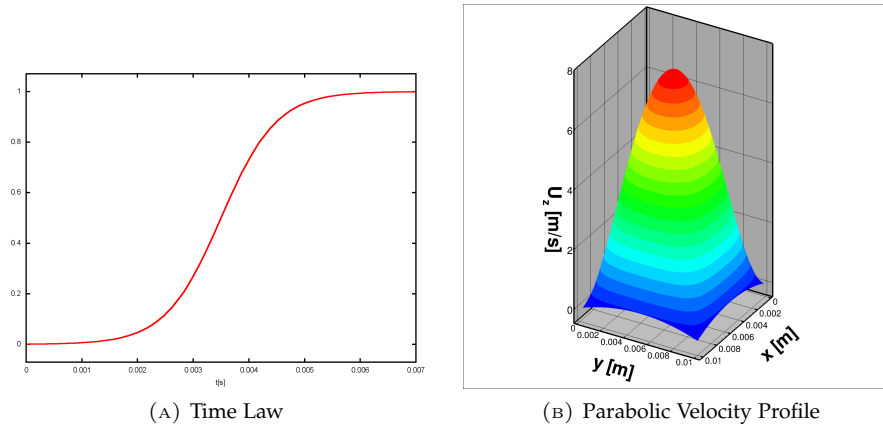
Figure 5.5. Inlet Boundary Conditions

Duct width (h)	1 cm
Domain size in the crosswise (x), spanwise (y) and streamwise (z) directions	$h \times h \times 3h$
Total grid points	304 000
Fine grid points	128 000
Fine grid size in the crosswise (x), spanwise (y) and streamwise (z) directions	$0.5h \times 0.5h \times h$
Steady jet velocity	$7.41 \, \text{m s}^{-1}$
Level 1 grid space	$5 \times 10^{-1} \, \text{mm}$
Level 2 grid space	$2.5 \times 10^{-1} \, \text{mm}$

Table 5.2. Simulation Setup

the domain size in the crosswise (x), spanwise (y) and streamwise (z) directions is $L_x \times L_y \times L_z = h \times h \times 3h$, where $h = 1 \times 10^{-2} \, \text{m}$ is the duct width; the grid is uniform for all the three directions, with $\Delta x_1 = \Delta y_1 = \Delta z_1 = 2.5 \times 10^{-4} \, \text{m}$ for the first (coarse) level, and $\Delta x_2 = \Delta y_2 = \Delta z_2 = 5 \times 10^{-4} \, \text{m}$ for the second (fine) level.

For the first run, performed with an eulerian flow, in z direction NSCBC (Navier-Stokes Characteristic Boundary Conditions) are imposed, in order to obtain non-reflecting inlet and outlet boundary conditions, while in x and y directions eulerian and adiabatic walls boundary conditions are imposed.

For the second and the third run, performed with a viscous flow, in z direction NSCBC (Navier-Stokes Characteristic Boundary Conditions) are imposed, in order to obtain non-reflecting inlet and outlet boundary conditions, while in x and y directions viscous and adiabatic walls boundary conditions are imposed.

The velocity profiles are evaluated on five lines, that are parallel to the z axis and that pass through the green points illustrated in figure 5.6b. In this figure, the fine grid is painted in red, while the coarse grid is painted in blue; the choice of these points isn't coincidental: the E point is the center of the duct in ax xy plane, the other four points are points where the numerical solution obtained on the

54

(A) Computational Grid   (B) Sampling Points in the xy Plane
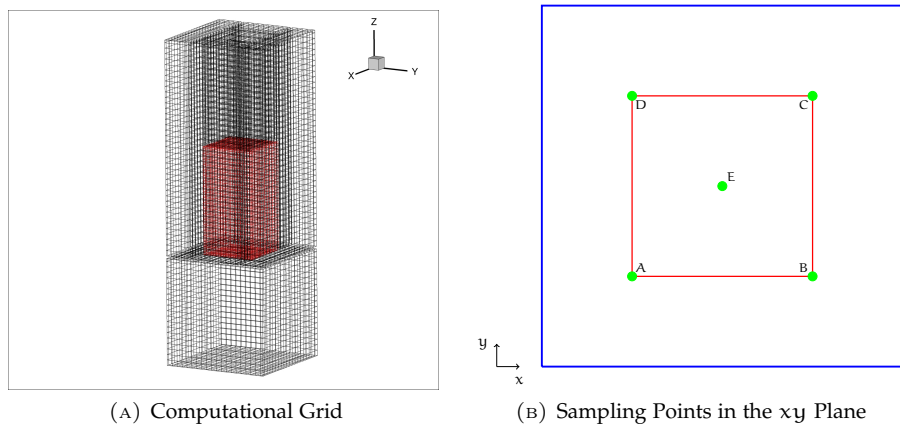
Figure 5.6.   Grid and Sampling Points Configurations

fine grid is affected by the communication procedures in all the three coordinate directions.

5.2.1   Simulation Results

5.2.1.1   One Dimensional Eulerian Jet

In the figures 5.7 on the following page and 5.8 on page 57 are illustrated the profiles of the three velocity components, for the five points described in figure 5.6b: as can be easily expected, the flow remain one-dimensional and the unique velocity component that is not equal to zero is U_z. At the coarse-fine interface the solution is smooth and the "connection" between the two zones take place flawlessly.

In figure 5.9 on page 58 are illustrated two-dimensional slides of the U_z velocity component and also from this pictures the mono-dimensional behaviour of the flow field is evident: the iso-surfaces are always perfectly orthogonal to the direction of the flow.

5.2.1.2   One Dimensional Viscous Jet

In the figures 5.10 on page 59 and 5.11 on page 60 are illustrated the profiles of the three velocity components, for the five points described in figure 5.6b: when the jet starts to flow in the duct, because of the viscous walls, U_x and U_y velocity components start to arise at the inlet (figures 5.10d, 5.10e, 5.10g, 5.10h), while at the center of the duct the crosswise and spanwise velocities remain null.

As the flow propagates into the duct, the crosswise and spanwise velocity components grow but remain symmetrical respect to the streamwise axis that passes through the E point; U_x and U_y, furthermore, are also identical. Another noticeable aspect is the U_z velocity increase in the streamwise direction, as can be seen in figures 5.11a, 5.11b, 5.11c: the outlet value is greater than the inlet one, and

(A) U_z, A and C points   (B) U_z, B and D points   (C) U_z, E point

(D) U_x, A and C points   (E) U_x, B and D points   (F) U_x, E point

(G) U_y, A and C points   (H) U_y, B and D points   (I) U_y, E point
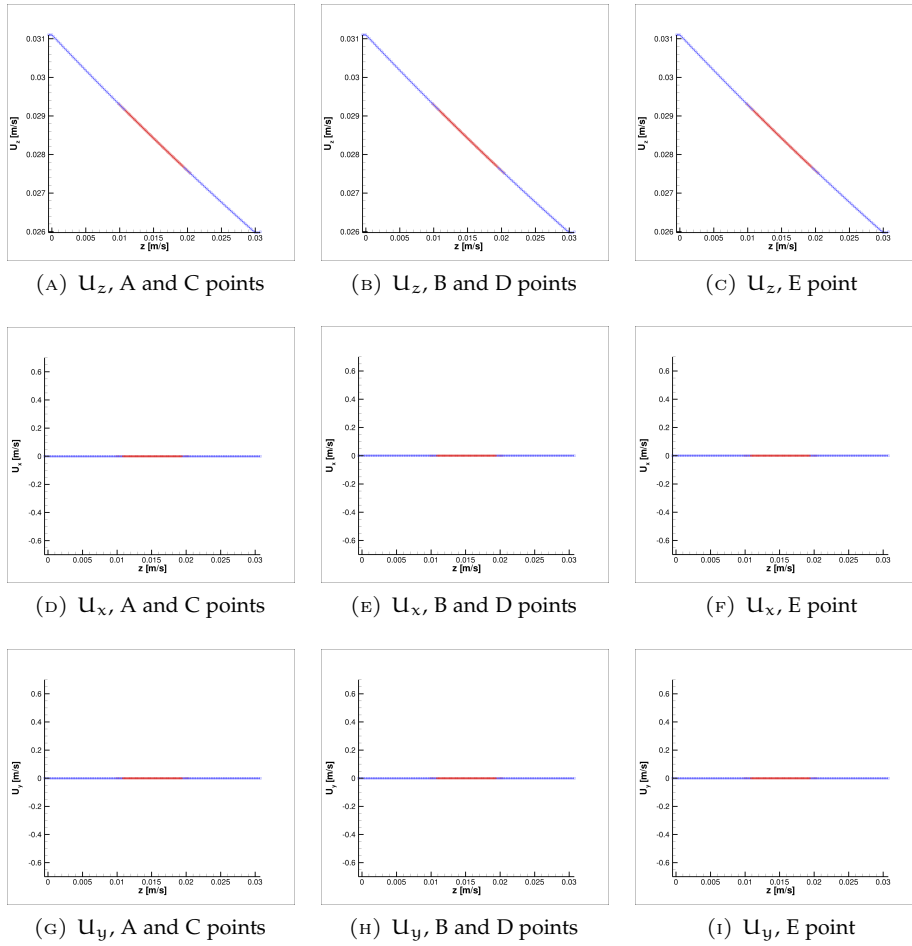
FIGURE 5.7. Eulerian flow velocity profiles, $t = 3.73 \times 10^{-4}$ s

(A) U_z, A and C points (B) U_z, B and D points (C) U_z, E point

(D) U_x, A and C points (E) U_x, B and D points (F) U_x, E point

(G) U_y, A and C points (H) U_y, B and D points (I) U_y, E point
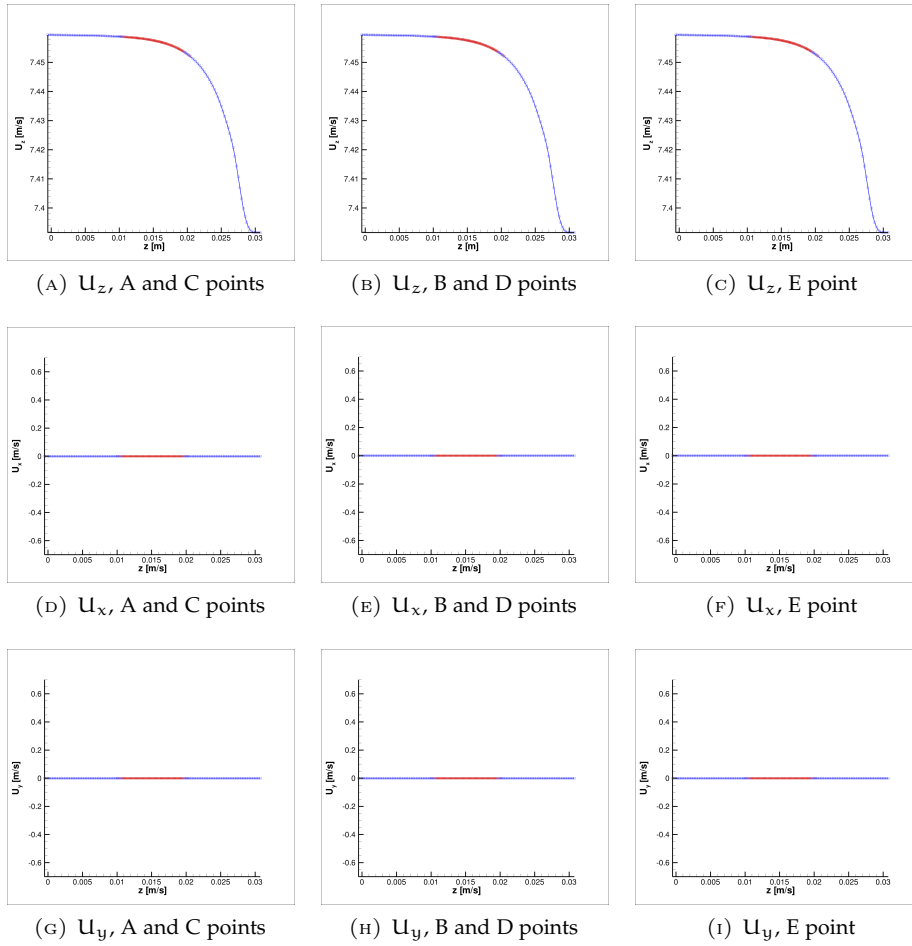
FIGURE 5.8. Eulerian flow velocity profiles, $t = 7.37 \times 10^{-3}$ s

(A) U_z, $t = 1.0 \times 10^{-3}$ s

(B) U_z, $t = 3.0 \times 10^{-3}$ s

(C) U_x, $t = 5.0 \times 10^{-3}$ s

(D) U_x, $t = 8.0 \times 10^{-3}$ s
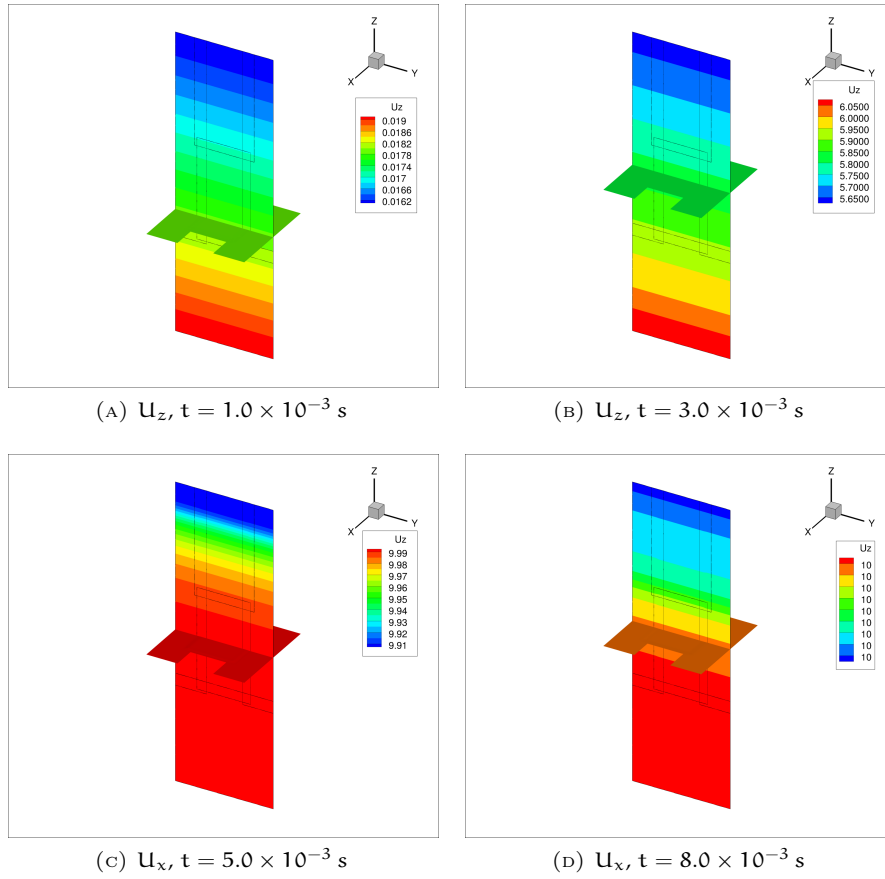
FIGURE 5.9. Eulerian flow velocity 2D slides

(A) U_z, A and C points   (B) U_z, B and D points   (C) U_z, E point

(D) U_x, A and C points   (E) U_x, B and D points   (F) U_x, E point

(G) U_y, A and C points   (H) U_y, B and D points   (I) U_y, E point
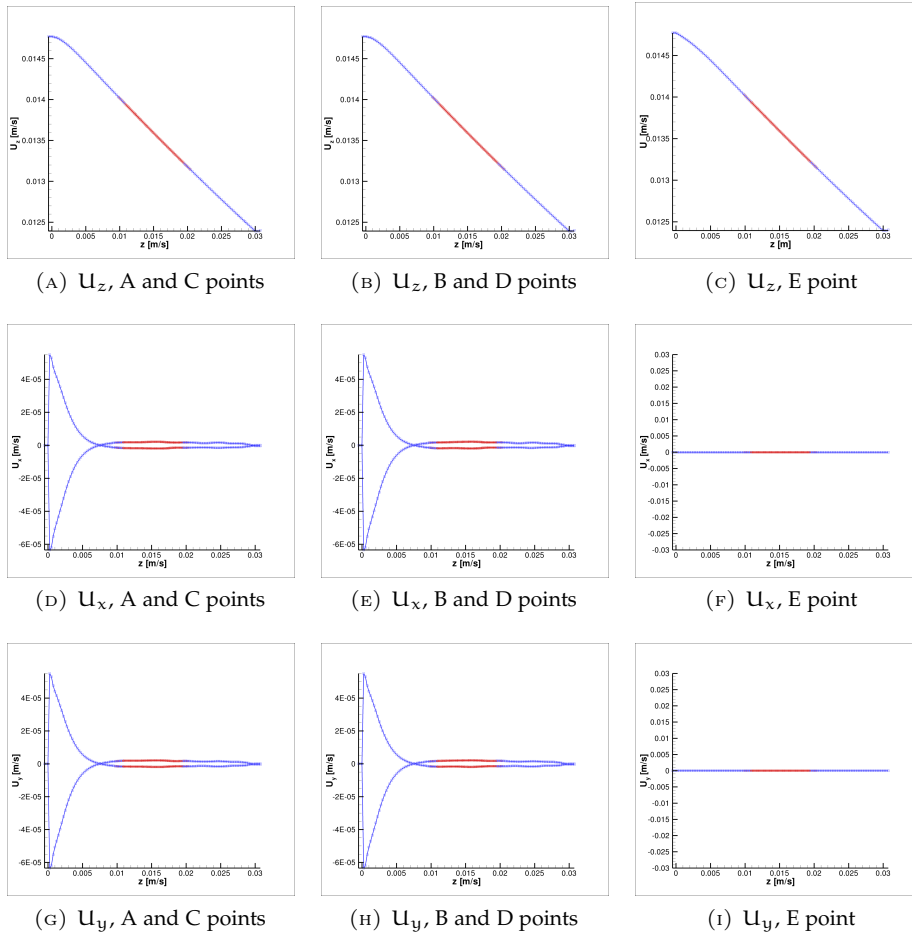
FIGURE 5.10.   Viscous flow velocity profiles, $t = 3.73 \times 10^{-4}$ s

this behaviour is caused by the development of the boundary layer on the walls, that reduce the duct section and speed up the flow.

Also in this test case, the connection between the different resolution zones doesn't alter the flow field.

In figure 5.12 on page 61 are illustrated two-dimensional slides of the U_z velocity component: the iso-surfaces remain orthogonal to the direction of the flow while the jet propagates into the duct; in figure 5.12d on page 61 is evident the development of the boundary layer and the speed-up of the flow next to the walls: the iso-surface isn't orthogonal to the direction of the flow and the U_z velocity component is greater at the corners than at the center of the field.

5.2.1.3 Parabolic Jet

Also this case has a central symmetry respect to the z axis that passes through the E point: the symmetry is maintained when the flow passes the borders between coarse and fine zones, as can be seen in figures 5.13a, 5.13b.

(A) U_z, A and C points   (B) U_z, B and D points   (C) U_z, E point

(D) U_x, A and C points   (E) U_x, B and D points   (F) U_x, E point

(G) U_y, A and C points   (H) U_y, B and D points   (I) U_y, E point
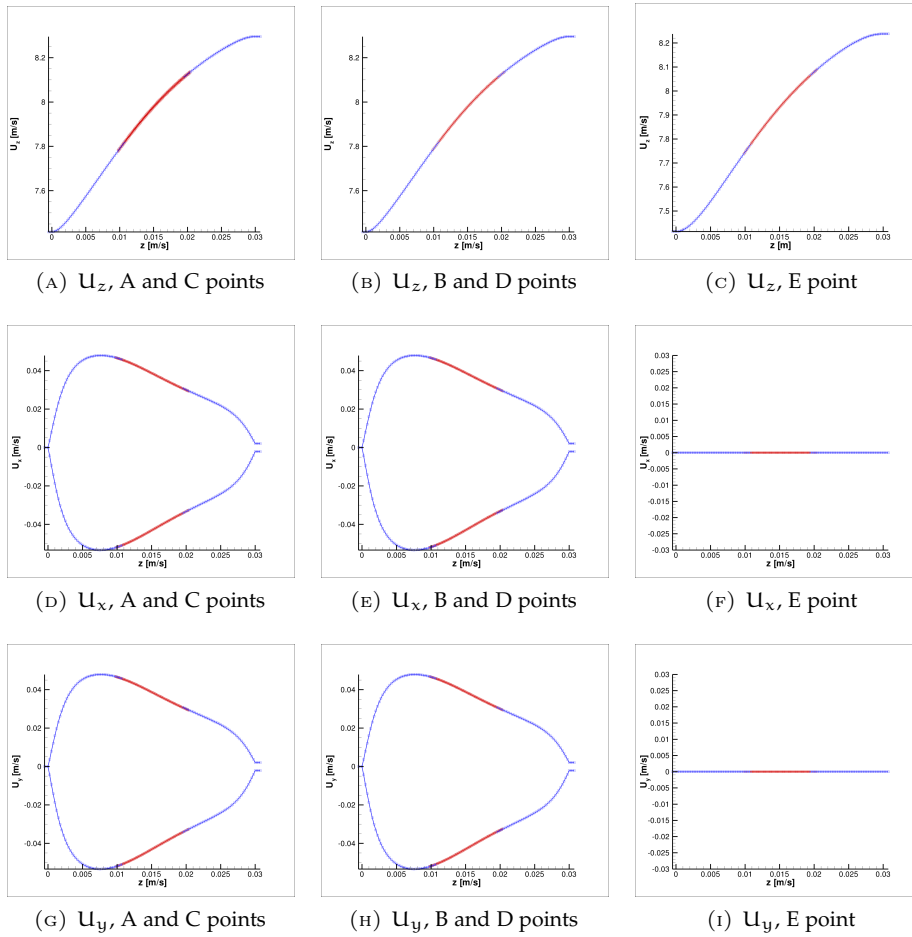
FIGURE 5.11.   Viscous flow velocity profiles, $t = 7.37 \times 10^{-3}$ s

(A) U_z, $t = 1.0 \times 10^{-3}$ s

(B) U_z, $t = 3.0 \times 10^{-3}$ s

(C) U_x, $t = 5.0 \times 10^{-3}$ s

(D) U_x, $t = 8.0 \times 10^{-3}$ s
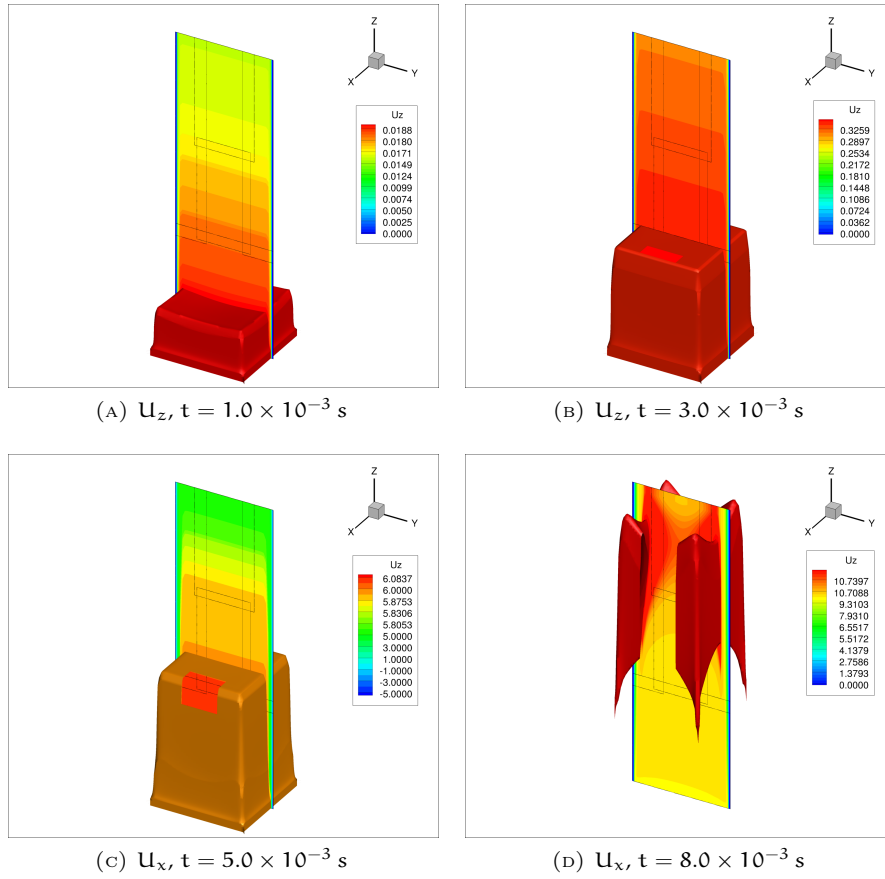
Figure 5.12.   Viscous flow velocity 2D slides

(A) U_z, A and C points

(B) U_z, B and D points

(C) U_z, E point

(D) U_x, A and C points

(E) U_x, B and D points

(F) U_x, E point

(G) U_y, A and C points

(H) U_y, B and D points

(I) U_y, E point
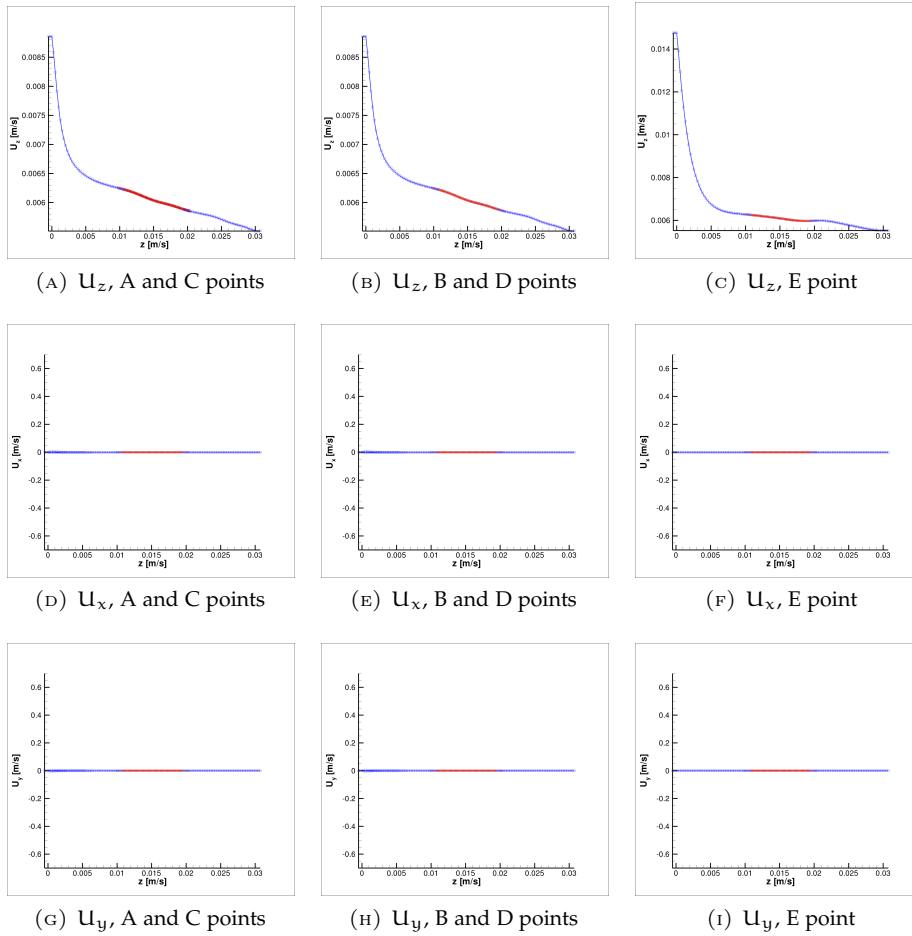
FIGURE 5.13.   Parabolic flow velocity profiles, $t = 3.73 \times 10^{-4}$ s

When the parabolic flow starts to propagate into the duct, two vortexes appear in front of the parabolic profile: the counter-rotating vortexes motion isn't altered by the coarse-fine grid communications. At the center of the duct, the spanwise and crosswise velocities remain null (figures 5.14f and 5.14i).

In figure 5.15 on page 64 are illustrated two-dimensional slides of the U_z velocity component: the parabolic profile isn't altered when passes through the coarse-fine and fine-coarse grid interfaces and in figure 5.15d on page 64 the parabolic front is exited from the outlet and the entire flow field has a central symmetry.

(A) U_z, A and C points   (B) U_z, B and D points   (C) U_z, E point

(D) U_x, A and C points   (E) U_x, B and D points   (F) U_x, E point

(G) U_y, A and C points   (H) U_y, B and D points   (I) U_y, E point
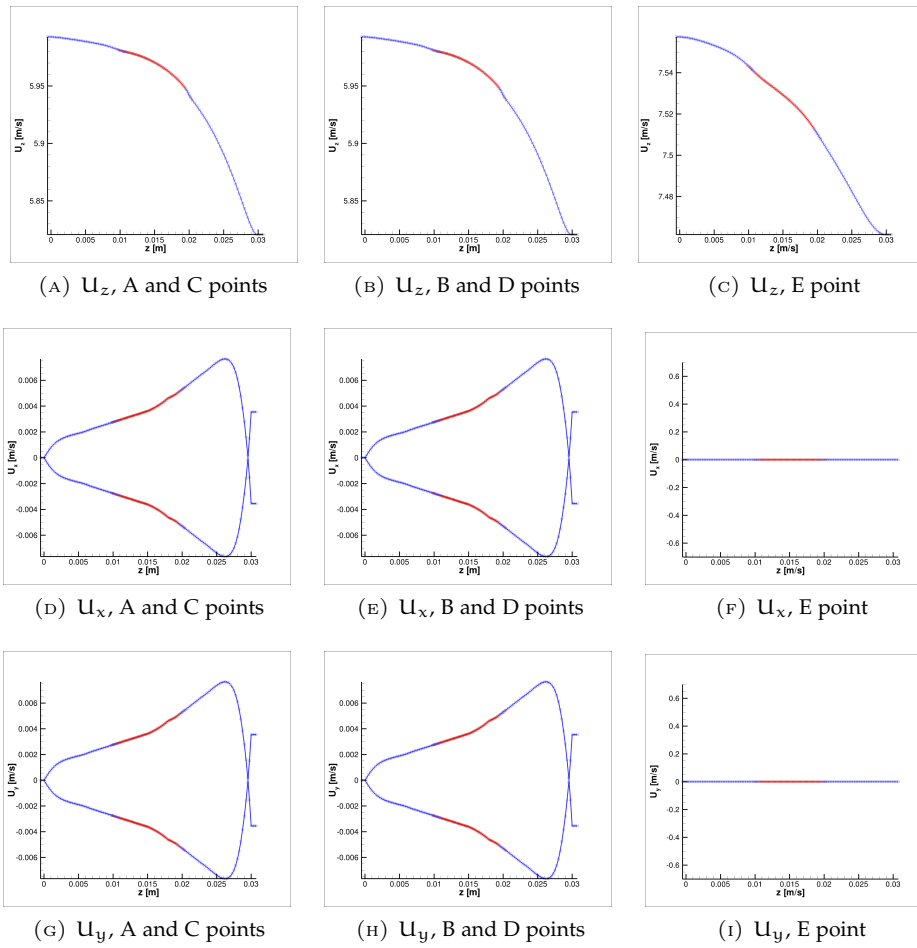
FIGURE 5.14.   Parabolic flow velocity profiles, $t = 7.37 \times 10^{-3}$ s

(A) U_z, $t = 1.0 \times 10^{-3}$ s

(B) U_z, $t = 3.0 \times 10^{-3}$ s

(C) U_x, $t = 5.0 \times 10^{-3}$ s

(D) U_x, $t = 8.0 \times 10^{-3}$ s
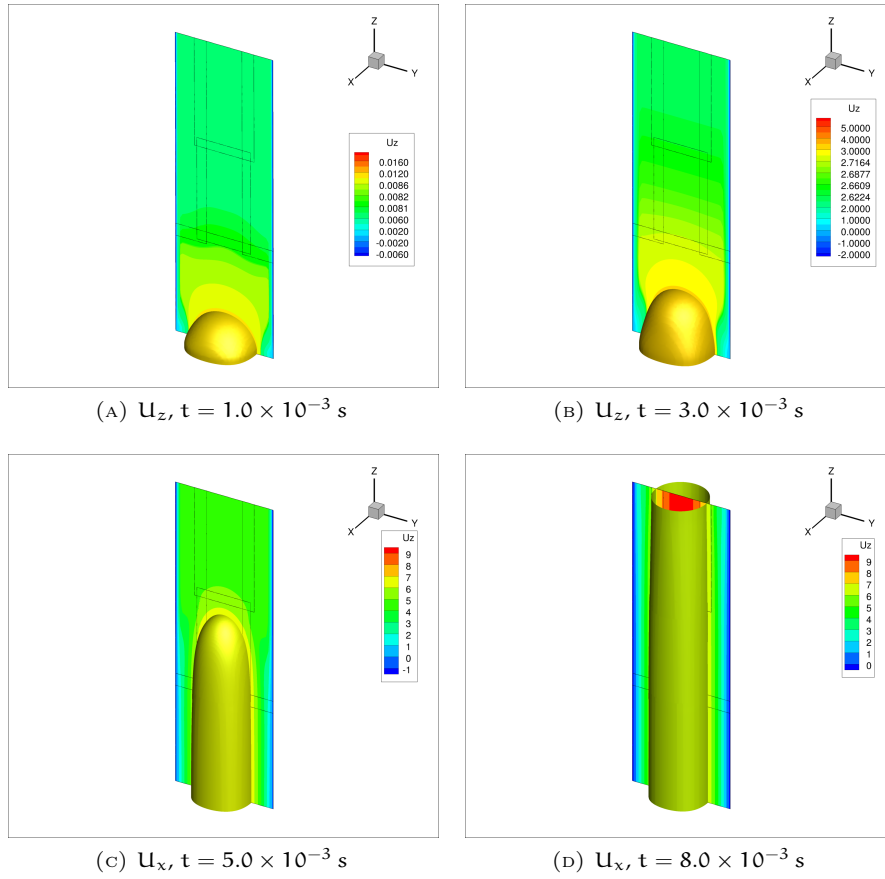
FIGURE 5.15.   Parabolic flow velocity 2D slides

6

VALIDATION

T HE validation is a fundamental phase for the development of a numerical code. In this chapter the numerical simulations of a significant test case, obtained with the joined-grids technique, are presented: a Large Eddy Simulation of a lean premixed CH_4/H_2–Air slot flame.

6.1 LEAN PREMIXED CH_4/H_2–AIR COMBUSTION

In the last few years, exceptional attention in high efficiency and low pollutants emissions is been addressed in many practical devices, such as gas turbines or propulsive systems, because of increasingly stringent pollutant emissions limits and fuel shortages: for this purpose a new class of burners is been developed, in which hydrocarbon-based fuel and oxidizer mixture is very lean. In such way, beyond a less fuel consumption, CO_2 and NO_x emissions are reduced (substantially thanks to higher efficiencies and lower temperatures of combustion).

Unfortunately, combustors that operate at leaner conditions generate high levels of combustion dynamic stems from the fact that their design goals are also ideal for promoting combustion instabilities: they operate very near the blowout point, where the flame is thicker and propagate more slowly; furthermore, high mixture inlet velocity (necessary to avoid flashback phenomena) can stretch flame front, causing heat losses and local flame extinction.

In order to overcome these issues, it is possible to add a small percentage of hydrogen to the lean premixed hydrocarbon–air mixture: with no design changes, a small percentage of H_2, thanks to its very wide flammability range, can extend the stable combustion regime, thus allowing stable operation at the lower temperatures needed to reduce oxides of nitrogen. Hydrogen addition can also reduce quenching distance (very important in safety and micro-combustion issues, because this distance is directly related to the flashback risk) and increase flame propagation velocity, due to the faster reaction rates of the H_2/O_2 system and to the larger diffusion coefficient of H_2. However, hydrogen also if has an higher heat of combustion relative to hydrocarbon fuels on a per unit mass basis, due to its lower density, has a lower heating value on a per unit volume (about a factor four less than CH_4).

65

The use of HENG (Hydrogen-Enriched Natural Gas) appears to be an economically sustainable solution to reduce the carbon intensity of natural gas, considering its compatibility with current transmission, distribution and energy production infrastructure (up to an hydrogen percentage of 20%); it is however observed that, depending on the gasification process and on which solid is used in the gasification process, substantial differences in the resulting syngas composition occur: these differences can modify the combustion properties, like flame speed, flammability limits and ignition delay time. All these issues increase the variability of fuel composition at the inlet of gas turbine combustors, thus increasing the risk of thermo-acoustic instabilities in gas turbine combustors and leading to the need for more fuel-flexible gas turbines.

For turbulent flames with hydrogen added to methane the literature is limited: we mention some experimental studies [Schefer et al., 2002; Cozzi and Coghe, 2006; Mandilas et al., 2007; Halter et al., 2007], the LES of [Hernandez-Perez et al., 2013] and the LES of [Giacomazzi et al., 2014], from which the present test case is been inspired.

6.2 Problem Configuration and Simulation Setup

The simulations were performed in a slot-burner Bunsen flame configuration, that is especially interesting due to the presence of mean shear in the flow and is similar to the burner used in the experimental studies by [Filatyev et al., 2005]. This configuration consists of a central jet of premixed reactants that is surrounded on either side by a heated coflow, whose composition and temperature are those of the complete combustion products of the reactant jet mixture. The size of the three adjacent slot burners is undefined in the crosswise (x) direction, and they are separated along the spanwise (y) direction by means of two $0.17\,\mathrm{mm}$ thick walls.

The premixed jet is a mixture of methane/hydrogen air jet at $600\,\mathrm{K}$, with equivalence ratio $\phi = 0.7$ and molar fraction distribution of 20% H_2 and 80% CH_4; the unstrained laminar flame properties at these conditions have been computed using LaminarSMOKE [Cuoci et al., 2013] and summarized in table 6.1 on the next page, where ϕ is the multicomponent equivalence ratio

$$\phi = \frac{\left[\left(X_{H_2} + X_{CH_4}\right)/X_{O_2}\right]}{\left[\left(X_{H_2} + X_{CH_4}\right)/X_{O_2}\right]_{stoich}}$$

T_u is the unburned gas temperature, T_b is the product gas temperature, s_L is the unstrained laminar flame speed and δ_{th} is the thermal thickness based in maximum temperature gradient

$$\delta_{th} = \frac{(T_b - T_u)}{|\partial T/\partial x|_{max}}$$

Preheating the reactants leads to a higher flame speed and allows an higher inflow velocity without blowing out the flame, reducing computational costs; also, many practical devices such as gas turbines operate at highly preheated conditions.

Table 6.1. CH_4/H_2–Air Laminar Flame

ϕ	$n_{H_2} = x_{H_2}/(x_{H_2} + x_{CH_4})$	T_u (K)	T_b (K)	s_L (cm s^{-1})	δ_{th} (mm)
0.7	0.2	600	2072	92.85	0.436

Table 6.2. Simulation Setup

Slot width (h)	1.2 mm
Domain size in the crosswise (x), spanwise (y) and streamwise (z) directions	$2.5h \times 29h \times 32.5h$
Total grid points	2 416 950
Fine grid points	2 116 320
Fine grid size (inlet excluded) in the crosswise, spanwise and streamwise directions	$2.5h \times 8.7h \times 17.15h$
Minimum grid space	3.5×10^{-2} mm
Turbulent jet velocity	110 m s^{-1}
Coflow velocity	25 m s^{-1}
Jet Reynolds number ($Re_{jet} = Uh/\nu$)	2264
Turbulent intensity (u'/S_L)	12.5
Turbulent length scale (l_t/δ_l)	2.6
Turbulent Reynolds number ($Re_t = u'\eta/\nu$)	226
Damköhler number ($s_L L_t/u'L$)	0.21
Karlowitz number (δ_L/η_k)	22

The reduced skeletal scheme adopted in the simulation [Sankaran et al., 2007] is based on 17 species (CH_4, CH_3, CH_2, CH, CH_2O, HCO, CO_2, CO, H_2, H, O_2, O, OH, HO_2, H_2O_2, H_2O, N_2) and 57 reactions. This scheme, compared to the detailed GRI-MECH 3.0 scheme [Smith et al.] by looking at their laminar freely propagating flame solutions obtained by using the CHEMKIN code [Kee et al., 1998] and neglecting the Soret effect, shows maximum errors of ~ 4% and ~ 6% for the laminar flame velocity and temperature, respectively.

The simulation parameters are summarized in table 6.2: the domain size in the crosswise (x), spanwise (y), and streamwise (z) directions is $L_x \times L_y \times L_z = 2.5h \times 29h \times 32.5h$, where h = 1.2 mm is the slot width; the grid is uniform only in the x direction, with $\Delta x = 5.0 \times 10^{-2}$ mm for the fine level and $\Delta x = 1.0 \times 10^{-1}$ mm for the coarse level, while is stretched in the y and z directions near the inlet duct walls (see figure 6.1 on the next page).

The grid has been created starting from the grid already used in a previous LES performed on the same test case by means of HeaRT code [Giacomazzi et al., 2014]: in the central reaction zone, the new grid is the same of the grid used in the previous simulation; the side and the upper zones (where flow field is calm), are obtained from the "old" grid deleting every other point, in each direction.

The simulation was run at atmospheric pressure using a 17 species chemical mechanism. The velocity of the central jet is 110 m s^{-1}, while the velocity of the coflow stream is 25 m s^{-1}; the width of the central duct, where the inlet turbulent velocity profile may develop is h =1.2 mm and 4 mm long.
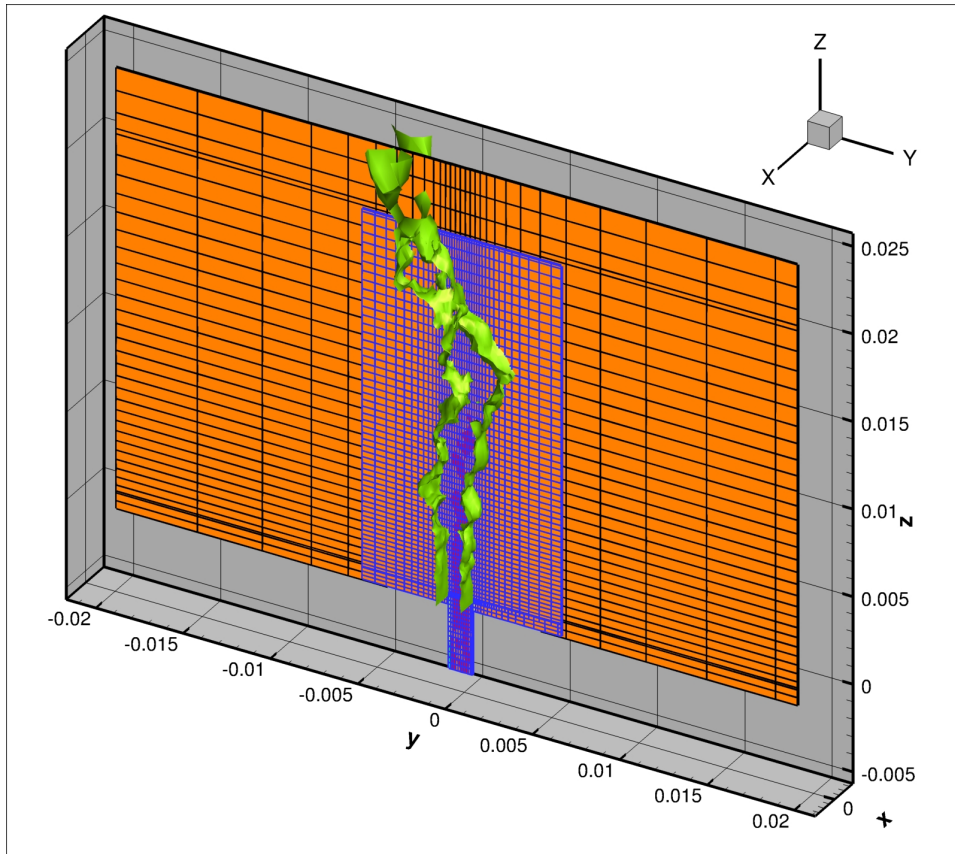
FIGURE 6.1. Domain configuration with computational coarse (black) and fine (blue) grids (only one line each four is represented); iso-surface of temperature T = 1600 K

Velocity fluctuations, $u' = 12\,\mathrm{m\,s^{-1}}$, are imposed on the mean inlet velocity profile, obtained by generating at duct's inlet homogeneous isotropic turbulence field with a characteristic turbulent correlation scale in the streamwise direction of $4 \times 10^{-4}\,\mathrm{m}$, by means of Klein's procedure [Klein et al., 2003].

The Reynolds number based on the centerline inlet velocity, slot width h and kinematic viscosity $5.3 \times 10^{-5}\,\mathrm{m^2\,s^{-1}}$ is $Re_{jet} = Uh/\nu = 2264$; based on the centerline jet velocity and the streamwise domain length, the flow through time is $\tau_U = 39\,\mathrm{ms}$.

The central jet turbulent Reynolds number is 226, based on the rms velocity fluctuation ($12\,\mathrm{m\,s^{-1}}$), the integral scale ($1\,\mathrm{mm}$) and the previous kinematic viscosity; The Kolmogorov length scale is $\eta = 17.22\,\mathrm{\mu m}$. The adiabatic flame temperature is $2072\,\mathrm{K}$ and at these conditions laminar flame speed is $s_L = 0.96\,\mathrm{m\,s^{-1}}$ and laminar flame front thickness is $\delta_L = 0.386\,\mathrm{mm}$.

In x direction periodic boundary conditions are imposed, in z direction NSCBC (Navier-Stokes Characteristic Boundary Conditions) are imposed, in order to obtain non-reflecting inlet and outlet boundary conditions, and in y direction viscous and adiabatic walls boundary conditions are imposed. The subgrid scale model adopted for the turbulence closure is the dynamic Smagorinsky model.

6.3 SIMULATION RESULTS

In figure 6.3 on the following page mean (6.3a) and instantaneous (6.3b) temperature contours are represented: the flame front is anchored at the corner between inlet duct and center reaction zone, and considering the Damköhler number, the Kolmogorov length scale and the laminar flame thickness values, turbulence of the flow field strongly influences the flame structure: this flame is in the thin reaction zone regime (as can be seen also in figure 6.2, where the combustion regimes are identified in terms of length and velocity ratio on logarithmic scales in the black area).
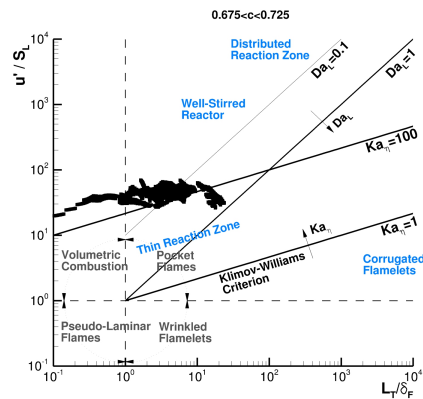
FIGURE 6.2. Borghi Diagram

The influence of turbulence can also be seen in figure 6.4 on the next page, in which mean (6.4a) and instantaneous (6.4b) streamwise velocity contours are represented: as can be seen from streamtraces in figure 6.4a, the channel boundary layer takes in the section of the inlet and for this reason the streamwise velocity is greater than its inlet value; this is well-rendered also in figure 6.5a, where the continuous black line reach a maximum value of $110\,\mathrm{m\,s^{-1}}$.

The velocity fluctuations are greater around the shear layer between cold flow and hot flow, also because of the heat released by the flame; the expansion of the CH_4/H_2–Air mixture jet at the end of the inlet duct and the coflow motion

(A) Mean Temperature Contour

(B) Instantaneous Temperature Contour
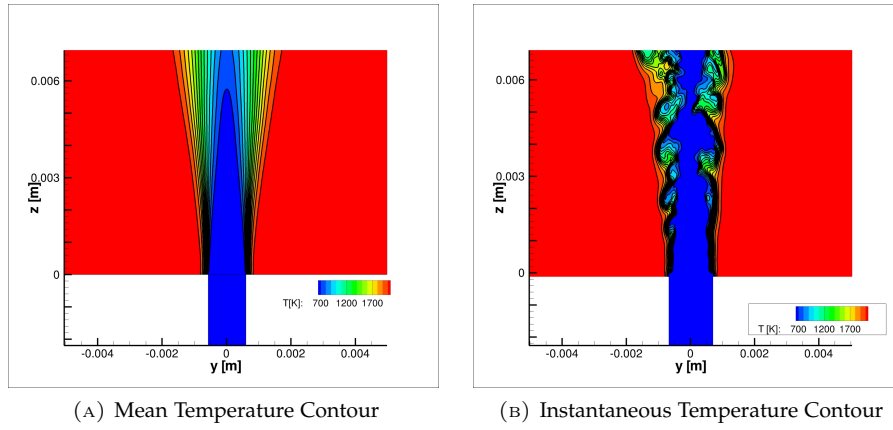
Figure 6.3. Temperature Contours

(A) Mean Velocity Contour

(B) Instantaneous Velocity Contour
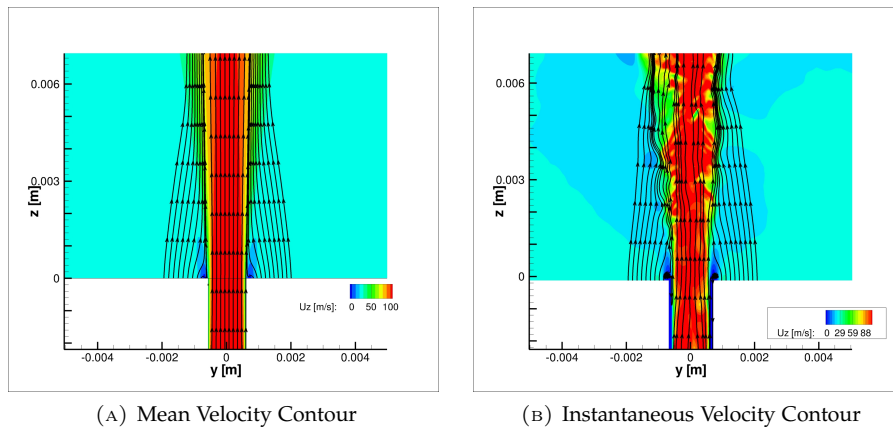
Figure 6.4. Streamwise Velocity Contours

(A) Mean Streamwise Velocity Profile

(B) rms Streamwise Velocity Profile
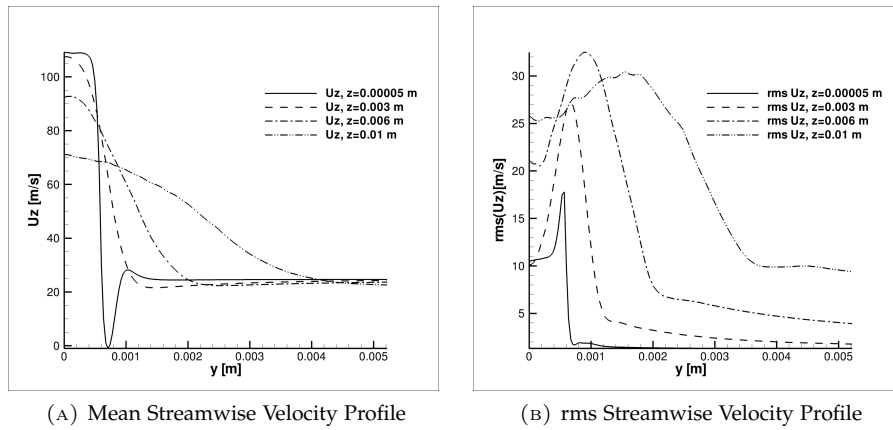
Figure 6.5.   Streamwise Velocity Profiles

(A) Mean Spanwise Velocity Profile

(B) rms Spanwise Velocity Profile
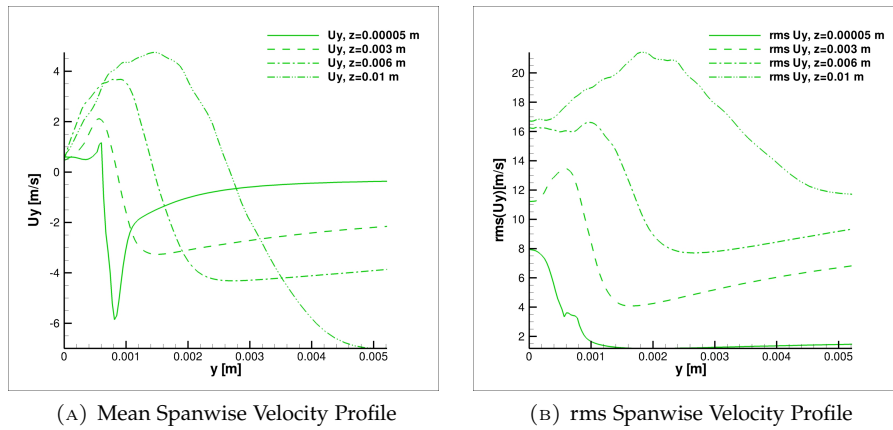
Figure 6.6.   Spanwise Velocity Profiles

towards the cold jet core can be seen in figure 6.6, where the spanwise mean and rms velocity profiles are plotted: moving towards the walls from the flame front, spanwise velocity is negative, while is positive into the jet; from figure 6.6a can also be seen that the flame front broadens in the spanwise direction when the flow moves towards outlet in streamwise direction: U_y becomes less than 0 for increasing values of the streamwise coordinate distance z.

Downstream the injection point the separation between the cold jet and the hot coflow is evident, as can be seen in figure 6.7a on the next page, where the mean temperature profile is plotted; at $h = 3\,mm$ the temperature at the center of the flow field starts to raise from $600\,K$ and reaches the maximum of about $1000\,K$ at $h = 10\,mm$, thanks to the heat released from the flame front. The rms temperature profiles in figure 6.7b on the following page show that temperature peak moves towards the external of the jet because at higher quotes the flame broadens and the flam front oscillations are greater.

71

(A) Mean Temperature Profile

(B) rms Temperature Profile
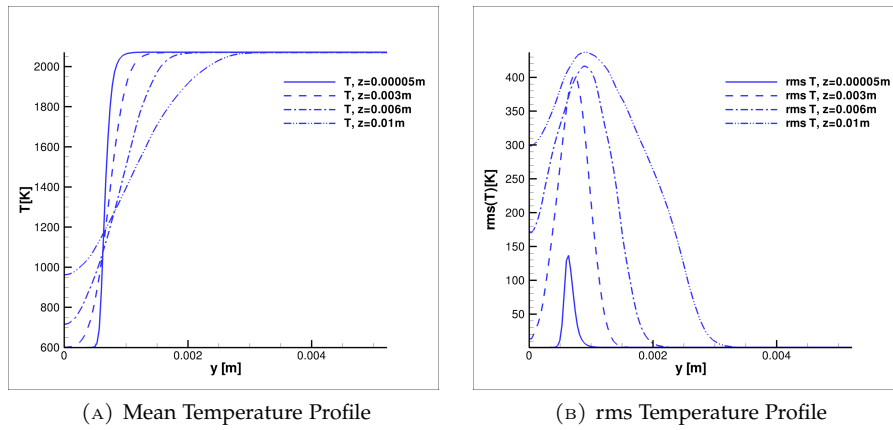
Figure 6.7. Temperature Profiles

(A) Mean Pressure Profile

(B) rms Pressure Profile
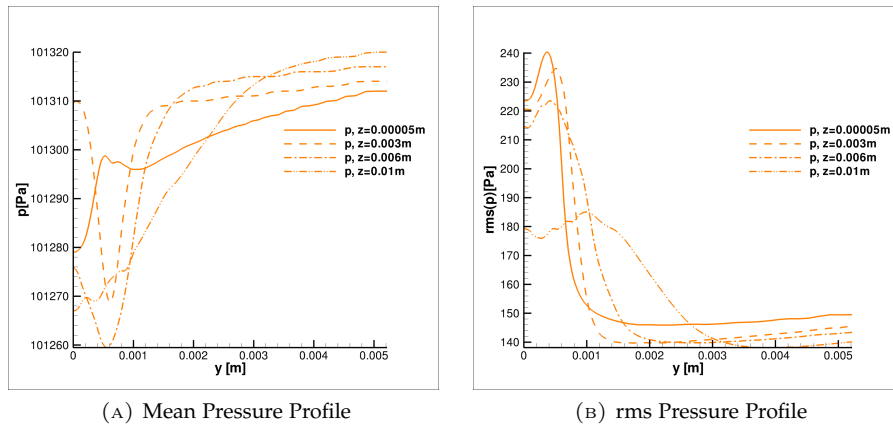
Figure 6.8. Pressure Profiles

The pressure field is strongly conditioned by the flame front oscillations and by the heat release from the flame, as can be seen in figure 6.8a: the minimum of the mean pressure profile decreases as the height from the injection point increases; the minimum, moreover, moves towards the y direction. At the maximum height ($h = 1\,cm$) the mean pressure profile shows a different trend respect to the three other quotas, and this behaviour is also noticeable in figure 6.8b (where the rms pressure profiles are plotted): the motion of the flame front reduces the pressure rms peak.

In figure 6.9 on the next page, mean profiles of four species (H_2, CH_4, CO and OH) are plotted: the fast reaction rate and the high diffusion coefficient of H2 is evident for the lower quota, where as the hydrogen encounter high temperature combustion products it burns instantaneously and its concentration decreases very quickly (see figure 6.9a); the higher flame propagation velocity due to the hydrogen can be seen also from the steep fall of the methane concentration at the lower quota in figure 6.9b; CH4 is always totally burnt before the hydrogen.

(A) Mean H_2 Profile

(B) Mean CH_4 Profile

(C) Mean CO Profile

(D) Mean OH Profile
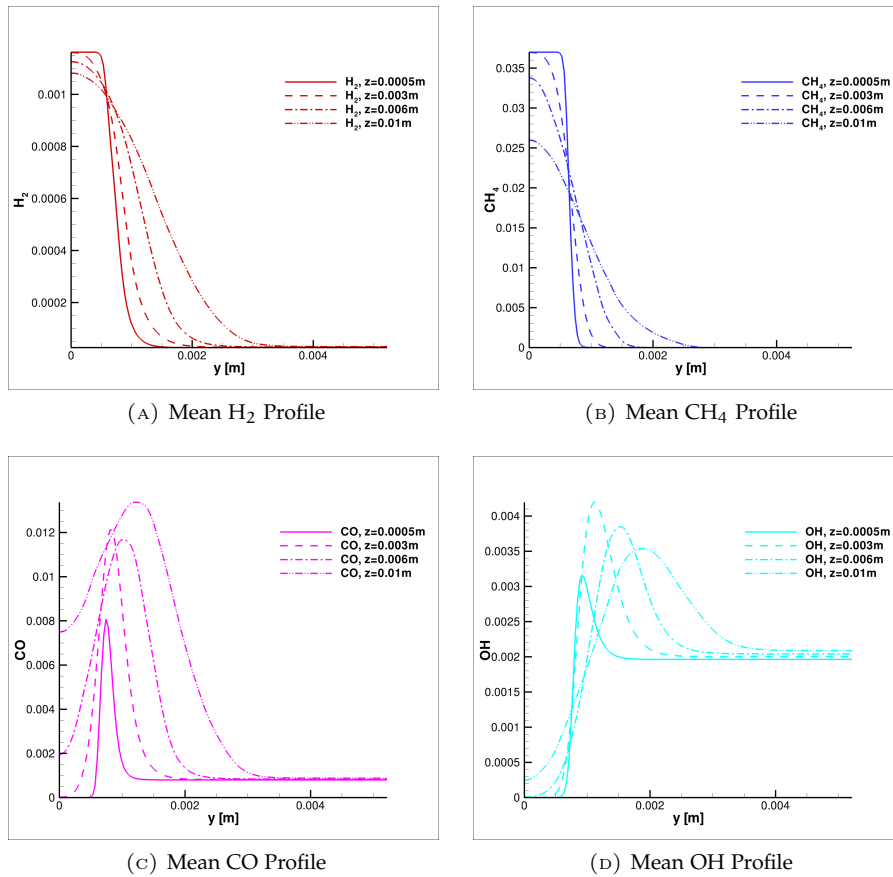
Figure 6.9. H_2, CH_4, CO and OH Mean Profiles

From these figures is also evident that CO has an higher diffusion velocity respect to the OH, which concentration remains very low at the center of the cold jet also for high quotas (see figures 6.9c and 6.9d); moreover, CO mean peak is always at a lower distance from the center of the cold jet than the OH mean peak: CO is therefore produced at an higher velocity than the OH in the chemical reactions that take place in the flame front.

6.3.1 "Old" LES Data Comparison

In this section, comparison between the numerical simulation described in section 6.3, a second multi-resolution numerical simulation, the previous LES [Giacomazzi et al., 2014] and a DNS [Cecere et al., 2015] are illustrated; all the three numerical simulations are performed by means of HeaRT numerical code, with numerical models described in chapter 3, on the computational domain described in table 6.2: the difference between the runs is obviously the presence of the joined-grid algorithm in the first two simulations, and therefore a different computational grid; the four configurations are summarized in table 6.3.

Table 6.3. Grid comparison between the previous simulation (Single Level) and the actual simulations (Joined Grids)

	DNS	Single Level (SL)	Two Levels (JG2)	Three Levels (JG3)
Computing blocks (for level)	4	4	5 (1), 4 (2)	3 (1) 3 (2), 4 (3)
Computing nodes	119666400	3969480	2416950	1548390
Grid levels	1	1	2	3
Grid points (for level)	119666400	3969480	234630 (1), 2116320 (2)	33030 (1), 130080 (2), 1385280 (3)

The computational grid of the second numerical simulation with joined grid approach (JG3, see figure 6.10 on the following page) is obtained from the grid described in tabular 6.2: the finest zone (level 3) has the same resolution of the level 2 of JG2 simulation, but it's smaller in y direction (4.35h) and in z direction (12.3h); outside this zone, the grid is obtained from the JG2 grid deleting every other point, in each direction: it's been possible to achieve an additional reduction for the total of computational nodes: the computational grid of JG2 simulation has about 1 500 000 nodes less than the SL grid, while the JG3 grid has about 870 000 nodes less than the JG2 grid; the JG3 computational grid has just over one third of the total nodes of SL grid.

In figures 6.12, 6.13, 6.14 average and rms profiles of streamwise velocity, spanwise velocity and temperature at several heights (illustrated in figure 6.11, where the injection is at $z = 0.00$ mm) are plotted: it is evident a very good agreement between JG2 (solid lines), JG3 (solid lines with cross), SL (dashed lines) and DNS (circles) simulation data; the communication procedures described in section 4.2.2 on page 39 don't modify both trend and maximum and minimum positions.

In figure 6.12, the transversal averages of streamwise velocity (blue lines) show the gradual opening of the central "cold" jet towards the hot gases that surround it: from the figure 6.12a to the figure 6.12f, the maximum of the averaged U_z decreases of about 30 m s^{-1} (from ~ 110 m s^{-1} to ~ 80 m s^{-1}), while the minimum of the averaged U_z increases of about 15 m s^{-1} (from ~ 20 m s^{-1} to ~ 35 m s^{-1}; this phenomena is also underlined by the transformation of the curve trend, that shows a wider bell shape.

At lower quotes, the streamwise velocity rms profiles (red lines in figures 6.12) show two well-rendered peaks at the edges of the central jet; at higher quotes (from figure 6.12d), the rms maximum value increases (up to 35 m s^{-1} and the curve shape becomes more smooth. The shape of the rms curves, furthermore, points out that at higher quotes the central jet becomes unstable and, also because of the combustion process, oscillates in the spanwise direction.

In figure 6.13, the transversal averages of spanwise velocity (blue lines) show that the hot combustion products tend to flow towards the central jet (see the two peaks near 4 m s^{-1} and -4 m s^{-1} in figure 6.13a), while the central jet flows in the opposite direction (see the two peaks near -1.5 m s^{-1} and 1.5 m s^{-1} in the same picture): at higher quotes, all these peaks move towards the transversal edges of
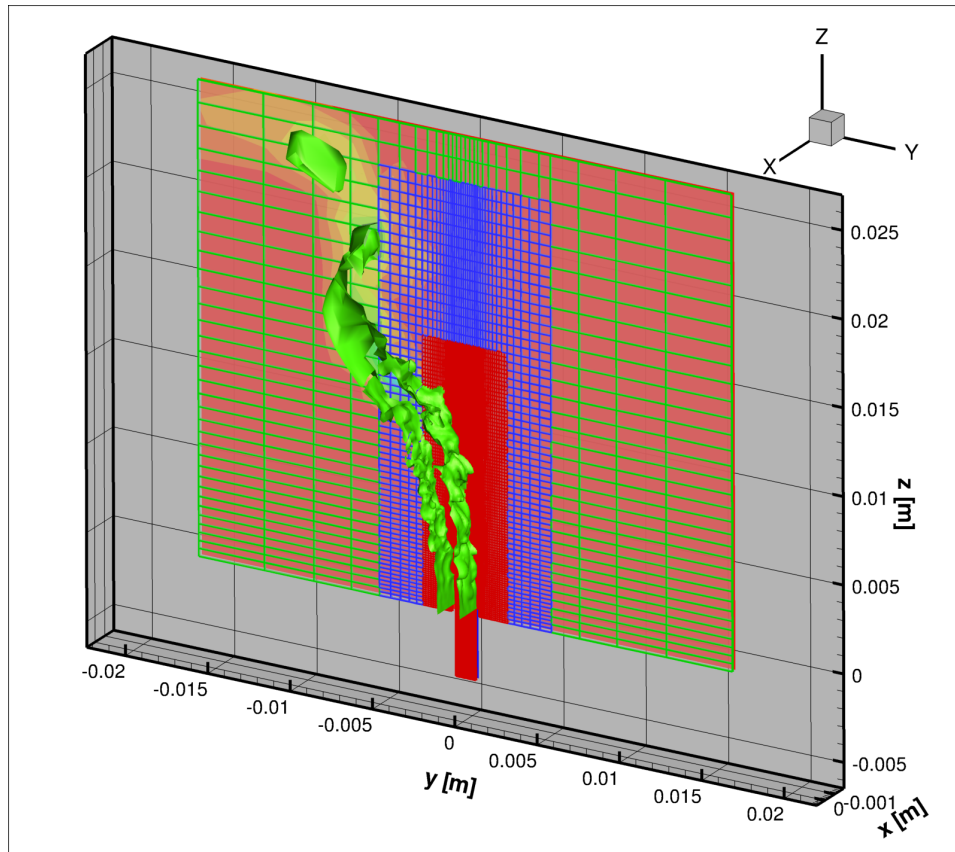
FIGURE 6.10.   Domain configuration with level 1 (green), level 2 (blue) and level 3 (red) computational grids (only one line each two is represented); iso-surface of temperature T = 1600 K
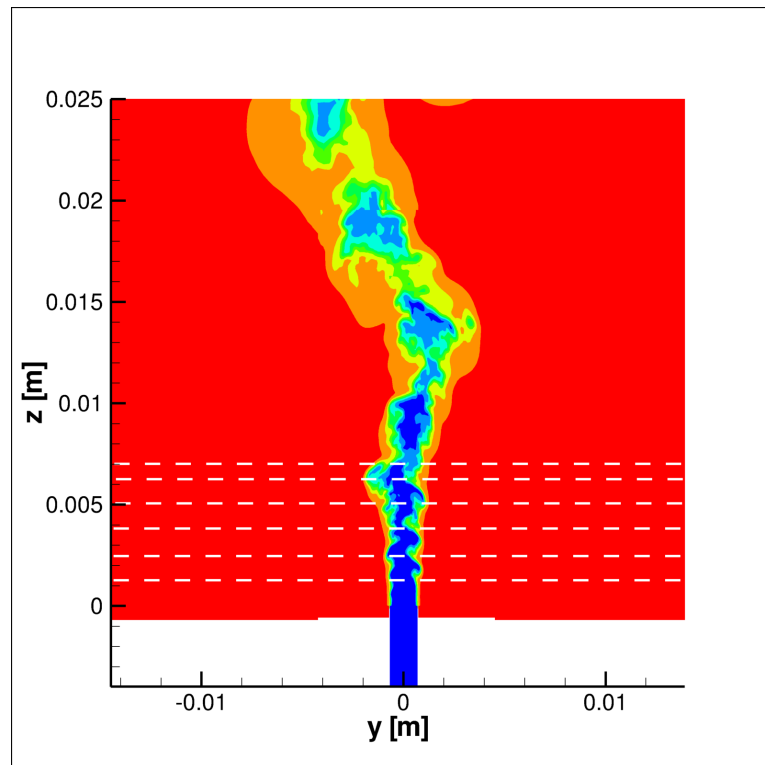
Figure 6.11. The six xy planes (white dashed lines) where JG2, JG3 and SL comparisons take place

the domain, strengthen the observation previously carried out about the opening of the central jet.

The spanwise velocity rms profiles (red lines in figure 6.13) show a gradual growth in the velocity fluctuation magnitude as the distance from the combustion chamber inlet increases; the higher fluctuations are also localized in the central high speed jet flow.

In figure 6.14, the transversal averages of temperature (blue lines) show that downstream the injection point the separation between the cold jet and the hot coflow is evident; at $h = 2.5\,mm$ the temperature at the center of the flow field starts to raise from $600\,K$ and reaches the maximum of $\sim 1200\,K$ at $h = 7.5\,mm$ (see figure 6.14f), thanks to the heat released from the flame front.

The temperature rms profiles (red lines in figure 6.14) show a behaviour similar to the streamwise velocity rms profiles, with two well-rendered peaks of $300\,K$ at the edges of the central jet, for $h = 1.25\,mm$ (figure 6.14a): these two peaks increase rapidly (at $h = 2.5\,mm$ the maximum value is close to $450\,K$) and reach the maximum value for $h = 7.5\,mm$ ($\sim 550\,K$, figure 6.14f).

In figure 6.15 average profiles at several heights above injection, for CH_4 (blue), H_2 (red), CO_2 (green), CO (purple), OH (cyan) are plotted. Also in this case is evident a very good agreement between data values obtained with the present numerical simulation (solid lines) and the "old" one (dashed lines, with symbols). The combustion products (CO and OH) diffuse in the central cold jet (the mass fraction minimum, located at the center of the flow field, increase as the quota increases), while the methane diffuses in the opposite direction: at the highest quota ($h = 7.5\,mm$, figure 6.15f), all the curves are almost flat.

In table 6.4, comparison between mean times for computing a single iteration (or time step) are reported: from the data obtained, is possible to understand that joined grids communication procedures need a deep analysis to discover and locate possible bottlenecks, cache misses and every other problem in memory management to improve computational efficiency; but is also clear that the domain decomposition algorithm currently adopted in HeaRT numerical code has to be redesigned to taking into account that computational grid is composed by blocks with different spatial resolution.

Another observation that can be made is that joined grid algorithm implemented in HeaRT code is more suitable for numerical simulation of big domains that require a very high spatial resolution in a little zone, rather than to speed up a numerical simulation of a simple domain.

Number of Cores	SL	JG2	JG3
8	28.013 47 s	26.313 07 s	22.834 56 s
16	15.356 42 s	13.535 09 s	10.398 12 s
32	8.893 72 s	8.028 20 s	7.251 65 s
64	4.782 63 s	5.288 21 s	5.127 34 s

Table 6.4. Comparison between Mean Time for a Single Iteration

77

(A) $z = 1.25$ mm

(B) $z = 2.50$ mm

(C) $z = 3.75$ mm

(D) $z = 5.00$ mm

(E) $z = 6.25$ mm

(F) $z = 7.00$ mm
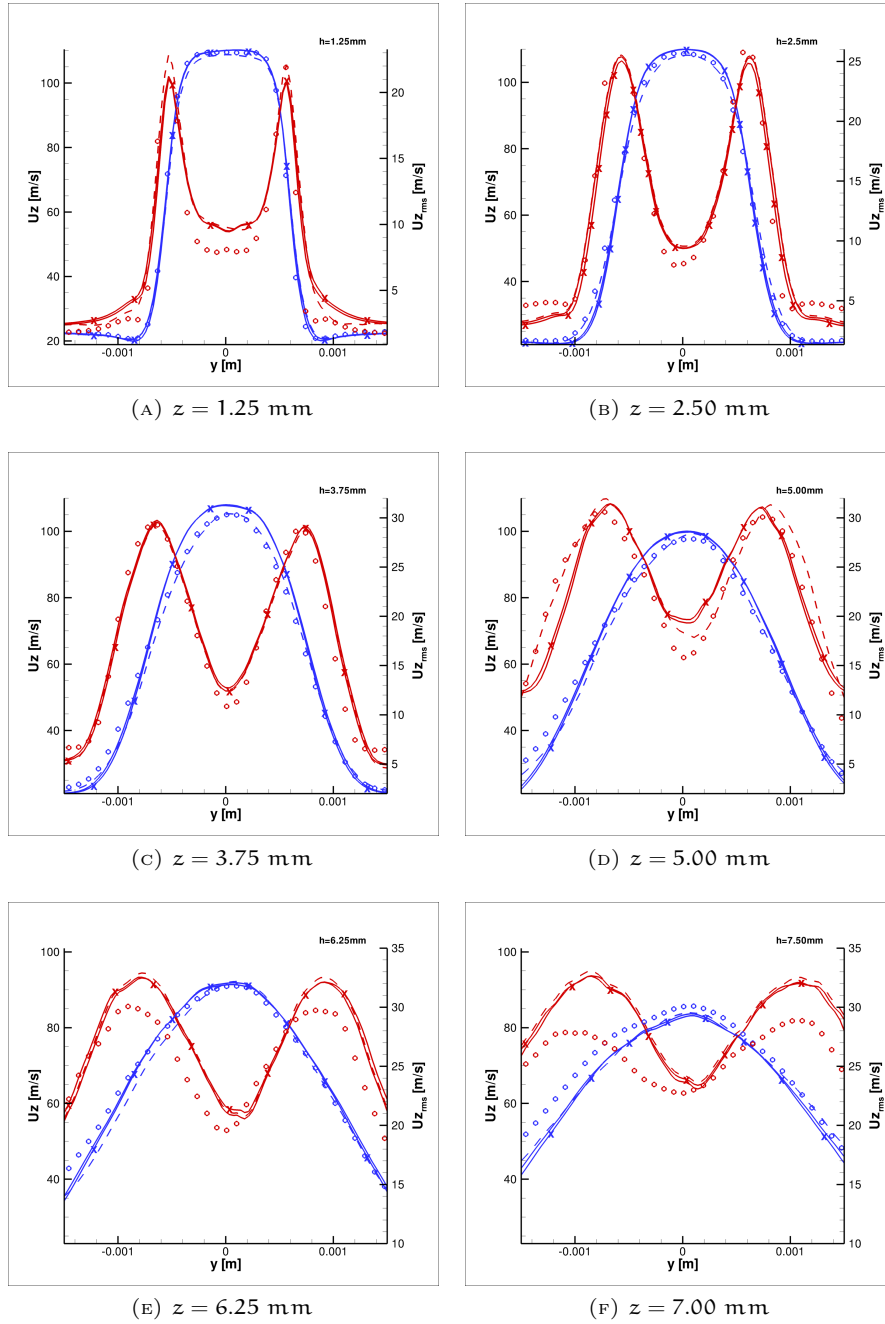
FIGURE 6.12.   Streamwise Velocity Mean (blue) and rms (red) profiles at several heights above injection: comparisons between DNS (circles), SL (dashed lines), JG2 (solid lines) and JG3 (solid lines with crosses)

78

(A) $z = 1.25$ mm

(B) $z = 2.50$ mm

(C) $z = 3.75$ mm

(D) $z = 5.00$ mm

(E) $z = 6.25$ mm

(F) $z = 7.00$ mm
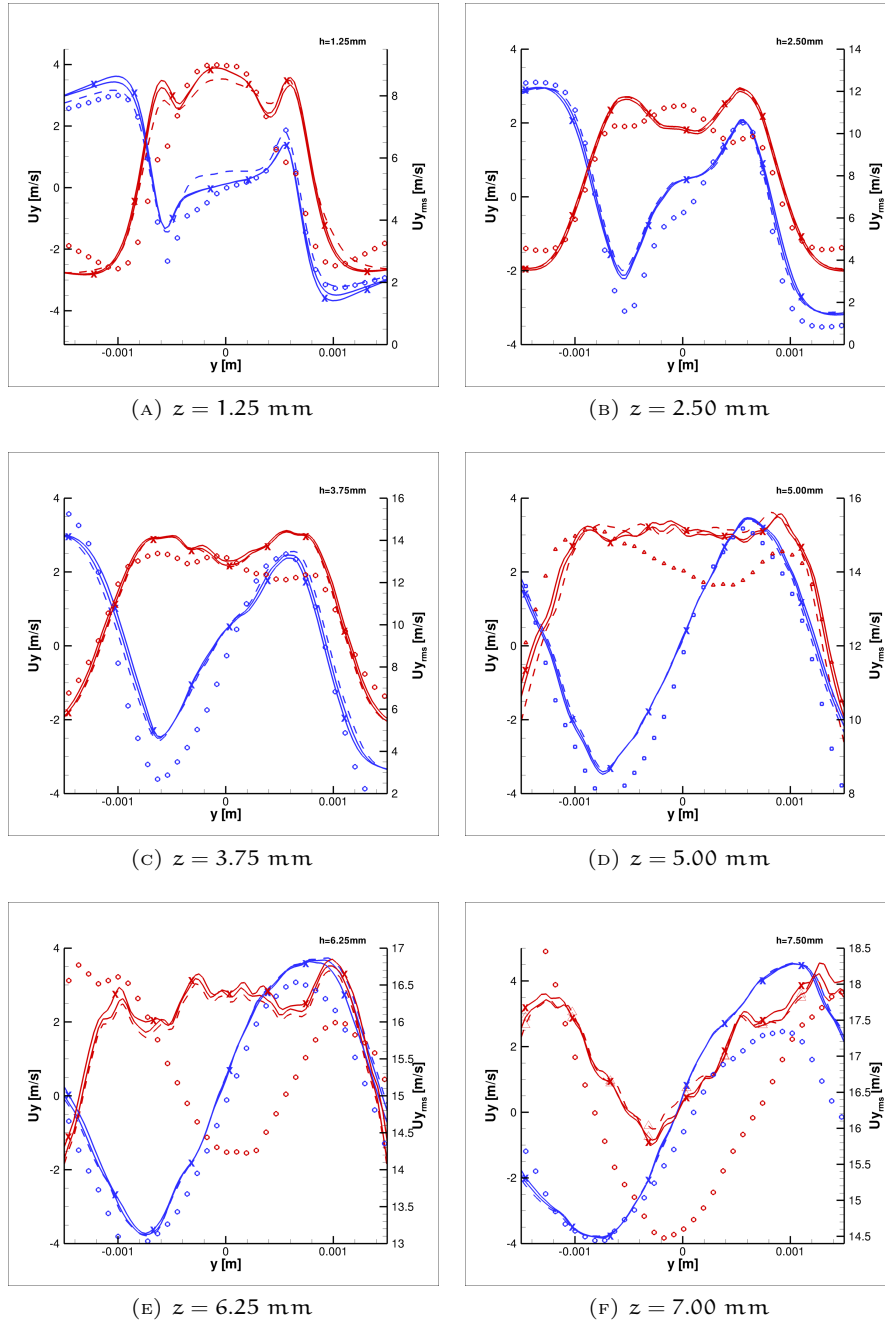
FIGURE 6.13. Spanwise Velocity Mean (blue) and rms (red) profiles at several heights above injection: comparisons between DNS (circles), SL (dashed lines), JG2 (solid lines) and JG3 (solid lines with crosses)

79

(A) $z = 1.25$ mm

(B) $z = 2.50$ mm

(C) $z = 3.75$ mm

(D) $z = 5.00$ mm

(E) $z = 6.25$ mm

(F) $z = 7.00$ mm
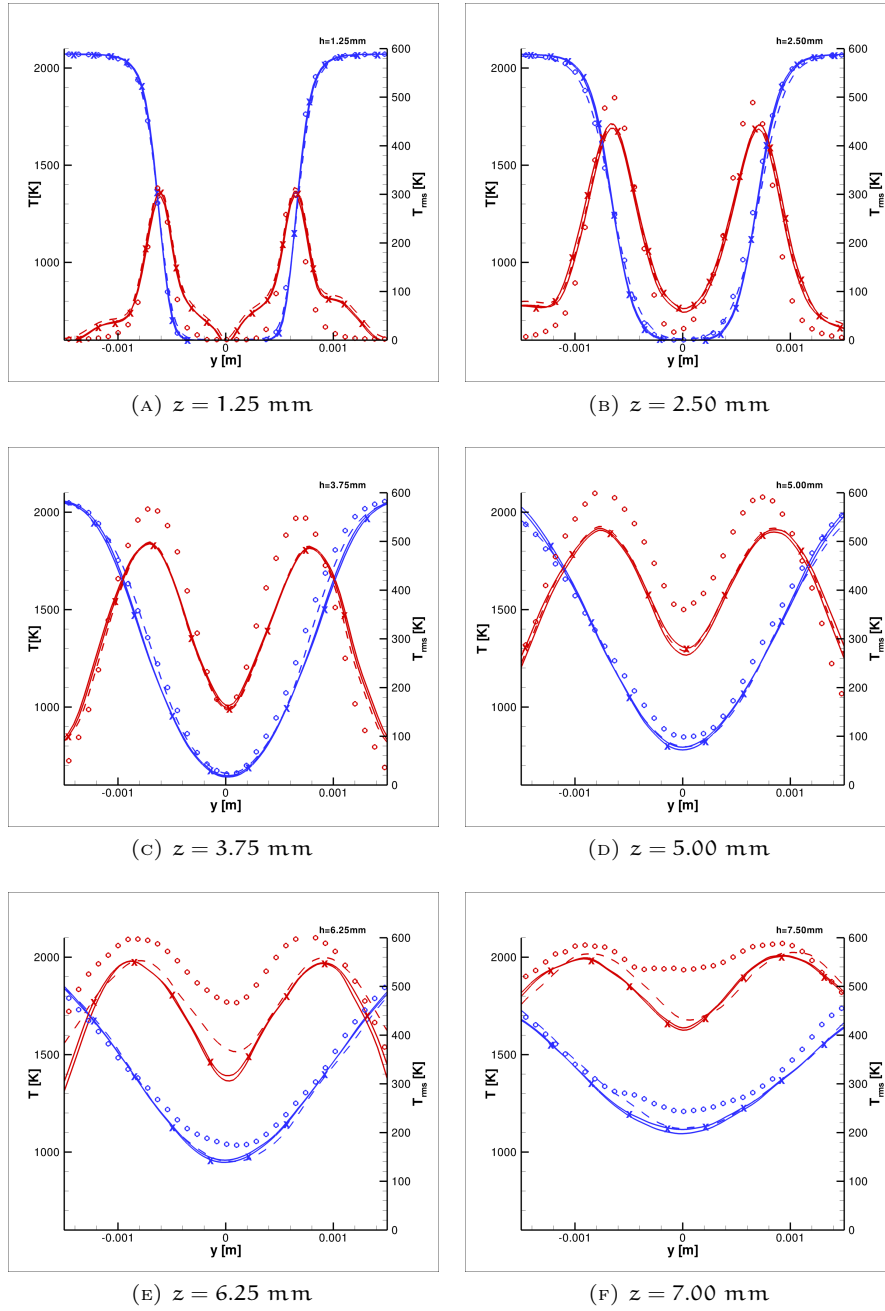
FIGURE 6.14.   Temperature Mean (blue) and rms (red) profiles at several heights above injection: comparisons between DNS (circles), SL (dashed lines), JG2 (solid lines) and JG3 (solid lines with crosses)

(A) $z = 1.25$ mm

(B) $z = 2.50$ mm

(C) $z = 3.75$ mm

(D) $z = 5.00$ mm

(E) $z = 6.25$ mm

(F) $z = 7.00$ mm
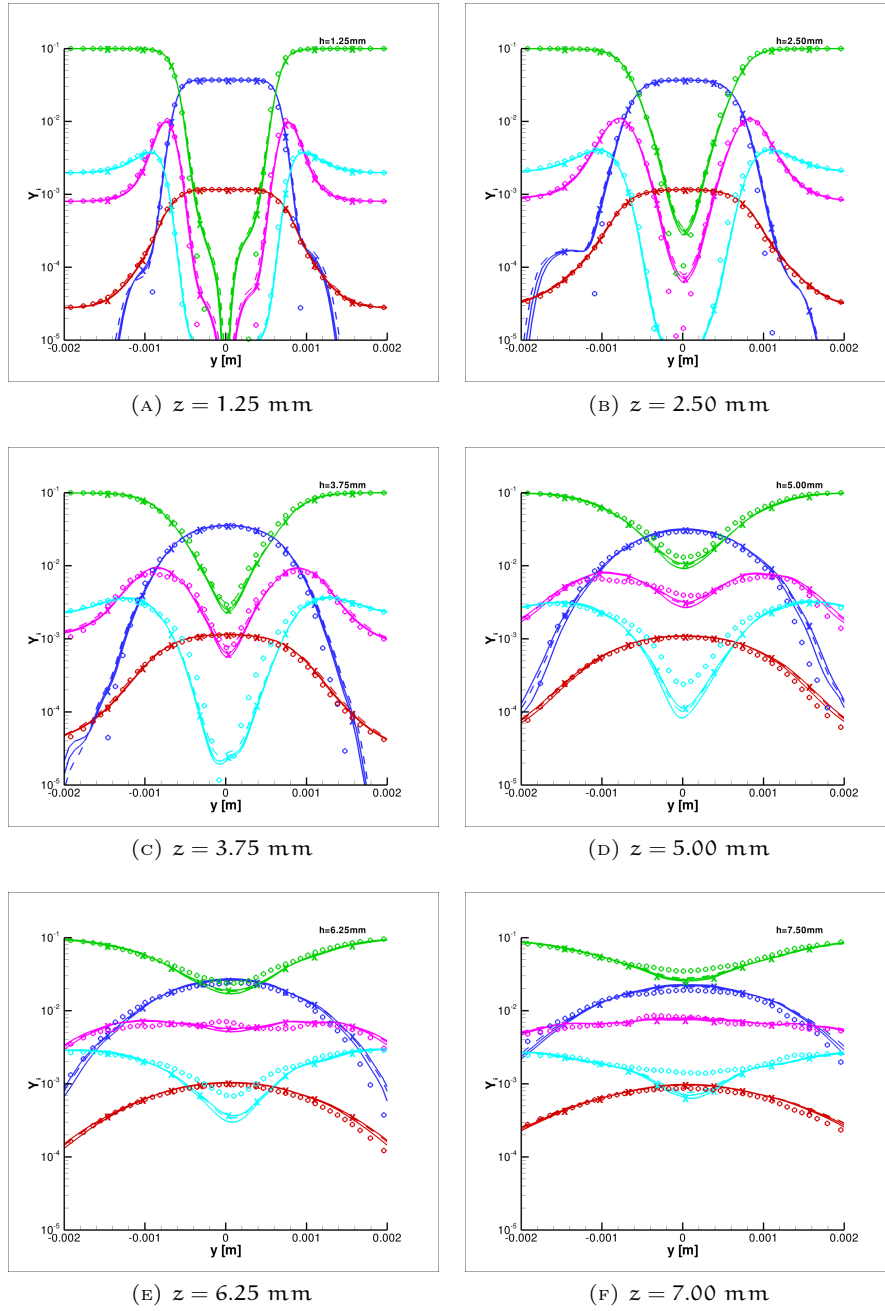
FIGURE 6.15. Mass Fraction profiles at several heights above injection: comparisons between DNS (circles), SL (dashed lines), JG2 (solid lines) and JG3 (solid lines with crosses) for CH_4 (blue), H_2 (red), CO_2 (green), CO (purple), OH (cyan)

6.3.2 Flame Curvature Statistics

In this section, a more in detail description of the flame is provided, analyzing its curvature and shape-factor at different iso-c surfaces and heights. The analysis is based on the progress variable c, defined as a normalized sum of S species mass fractions, with S={H_2, CO_2, CO, H_2O}:

$$c = \frac{\sum_{i \in S} Y_i - \sum_{i \in S} Y_{i,u}}{\sum_{i \in S} Y_{i,b} - \sum_{i \in S} Y_{i,u}} = \frac{\sum_{i \in S} Y_i - \sum_{i \in S} Y_{i,u}}{Y_{c,n}} \tag{6.1}$$

where $Y_{i,u}$ is the i-th species mass fraction in unburnt gases, $Y_{i,b}$ is the i-th species mass fraction in burned gases and $Y_{c,n}$ is the normalizing factor; so the progress variable values can be only included between 0 and 1: in particular, $c = 0$ in unburnt gases and $c = 1$ in burned gases (see figure 6.16).
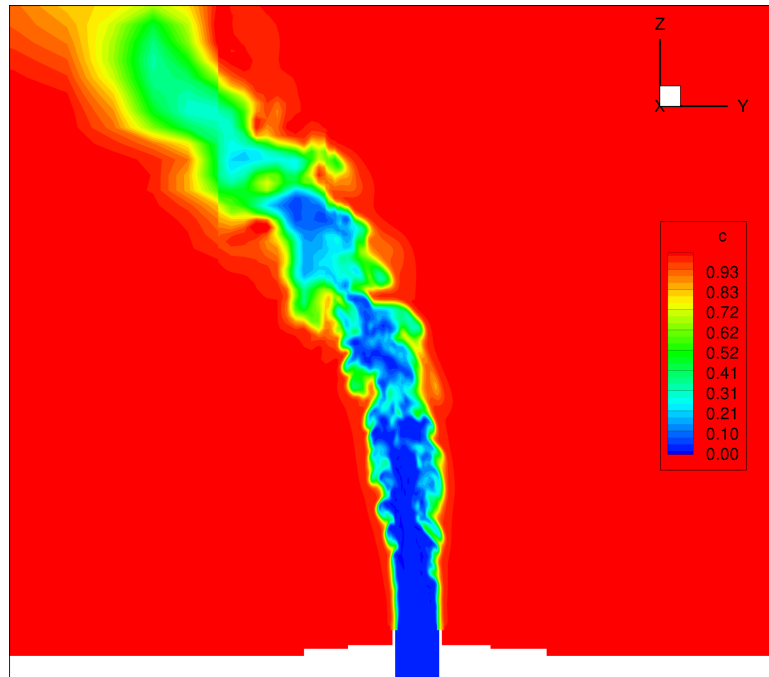
FIGURE 6.16.   Progress Variable Contour for JG2 Numerical Simulation

For the flame described in table 6.1 on page 67, the maximum heat release is for $c = 0.704$, while the maximum value of temperature gradient, adopted for the calculation of laminar flame thermal thickness δ_{th}, is $c = 0.44$; the heat release is complete at $c \sim 0.9$.

The local geometry of the progress variable scalar field is defined by:

- its value $c = (\mathbf{x}, t)$;

- its derivative in the direction normal to the iso-surface;

- its curvature.
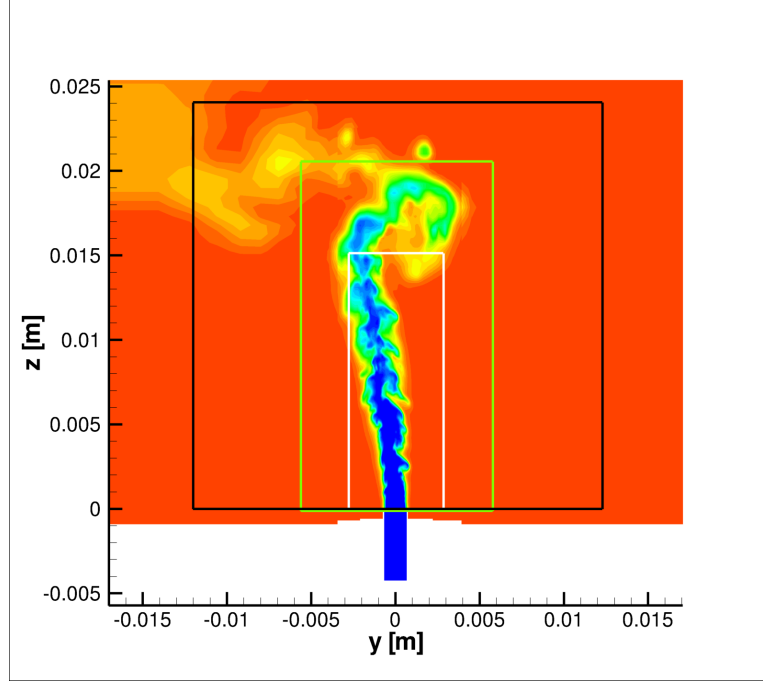
FIGURE 6.17. Areas where the statistics take place: JG3 (white), JG2 (green), DNS (black)

The curvature is computed from the not symmetric tensor formed by taking the gradient of the flame front normal vector $\mathbf{n}_{i,j} = \partial n_i i / \partial x_j$. The principal curvatures k_1, k_2 are the two nonzero eigenvalues of the curvature tensor $\mathbf{n}_{i,j}$. They are related to the two nonzero invariants $I_1 = -\nabla \cdot \mathbf{n} = -(k_1 + k_2) = 2k_m$ (where $k_m = I_1/2$ is the mean curvature) and $I_2 = (n_{i,i}n_{j,j} - n_{i,j}n_{j,i})/2 = k_1 k_2 = k_g$ (where k_g is the Gaussian curvature) by the

$$k_1, k_2 = \frac{\left(-I_1 + \sqrt{I_1^2 - 4I_2}\right)}{2} \tag{6.2}$$

The zone $k_g > k_m^2$ implies complex curvature and it's excluded from the statistics, that are normalized using the laminar flame temperature gradient thickness δ_L.

The statistics take place in the finest reaction zone, where the main part of the flame is located. In figure 6.17, are represented the regions where the statistics take place, for the three simulations analyzed: the biggest rectangle (black) is the volume, in the IJ plane, where the DNS statistics are evaluated, the green rectangle is the region where JG2 statistics are evaluated while the smallest rectangle (white) is the JG3 region: so, for JG3 simulation, the upper part of the flame is excluded from the statistics, because of the poor resolution of the computational grid respect to JG2 and DNS simulations.

In figure 6.18 the PDF of the normalized curvature at different progress variable values is represented (JG2 - lines, JG3 - lines with symbols): in the reaction zone, at higher value of the progress variable c, the probability of finding negative (concave towards the reactants) curvature ($\nabla \cdot \mathbf{n}\delta_L \sim -0.6$) is higher than in the
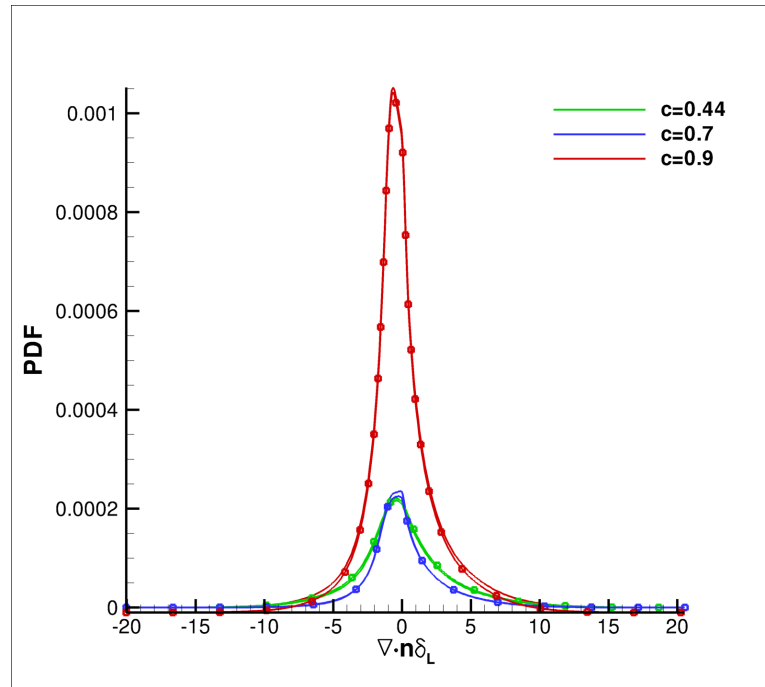
Figure 6.18.   Curvature's PDFs for JG2 (lines) and JG3 (lines with symbols)

diffusive layer ($\nabla \cdot \mathbf{n}\delta_L \sim 0$); the smallest mean radius of curvature is about $\delta_L \sim 10$ since the flame has a finite thickness.

An asymmetry in the flame curvature PDFs is noticeable in the reaction zone, where it's more probable to find negative curves than positive ones. The two joined grid simulations show very good agreement.

In figure 6.19 are plotted PDF's curvatures for JG2, JG3 and DNS for $c = 0.44$, $c = 0.7$ and $c = 0.9$; also if there's a big difference in terms of spatial resolution (for DNS, minimum grid spacing is $9\,\mu m$, for JG2 and JG3 is $35\,\mu m$), the shape of the curves and the peak position are very close: the closure model adopted for LES simulations is very good.

(A) c = 0.44   (B) c = 0.7   (C) c = 0.9
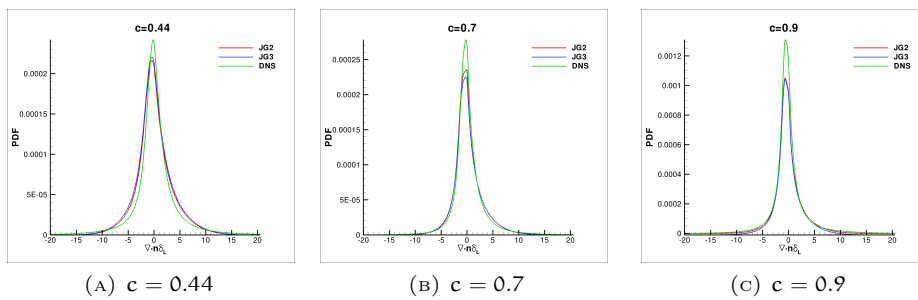
Figure 6.19.   JG2, JG3 and DNS Curvature PDFs comparison for $c = 0.44$, $c = 0.7$ and $c = 0.9$

84
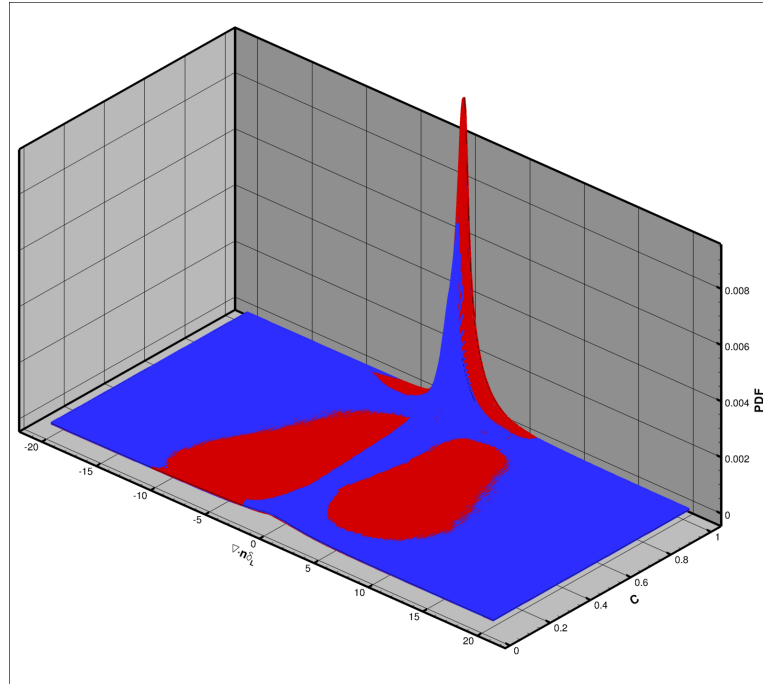
FIGURE 6.20. JG2 (red) and DNS (blue) Curvature PDFs comparison for any c value

In all the three figures, for curvature values very close to 0, the PDF's curvature of the DNS (green curve) is always slightly over the PDF's curvatures of JG2 and JG3 simulations.

In figure 6.20 are plotted the curvature PDFs for any c value for both JG2 and DNS numerical simulations: is possible to notice that JG2 PDFs for outer curvature values is bigger than the DNS PDFs, at any c; the DNS, otherwise, shows higher PDFs for the smaller curvatures, at almost any c value.

The local geometry of a three dimensional iso-surface can be qualitatively characterized by the curvature shape factor $H_k = k_{min}/k_{max}$, where k_{min} and k_{max} are respectively the smaller and the larger values between k_1 and k_2: so, following this definition, the shape factor can only vary between -1 and 1. If $H_k \sim -1$, the mean curvature is zero and the flame surface is near a perfect spherical saddle; if $H_k \sim 0$, one principal curvature is much larger in magnitude than the numerator, so the flame surface is flat in one direction (i.e. it's locally cylindrical); when $H_k \sim +1$, the flame surface is spherically curved.

The normalized PDFs of H_k at different iso-c surfaces are shown in figure 6.21 on the following page (JG2 - lines, JG3 - lines with symbols): the most probable values for the shape factor are close to zero, indicating that the flame has mainly a cylindrical shape; the distribution of the shape factor is skewed negatively, indicating that saddle-like curvatures are more probable than ellipsoidal regions: for $H_k \sim 1$, the PDF value, for all the three curves, is near zero.

The comparison between JG2, JG3 and DNS is showed in figure 6.22 on the next page, where are plotted shape factor PDFs for c = 0.44, c = 0.7 and c = 0.9: the shape of the curves is very similar, and also for the DNS the higher PDF value
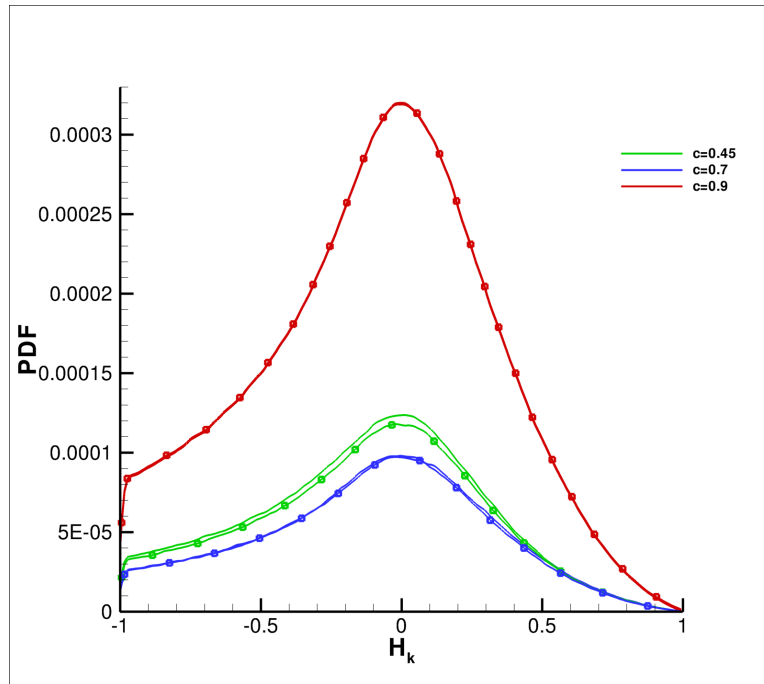
FIGURE 6.21.   Shape factor PDFs for JG2 (lines) and JG3 (lines with symbols)

(A) $c = 0.44$ (B) $c = 0.7$ (C) $c = 0.9$
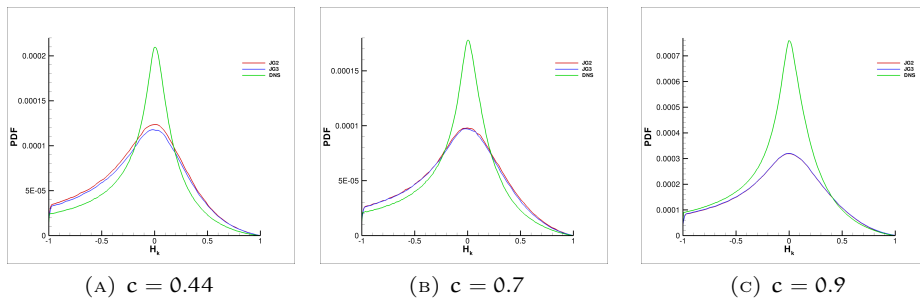
FIGURE 6.22.   JG2, JG3 and DNS Shape Factor PDFs comparison for $c = 0.44$, $c = 0.7$ and $c = 0.9$
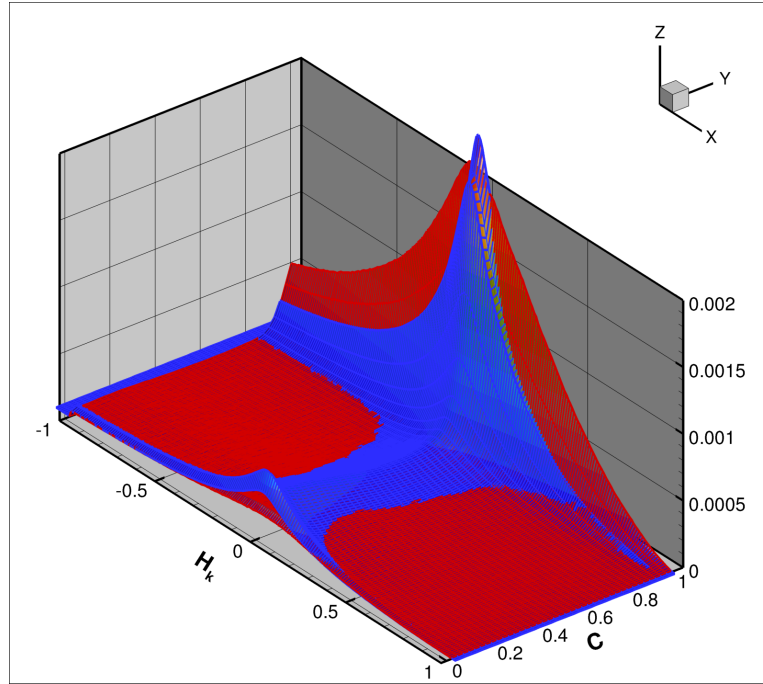
FIGURE 6.23.   JG2 (red) and DNS (blue) Shape Factor PDFs comparison for any c value

is reached when $H_k = 0$, but also in this case the DNS PDF is higher than JG2 and JG3 PDF for H_k values close to 0.

In figure 6.20 on page 85 are plotted the shape factor PDFs for any c value for both JG2 and DNS numerical simulations: DNS PDFs for H_k values near 0 are higher than JG2 PDFs for any c value, so for the DNS the c isosurfaces have an higher probability to acquire a cylindrical shape than the JG2 c iso-surfaces; for JG2 is otherwise more probable to find a spherical saddle or a perfect sphere in the c iso-surfaces than the DNS.

The inverse of the magnitude of the gradient of the progress variable is directly associated to the flame thickness: the figure 6.24 shows the conditional mean of normalized $|\nabla c|$, with the laminar flame thickness δ_L used as normalizing factor.
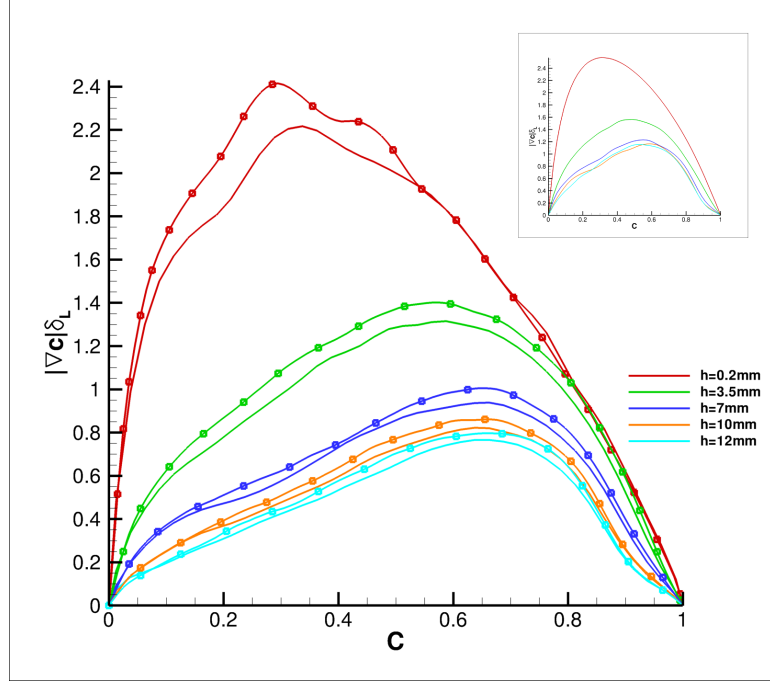
FIGURE 6.24. Conditional means of the normalized flame thickness $|\nabla c|\delta_L$ versus the progress variable, at different heights (JG2 lines, JG3 lines with symbols); in the square curvature's PDF obtained from the DNS [Cecere et al., 2015]

The results show that the flame thickness is lower than the laminar flame thickness δ_L close to the exit of the mixture channel (h = 0.2 mm) and for c ~ 0.3: this is due to the development of the shear layer and to the local increase of the strain rate that reduces the thickness of the flame; the shape of the curve, moreover, is skewed towards the reactant side.

As the shear layer develops downstream, velocity gradients in crosswise direction decrease and the flame thickness increases. Also in this case, the shape and the amplitude of the curves is similar to that obtained from the previously cited DNS (figure 6.24, on the upper right corner); also in this case the two joined grid simulations show a good agreement.

6.3.3 Turbulence Spectra Analysis

In this section, the fluctuating kinetic energy spectra analysis for JG2 and DNS numerical simulation are reported. The sampling point, for both cases, is located 4 mm over the right wall of the inlet duct (figure 6.25).

From the samples of the streamwise (w) and spanwise (v) velocities, the streamwise and spanwise mean values are obtained from:

$$\overline{w} = \frac{\sum_{i=1}^{N} w_i}{N}, \quad \overline{v} = \frac{\sum_{i=1}^{N} v_i}{N} \tag{6.3}$$

where N is the total number of the samples.
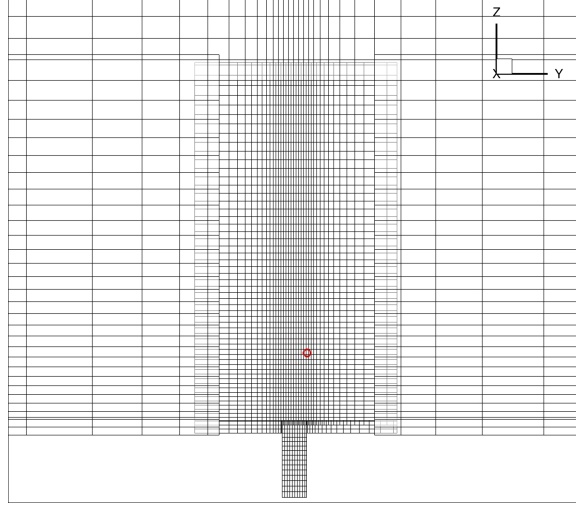
Figure 6.25. Sampling point (red circle) position

These mean values are used to extract the fluctuating component for the stream-wise and the spanwise velocities, as

$$w'_i = w_i - \overline{w}, \quad v'_i = v_i - \overline{v} \tag{6.4}$$

The fluctuating kinetic energy is then calculated as

$$E'_i = \frac{w'^2_i + v'^2_i}{2} \tag{6.5}$$

The crosswise velocity component (u) is excluded from the 6.5 because it is negligible with respect to the other two components but above all because it has not converged statistics.

For DNS, the sampling frequency is $1\,\mathrm{MHz}$, the sampling time is $\sim 1.8\,\mathrm{ms}$ and so the resolution frequency is $\sim 550\,\mathrm{Hz}$.

In figure 6.26 on the following page, the complete (on the left) and the selected two-burst ($\sim 0.508\,\mathrm{ms}$, on the right) samplings are reported, while the spectra of these two signals are represented in figure 6.27.

The two-burst spectrum shows an inertial decay with a slope very close to $-5/3$ for frequencies above $75\,\mathrm{kHz}$.

The complete signal spectrum, instead, shows an inertial decay with a slope close to $-5/3$ only for high frequencies (above $\sim 126\,\mathrm{kHz}$), while for the rest of the spectrum the slope is close to $-2/3$: this behaviour will be investigated in future DNS simulations.

Summarizing, the DNS spectral analysis shows a $-5/3$ slope for frequencies larger than $75\,\mathrm{kHz}$: for smaller frequencies, the slope is very close to $-2/3$, but the poor frequency resolution doesn't permit to examine this phenomenon in a adequate manner.

In figure 6.28, the complete (on the left) and the first two-burst ($\sim 1.308\,\mathrm{ms}$, on the right) samplings obtained from the JG2 simulation are reported: the sam-

(A) Complete sampling

(B) Two-bursts sampling
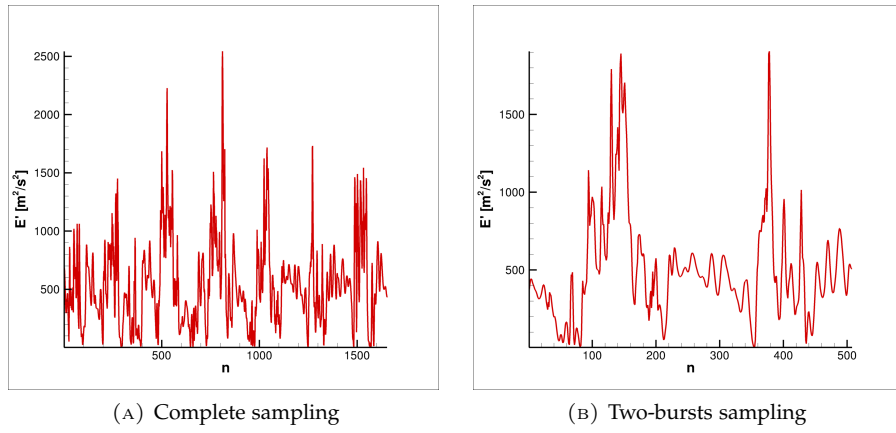
Figure 6.26.   Fluctuating kinetic energy samplings for DNS
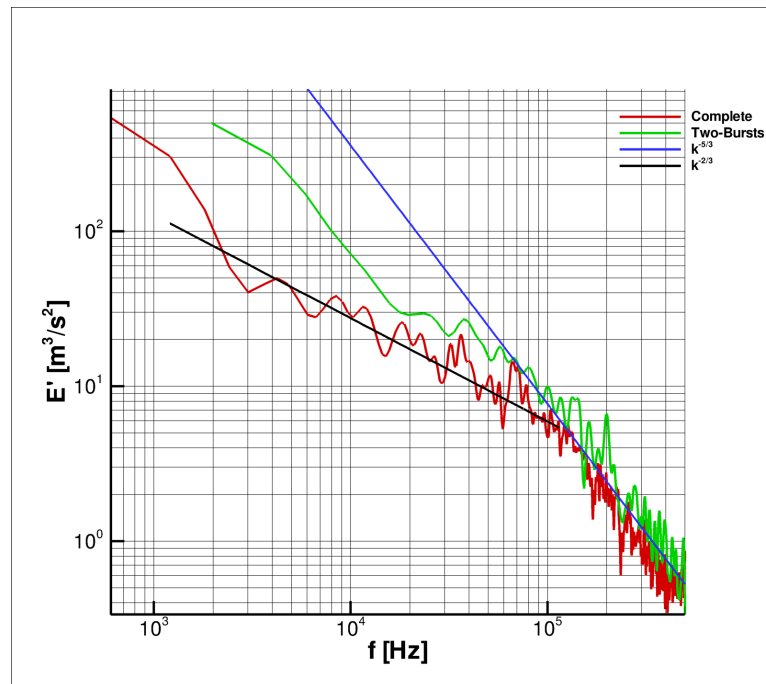
Figure 6.27.   Fluctuating kinetic energy spectra for the complete and the two-burst samplings obtained from DNS

(A) Complete sampling   (B) Two-burst sampling
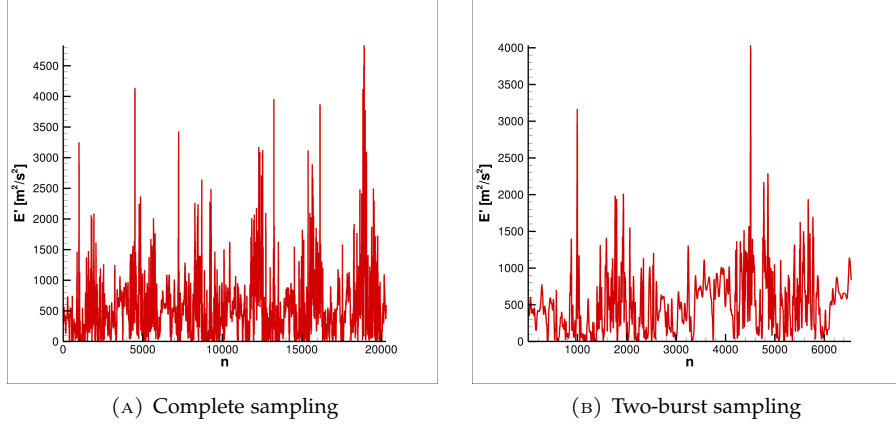
FIGURE 6.28.   Fluctuating kinetic energy samplings for JG2

pling frequency is 5 MHz, the sampling time is ∼ 4.396 ms and so the resolution frequency is ∼ 230 Hz.

The spectra of these two signals are represented in figure 6.29: the complete signal shows an inertial decay with a slope close to −2/3 until ∼ 300 kHz, that is the cut-off frequency where the subgrid scale model starts to work; at that point, under the ergodic hypothesis, it is possible to find a relationship between the characteristic length of the cell and the frequency: the characteristic length of the cell is $\Delta = \sqrt[3]{V} = 5.0 \times 10^{-5}$ m, where V is the cell volume, and therefore $1/\Delta = 3.0 \times 10^5$.

The two-burst spectrum shows an inertial decay with a slope close to −2/3 until ∼ 150 kHz, beyond which the Kolmogorov theory −5/3 slope appears: also in this case, for frequencies larger than ∼ 300 kHz the spectrum separates from the predicted Kolmogorov theory slope.

The absence of −5/3 slope in the complete energy spectrum can be attributed to the subgrid scale model error: as can be seen in [Lesieur, 2008], the scale of the wave number over which most of the error is confined $(k_e(t))$ follows an analogous Richardson law, which leads to

$$k_e^{-2/3}(t) \sim \epsilon^{1/3}t + k_e^{-2/3}(t_0) \qquad (6.6)$$

where t_0 is the time at which the error has been injected in the small scales of the inertial range. This shows that k_e is going to decrease following a $(t-t_0)^{-3/2}$ law, as soon as $k_e(t)$ will be sufficiently small compared with $k_e(0)$. So the initial location of this wave number can be forgotten, and the necessary time for the error, starting from very high wave numbers, to reach a given wave number k, is proportional to $\epsilon^{-1/3}k^{-2/3}$, that is the local turnover time of turbulence at k.

The complete signal was sampled for more than 4 ms, so the error had the time to go back up the energy spectrum and "replaces" the −5/3 Kolmogorov slope with the −2/3 slope obtained from equation 6.6.

As can be seen from the DNS spectra, the −2/3 slope can be attributed to the subgrid scale model error only for the wave numbers between 150 kHz and 300 kHz: the −2/3 slope before 150 kHz in the JG2 simulation, as well as the
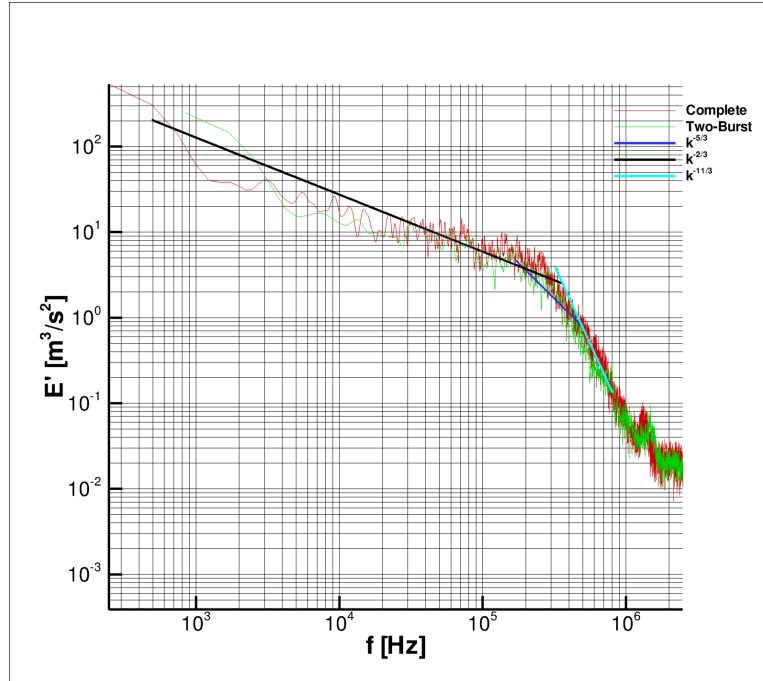
Figure 6.29. Fluctuating kinetic energy spectra for the complete and the two-burst samplings obtained from JG2

−2/3 slope observed in figure 6.27, will be investigated in future LES and DNS simulations.

In figure 6.30 on the next page, the complete and two-burst spectra for JG2 and DNS are compared. For the two-burst spectra, DNS and JG2 are not in agreement: the first, indeed, shows a −5/3 slope for almost the whole spectrum, excluding a very little zone where the DNS spectrum has the same −2/3 slope of the JG2 spectrum. The complete spectra show a better agreement until ∼ 150 kHz, where the DNS begins to show a slope very close to the −5/3 Kolmogorov's theory one, while the LES spectrum slope is still −2/3 up to 300 kHz, beyond which the slope changes to −11/3.

(A) Two-burst spectra
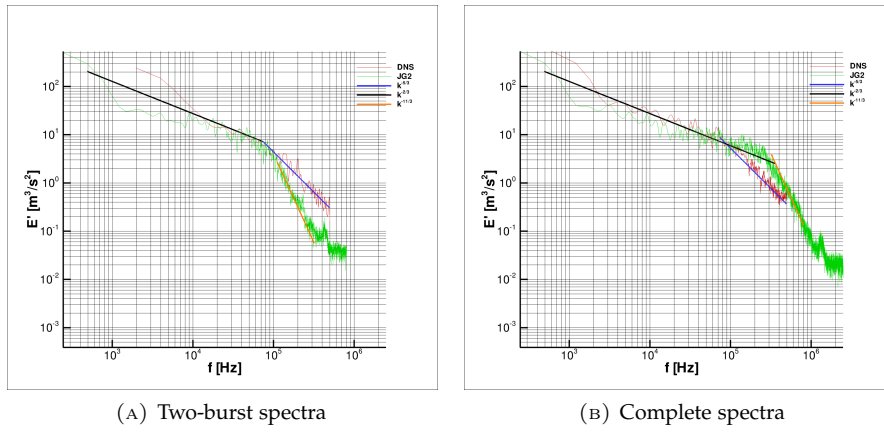
(B) Complete spectra

FIGURE 6.30.   Comparison between DNS and LES 2 bursts and complete spectra

7

Concluding Remarks

The LES approach is growing in importance since, when a sufficient portion of the energy spectrum is resolved, it is the only available and reliable tool with prediction capability for complex flows.

Unfortunately, when this technique is used on a big domain discretized by means of a structured grid, a difficult compromise could be engaged: if the domain geometric characteristics or the fluid motion peculiarities need an high spatial resolution, the numerical grid will be made by an incredible number of nodes, making the solution obtainable only on hundred of thousands computational cores; vice versa, if such computing power is not available, the chosen number of computational nodes don't allow to produce an accurate numerical solution of the flow field.

This problem can be resolved with a multi-resolution technique that permit to improve the spatial resolution only where it's necessary: in such way it's possible to reduce the total number of computational nodes and/or, at the same time, to obtain a better numerical solution.

The development of a multi-resolution technique for an existing numerical code is a challenging task. Indeed, a deep and accurate knowledge of the existing code is necessary, from both numerical and information technology points of view: the first has a fundamental role in the selection of a multi-resolution algorithm (i.e. the staggered grid adopted in the HeaRT numerical code requires a different treatment for scalars and momentum), while the latter is very important to understand existing data structures, modules and subroutines already available and to understand the whole operation algorithm.

By mean of this technique, based on the joined-grid approach, is possible to obtain some important targets.

First, is possible to reduce, in a considerable way, the total number of grid points without any significant loss of accuracy: the 3 levels computational grid used in the numerical simulation of the slot flame has about one third, in terms of computing nodes, respect to the single level grid; this permits to obtain smaller output files (the size is reduced from $\sim 800\,\mathrm{MB}$ to $\sim 270\,\mathrm{MB}$) and therefore an important saving of disk space, post-processing times and computational resources.

The computational nodes number reduction has furthermore a positive effect on single iteration (or time step) computing times: for a small number of cores

(up to 16), the joined-grids numerical simulations shows a shorter computing time respect to the single level simulation; for an higher number of cores, the advantage of joined-grids algorithm is not so clear. One the reasons is the domain decomposition algorithm adopted in the HeaRT code, that makes impossible a concentration of CPUs on the finest zone, because it is limited on a "structured" decomposition of the numerical grid; another reason is most assuredly the poor efficiency of the joined-grids procedures, that have to be deep analyzed to discover all the possible bottlenecks, cache misses and every other problem in memory management.

The validation of the whole multi-resolution algorithm has permitted to analyze in detail the topological structure of the CH_4/H_2-Air slot flame: the central pre-heated jet, because of its high velocity, trails and warps the hot coflow; in few millimeters, the central jet speed decrease of about $30\,m\,s^{-1}$, since a section of its kinetic energy is been transferred to the coflow, that sees its velocity increased from $\sim 20\,m\,s^{-1}$ to $\sim 35\,m\,s^{-1}$.

The flame curvature statistics analysis strengthen the three dimensional behaviour of the flow field with particular attention to the flame front curvature and shape-factor: the flame has mainly a cylindrical shape and in the reaction zone, because of the presence of the hydrogen, the curvature has an high probability to be concave towards the reactants. The flame thickness, moreover, is lower than the laminar flame thickness close to the exit of the mixture channel, because of the development of the shear layer and to the local increase of the strain rate: as the shear layer develops downstream, the flame thickness increase.

The spectral analysis shows an unexpected behaviour, with an inexplicable slope of about $-2/3$ both for DNS and for LES simulations; another interesting aspect is the difference between the complete spectra and the two-bursts spectra, that is partially explained with the Lesieur error formulation. These two anomalies will be the subject of future DNS and LES numerical simulations of channel flows.

In conclusion, even if this work can be considered as a first step to obtain a multi-resolution algorithm on a compressible and staggered LES numerical code, the presented approach has demonstrated a great potential providing good numerical results and a important drop in the numerical results data amount.

PART III

APPENDIXES

A

CYLINDRICAL COORDINATES SYSTEM

T HE common large energy burner combustion chamber's shape is cylindrical-like, at least for the main part, therefore adopting a cylindrical coordinates system is very useful for a better discretization of the domain. The cylindrical coordinates system adopted, cylindrical/rectangular transformation equations and the governing equations in cylindrical coordinates are reported in this chapter.

A.1 CURVILINEAR ORTHOGONAL COORDINATES SYSTEM

Cylindrical coordinates system belongs to the curvilinear orthogonal system. Respect to the rectangular coordinates system, that is also an orthogonal system, a curvilinear orthogonal system has a tensor metric that is generally different to the unit tensor. In this section the tensor metric for a curvilinear orthogonal coordinates system is evaluated; also the transformation equations for the operators $\nabla^2\,()$, $\overrightarrow{\nabla} \cdot ()$, $\overrightarrow{\nabla} \times ()$ and $\overrightarrow{\nabla}\,()$ are presented.

Considering the rectangular coordinates system (x, y, z) with the basis unit vectors $\overrightarrow{i}$, $\overrightarrow{j}$, $\overrightarrow{k}$ the position vector $\overrightarrow{p}$ can be expressed as:

$$\overrightarrow{p} = x \cdot \overrightarrow{i} + y \cdot \overrightarrow{j} + z \cdot \overrightarrow{k} \tag{A.1}$$

Introducing a new curvilinear orthogonal coordinates system (ξ_1, ξ_2, ξ_3) with the basis unit vectors $\overrightarrow{e}_1$, $\overrightarrow{e}_2$, $\overrightarrow{e}_3$ the position vector $\overrightarrow{p}$ can be expressed as:

$$\overrightarrow{p} = \xi_1 \cdot \overrightarrow{e}_1 + \xi_2 \cdot \overrightarrow{e}_2 + \xi_3 \cdot \overrightarrow{e}_3 \tag{A.2}$$

The derivatives of $\overrightarrow{p}$ with respect to (ξ_1, ξ_2, ξ_3) are the base vectors of the curvilinear system:

$$
\begin{aligned}
h_1 &= \left| \frac{\partial \overrightarrow{p}}{\partial \xi_1} \right| = \left| \begin{array}{ccc} \frac{\partial x}{\partial \xi_1} & \frac{\partial y}{\partial \xi_1} & \frac{\partial z}{\partial \xi_1} \end{array} \right| = \sqrt{\left(\frac{\partial x}{\partial \xi_1}\right)^2 + \left(\frac{\partial y}{\partial \xi_1}\right)^2 + \left(\frac{\partial z}{\partial \xi_1}\right)^2} \\
h_2 &= \left| \frac{\partial \overrightarrow{p}}{\partial \xi_2} \right| = \left| \begin{array}{ccc} \frac{\partial x}{\partial \xi_2} & \frac{\partial y}{\partial \xi_2} & \frac{\partial z}{\partial \xi_2} \end{array} \right| = \sqrt{\left(\frac{\partial x}{\partial \xi_2}\right)^2 + \left(\frac{\partial y}{\partial \xi_2}\right)^2 + \left(\frac{\partial z}{\partial \xi_2}\right)^2} \\
h_3 &= \left| \frac{\partial \overrightarrow{p}}{\partial \xi_3} \right| = \left| \begin{array}{ccc} \frac{\partial x}{\partial \xi_3} & \frac{\partial y}{\partial \xi_3} & \frac{\partial z}{\partial \xi_3} \end{array} \right| = \sqrt{\left(\frac{\partial x}{\partial \xi_3}\right)^2 + \left(\frac{\partial y}{\partial \xi_3}\right)^2 + \left(\frac{\partial z}{\partial \xi_3}\right)^2}
\end{aligned}
\tag{A.3}
$$

Therefore the tensor metric is:

$$T_{Metric} = \begin{bmatrix} h_1 & 0 & 0 \\ 0 & h_2 & 0 \\ 0 & 0 & h_3 \end{bmatrix}$$

(A.4)

Thus the curvilinear basis unit vectors can be expressed as:

$$\vec{e_1} = \frac{1}{h_1}\frac{\partial \vec{p}}{\partial \xi_1} \quad \vec{e_2} = \frac{1}{h_2}\frac{\partial \vec{p}}{\partial \xi_2} \quad \vec{e_3} = \frac{1}{h_3}\frac{\partial \vec{p}}{\partial \xi_3}$$

(A.5)

The operators $\vec{\nabla} \cdot ()$ and $\vec{\nabla} ()$ can be expressed as:

$$\vec{\nabla} \cdot () = \frac{\partial ()}{\partial x} \cdot \vec{i} + \frac{\partial ()}{\partial y} \cdot \vec{j} + \frac{\partial ()}{\partial z} \cdot \vec{k} = \frac{1}{h_1}\frac{\partial ()}{\partial \xi_1} \cdot \vec{e_1} + \frac{1}{h_2}\frac{\partial ()}{\partial \xi_2} \cdot \vec{e_2} + \frac{1}{h_3}\frac{\partial ()}{\partial \xi_3} \cdot \vec{e_3}$$

(A.6)

$$\vec{\nabla} () = \frac{\partial ()}{\partial x}\vec{i} + \frac{\partial ()}{\partial y}\vec{j} + \frac{\partial ()}{\partial z}\vec{k} = \frac{1}{h_1}\frac{\partial ()}{\partial \xi_1}\vec{e_1} + \frac{1}{h_2}\frac{\partial ()}{\partial \xi_2}\vec{e_2} + \frac{1}{h_3}\frac{\partial ()}{\partial \xi_3}\vec{e_3}$$

(A.7)

Note that if we apply one of A.6 and A.7 to a vector expressed in the curvilinear system we must evaluate the derivatives of $\vec{e}_1, \vec{e}_2, \vec{e}_3$ with respect of (ξ_1, ξ_2, ξ_3); since the curvilinear coordinates system considered is orthogonal the following identities are satisfied:

$$\begin{array}{ccc} \vec{e_1} \cdot \vec{e_2} = 0 & \vec{e_2} \cdot \vec{e_3} = 0 & \vec{e_1} \cdot \vec{e_3} = 0 \\ \frac{\partial \vec{p}}{\partial \xi_1} \cdot \frac{\partial \vec{p}}{\partial \xi_2} = 0 & \frac{\partial \vec{p}}{\partial \xi_2} \cdot \frac{\partial \vec{p}}{\partial \xi_3} = 0 & \frac{\partial \vec{p}}{\partial \xi_1} \cdot \frac{\partial \vec{p}}{\partial \xi_3} = 0 \\ \vec{e_1} = \vec{e_2} \times \vec{e_3} & \vec{e_2} = \vec{e_3} \times \vec{e_1} & \vec{e_3} = \vec{e_1} \times \vec{e_2} \end{array}$$

(A.8)

Differencing the second line of identities of A.8 by that coordinate which does not appear explicitly we obtain:

$$\begin{array}{c} \frac{\partial \vec{p}}{\partial \xi_1} \cdot \frac{\partial^2 \vec{p}}{\partial \xi_2 \partial \xi_3} + \frac{\partial^2 \vec{p}}{\partial \xi_1 \partial \xi_3} \cdot \frac{\partial \vec{p}}{\partial \xi_2} = 0 \\ \frac{\partial \vec{p}}{\partial \xi_2} \cdot \frac{\partial^2 \vec{p}}{\partial \xi_1 \partial \xi_3} + \frac{\partial^2 \vec{p}}{\partial \xi_1 \partial \xi_2} \cdot \frac{\partial \vec{p}}{\partial \xi_3} = 0 \\ \frac{\partial \vec{p}}{\partial \xi_1} \cdot \frac{\partial^2 \vec{p}}{\partial \xi_2 \partial \xi_3} + \frac{\partial^2 \vec{p}}{\partial \xi_1 \partial \xi_2} \cdot \frac{\partial \vec{p}}{\partial \xi_3} = 0 \end{array}$$

(A.9)

adding the first two of A.9 we obtain:

$$\frac{\partial \vec{p}}{\partial \xi_1} \cdot \frac{\partial^2 \vec{p}}{\partial \xi_2 \partial \xi_3} + \frac{\partial^2 \vec{p}}{\partial \xi_1 \partial \xi_3} \cdot \frac{\partial \vec{p}}{\partial \xi_2} + \frac{\partial \vec{p}}{\partial \xi_2} \cdot \frac{\partial^2 \vec{p}}{\partial \xi_1 \partial \xi_3} + \frac{\partial^2 \vec{p}}{\partial \xi_1 \partial \xi_2} \cdot \frac{\partial \vec{p}}{\partial \xi_3} = 0$$

$$\Downarrow$$

$$2\frac{\partial \vec{p}}{\partial \xi_2} \cdot \frac{\partial^2 \vec{p}}{\partial \xi_1 \partial \xi_3} + \underbrace{\frac{\partial \vec{p}}{\partial \xi_1} \cdot \frac{\partial^2 \vec{p}}{\partial \xi_2 \partial \xi_3} + \frac{\partial^2 \vec{p}}{\partial \xi_1 \partial \xi_2} \cdot \frac{\partial \vec{p}}{\partial \xi_3}}_{=0 \quad by\ means\ of\ third\ identities} = 0$$

$$\Downarrow$$

$$\frac{\partial \vec{p}}{\partial \xi_2} \cdot \frac{\partial^2 \vec{p}}{\partial \xi_1 \partial \xi_3} = 0$$

With analogous calculations we obtain:

$$\frac{\partial \vec{p}}{\partial \xi_1} \cdot \frac{\partial^2 \vec{p}}{\partial \xi_2 \partial \xi_3} = 0 \quad \frac{\partial \vec{p}}{\partial \xi_2} \cdot \frac{\partial^2 \vec{p}}{\partial \xi_1 \partial \xi_3} = 0 \quad \frac{\partial \vec{p}}{\partial \xi_3} \cdot \frac{\partial^2 \vec{p}}{\partial \xi_1 \partial \xi_2} = 0$$

(A.10)

The partial derivatives of $\vec{p}$ with respect to (ξ_1, ξ_2, ξ_3) are tangential to the coordinate lines ξ_1, ξ_2 and ξ_3, respectively, and so from the first of A.10 we obtain:

$$\frac{\partial^2 \vec{p}}{\partial \xi_2 \partial \xi_3} \perp \vec{e_1} \Rightarrow \frac{\partial^2 \vec{p}}{\partial \xi_2 \partial \xi_3} = \alpha \cdot \vec{e_2} + \beta \cdot \vec{e_3}$$

Using the third of A.5 and the above equation we obtain:

$$\frac{\partial^2 \vec{p}}{\partial \xi_2 \partial \xi_3} = \frac{\partial}{\partial \xi_2}\left(\frac{\partial \vec{p}}{\partial \xi_3}\right) = \frac{\partial}{\partial \xi_2}\left(h_3 \vec{e_3}\right) = h_3 \frac{\partial \vec{e_3}}{\partial \xi_2} + \frac{\partial h_3}{\partial \xi_2} \vec{e_3} = \alpha \cdot \vec{e_2} + \beta \cdot \vec{e_3}$$

because $\frac{\partial \vec{e_3}}{\partial \xi_2} \parallel \vec{e_2}$ we obtain:

$$\beta = \frac{\partial h_3}{\partial \xi_2}$$

With analogous passages we finally obtain:

$$\begin{array}{lll}
\frac{\partial \vec{e_1}}{\partial \xi_1} = -\frac{\partial h_1}{\partial \xi_2}\frac{\vec{e_2}}{h_2} - \frac{\partial h_1}{\partial \xi_3}\frac{\vec{e_3}}{h_3} & \frac{\partial \vec{e_1}}{\partial \xi_2} = \frac{\partial h_2}{\partial \xi_1}\frac{\vec{e_2}}{h_1} & \frac{\partial \vec{e_1}}{\partial \xi_3} = \frac{\partial h_3}{\partial \xi_1}\frac{\vec{e_3}}{h_1} \\
\frac{\partial \vec{e_2}}{\partial \xi_1} = \frac{\partial h_1}{\partial \xi_2}\frac{\vec{e_1}}{h_2} & \frac{\partial \vec{e_2}}{\partial \xi_2} = -\frac{\partial h_2}{\partial \xi_3}\frac{\vec{e_3}}{h_3} - \frac{\partial h_2}{\partial \xi_1}\frac{\vec{e_2}}{h_2} & \frac{\partial \vec{e_2}}{\partial \xi_3} = \frac{\partial h_3}{\partial \xi_2}\frac{\vec{e_3}}{h_2} \\
\frac{\partial \vec{e_3}}{\partial \xi_1} = \frac{\partial h_1}{\partial \xi_3}\frac{\vec{e_1}}{h_3} & \frac{\partial \vec{e_3}}{\partial \xi_2} = \frac{\partial h_2}{\partial \xi_3}\frac{\vec{e_2}}{h_3} & \frac{\partial \vec{e_3}}{\partial \xi_3} = -\frac{\partial h_3}{\partial \xi_1}\frac{\vec{e_1}}{h_1} - \frac{\partial h_3}{\partial \xi_2}\frac{\vec{e_2}}{h_2}
\end{array}$$
$$(A.11)$$

By means of A.11 we can obtain the operators $\vec{\nabla} \cdot ()$ into the curvilinear coordinates system; considering a generic vector $\vec{u} = u_1 \vec{e_1} + u_2 \vec{e_2} + u_3 \vec{e_3}$ the divergence operator can be expressed as:

$$\vec{\nabla} \cdot \vec{u} = \frac{\partial \vec{u}}{\partial \xi_1} \cdot \frac{\vec{e_1}}{h_1} + \frac{\partial \vec{u}}{\partial \xi_2} \cdot \frac{\vec{e_2}}{h_2} + \frac{\partial \vec{u}}{\partial \xi_3} \cdot \frac{\vec{e_3}}{h_3} =$$

$$= \frac{\partial\left(u_1 \vec{e_1} + u_2 \vec{e_2} + u_3 \vec{e_3}\right)}{\partial \xi_1} \cdot \frac{\vec{e_1}}{h_1} + \frac{\partial\left(u_1 \vec{e_1} + u_2 \vec{e_2} + u_3 \vec{e_3}\right)}{\partial \xi_2} \cdot \frac{\vec{e_2}}{h_2} + \frac{\partial\left(u_1 \vec{e_1} + u_2 \vec{e_2} + u_3 \vec{e_3}\right)}{\partial \xi_3} \cdot \frac{\vec{e_3}}{h_3} =$$

$$= \left[\frac{\partial u_1}{\partial \xi_1} \underbrace{\vec{e_1} \cdot \vec{e_1}}_{1} + u_1 \underbrace{\frac{\partial \vec{e_1}}{\partial \xi_1} \cdot \vec{e_1}}_{0} + \frac{\partial u_2}{\partial \xi_1} \underbrace{\vec{e_2} \cdot \vec{e_1}}_{0} + u_2 \frac{\partial \vec{e_2}}{\partial \xi_1} \cdot \vec{e_1} + \frac{\partial u_3}{\partial \xi_1} \underbrace{\vec{e_3} \cdot \vec{e_1}}_{0} + u_3 \frac{\partial \vec{e_3}}{\partial \xi_1} \cdot \vec{e_1}\right] \frac{1}{h_1} +$$

$$+ \left[\frac{\partial u_1}{\partial \xi_2} \underbrace{\vec{e_1} \cdot \vec{e_2}}_{0} + u_1 \frac{\partial \vec{e_1}}{\partial \xi_2} \cdot \vec{e_2} + \frac{\partial u_2}{\partial \xi_2} \underbrace{\vec{e_2} \cdot \vec{e_2}}_{1} + u_2 \underbrace{\frac{\partial \vec{e_2}}{\partial \xi_2} \cdot \vec{e_2}}_{0} + \frac{\partial u_3}{\partial \xi_2} \underbrace{\vec{e_3} \cdot \vec{e_2}}_{0} + u_3 \frac{\partial \vec{e_3}}{\partial \xi_2} \cdot \vec{e_2}\right] \frac{1}{h_2} +$$

$$+ \left[\frac{\partial u_1}{\partial \xi_3} \underbrace{\vec{e_1} \cdot \vec{e_3}}_{0} + u_1 \frac{\partial \vec{e_1}}{\partial \xi_3} \cdot \vec{e_3} + \frac{\partial u_2}{\partial \xi_3} \underbrace{\vec{e_2} \cdot \vec{e_3}}_{0} + u_2 \frac{\partial \vec{e_2}}{\partial \xi_3} \cdot \vec{e_3} + \frac{\partial u_3}{\partial \xi_3} \underbrace{\vec{e_3} \cdot \vec{e_3}}_{1} + u_3 \underbrace{\frac{\partial \vec{e_3}}{\partial \xi_3} \cdot \vec{e_3}}_{0}\right] \frac{1}{h_3} =$$

$$= \frac{1}{h_1 h_2 h_3}\left[h_2 h_3 \frac{\partial u_1}{\partial \xi_1} + h_2 h_3 u_2 \frac{\partial \vec{e_2}}{\partial \xi_1} \cdot \vec{e_1} + h_2 h_3 u_3 \frac{\partial \vec{e_3}}{\partial \xi_1} \cdot \vec{e_1} + \right.$$
$$+ h_1 h_3 u_1 \frac{\partial \vec{e_1}}{\partial \xi_2} \cdot \vec{e_2} + h_1 h_3 \frac{\partial u_2}{\partial \xi_2} + h_1 h_3 u_3 \frac{\partial \vec{e_3}}{\partial \xi_2} \cdot \vec{e_2} +$$
$$\left. + h_1 h_2 u_1 \frac{\partial \vec{e_1}}{\partial \xi_3} \cdot \vec{e_3} + h_1 h_2 u_2 \frac{\partial \vec{e_2}}{\partial \xi_3} \cdot \vec{e_3} + h_1 h_2 \frac{\partial u_3}{\partial \xi_3}\right]$$

Using the [A.11](#) we obtain:

$$\vec{\nabla} \cdot \vec{u} = \frac{1}{h_1 h_2 h_3} \left[h_2 h_3 \frac{\partial u_1}{\partial \xi_1} + h_2 h_3 u_2 \frac{\partial h_1}{\partial \xi_2} \frac{1}{h_2} \underbrace{\vec{e_1} \cdot \vec{e_1}}_{1} + h_2 h_3 u_3 \frac{\partial h_1}{\partial \xi_3} \frac{1}{h_3} \underbrace{\vec{e_1} \cdot \vec{e_1}}_{1} + \right.$$

$$+ h_1 h_3 u_1 \frac{\partial h_2}{\partial \xi_1} \frac{1}{h_1} \underbrace{\vec{e_2} \cdot \vec{e_2}}_{1} + h_1 h_3 \frac{\partial u_2}{\partial \xi_2} + h_1 h_3 u_3 \frac{\partial h_2}{\partial \xi_3} \frac{1}{h_3} \underbrace{\vec{e_2} \cdot \vec{e_2}}_{1} +$$

$$\left. + h_1 h_2 u_1 \frac{\partial h_3}{\partial \xi_1} \frac{1}{h_1} \underbrace{\vec{e_3} \cdot \vec{e_3}}_{1} + h_1 h_2 u_2 \frac{\partial h_3}{\partial \xi_2} \frac{1}{h_2} \underbrace{\vec{e_3} \cdot \vec{e_3}}_{1} + h_1 h_2 \frac{\partial u_3}{\partial \xi_3} \right] =$$

$$= \frac{1}{h_1 h_2 h_3} \left[\frac{\partial (h_2 h_3 u_1)}{\partial \xi_1} + \frac{\partial (h_1 h_3 u_2)}{\partial \xi_2} + \frac{\partial (h_1 h_2 u_3)}{\partial \xi_3} \right]$$

With analogous passages we can obtain the expression of the other operators; considering a scalar variable ϕ and a tensor of second order $\overline{\overline{T}}$ the operators read:

$$\nabla^2 (\phi) = \frac{1}{h_1 h_2 h_3} \left[\frac{\partial}{\partial \xi_1} \left(\frac{h_2 h_3}{h_1} \frac{\partial \phi}{\partial \xi_1} \right) + \frac{\partial}{\partial \xi_2} \left(\frac{h_1 h_3}{h_2} \frac{\partial \phi}{\partial \xi_2} \right) + \frac{\partial}{\partial \xi_3} \left(\frac{h_1 h_2}{h_3} \frac{\partial \phi}{\partial \xi_3} \right) \right]$$
$$\tag{A.12}$$

$$\vec{\nabla} \cdot \vec{u} = \frac{1}{h_1 h_2 h_3} \left[\frac{\partial}{\partial \xi_1} (h_2 h_3 u_1) + \frac{\partial}{\partial \xi_2} (h_1 h_3 u_2) + \frac{\partial}{\partial \xi_3} (h_1 h_2 u_3) \right] \tag{A.13}$$

$$\vec{\nabla} \times \vec{u} = \frac{\vec{e_1}}{h_2 h_3} \left[\frac{\partial}{\partial \xi_2} (h_3 u_3) - \frac{\partial}{\partial \xi_3} (h_2 u_2) \right] +$$
$$+ \frac{\vec{e_2}}{h_1 h_3} \left[\frac{\partial}{\partial \xi_3} (h_1 u_1) - \frac{\partial}{\partial \xi_1} (h_3 u_3) \right] + \tag{A.14}$$
$$+ \frac{\vec{e_3}}{h_1 h_2} \left[\frac{\partial}{\partial \xi_1} (h_2 u_2) - \frac{\partial}{\partial \xi_2} (h_1 u_1) \right]$$

$$\vec{\nabla} \cdot \overline{\overline{T}} = \vec{e_1} \left\{ \frac{1}{h_1^2 h_2 h_3} \left[\frac{\partial}{\partial \xi_1} (h_1 h_2 h_3 T_{11}) + \frac{\partial}{\partial \xi_2} (h_1^2 h_3 T_{12}) + \frac{\partial}{\partial \xi_3} (h_1^2 h_2 T_{13}) \right] + \right.$$

$$\left. - \frac{1}{h_1^2} \frac{\partial h_1}{\partial \xi_1} T_{11} - \frac{1}{h_1 h_2} \frac{\partial h_2}{\partial \xi_1} T_{22} - \frac{1}{h_1 h_3} \frac{\partial h_3}{\partial \xi_1} T_{33} \right\} +$$

$$+ \vec{e_2} \left\{ \frac{1}{h_1 h_2^2 h_3} \left[\frac{\partial}{\partial \xi_1} (h_2^2 h_3 T_{12}) + \frac{\partial}{\partial \xi_2} (h_1 h_2 h_3 T_{22}) + \frac{\partial}{\partial \xi_3} (h_2^2 h_1 T_{23}) \right] + \right.$$

$$\left. - \frac{1}{h_1 h_2} \frac{\partial h_1}{\partial \xi_2} T_{11} - \frac{1}{h_2^2} \frac{\partial h_2}{\partial \xi_2} T_{22} - \frac{1}{h_2 h_3} \frac{\partial h_3}{\partial \xi_2} T_{33} \right\} +$$

$$+ \vec{e_3} \left\{ \frac{1}{h_1 h_2 h_3^2} \left[\frac{\partial}{\partial \xi_1} (h_2 h_3^2 T_{13}) + \frac{\partial}{\partial \xi_2} (h_1 h_3^2 T_{23}) + \frac{\partial}{\partial \xi_3} (h_1 h_2 h_3 T_{33}) \right] + \right.$$

$$\left. - \frac{1}{h_1 h_3} \frac{\partial h_1}{\partial \xi_3} T_{11} - \frac{1}{h_2 h_3} \frac{\partial h_2}{\partial \xi_3} T_{22} - \frac{1}{h_3^2} \frac{\partial h_3}{\partial \xi_3} T_{33} \right\}$$
$$\tag{A.15}$$

It is also useful to report the expression of $\vec{u} \cdot \vec{\nabla} (\vec{u})$ and $\vec{u} \left(\vec{\nabla} \cdot \vec{u} \right)$:

$$\vec{u} \cdot \vec{\nabla} (\vec{u}) = +$$

$$+ \vec{e_1} \left[\frac{u_1}{h_1} \frac{\partial u_1}{\partial \xi_1} + \frac{u_2}{h_2} \frac{\partial u_1}{\partial \xi_2} + \frac{u_3}{h_3} \frac{\partial u_1}{\partial \xi_3} + \frac{u_1 u_2}{h_1 h_2} \frac{\partial h_1}{\partial \xi_2} - \frac{u_2^2}{h_1 h_2} \frac{\partial h_2}{\partial \xi_1} + \frac{u_1 u_3}{h_1 h_3} \frac{\partial h_1}{\partial \xi_3} - \frac{u_3^2}{h_1 h_3} \frac{\partial h_3}{\partial \xi_1} \right] +$$

$$+ \vec{e_2} \left[\frac{u_1}{h_1} \frac{\partial u_2}{\partial \xi_1} + \frac{u_2}{h_2} \frac{\partial u_2}{\partial \xi_2} + \frac{u_3}{h_3} \frac{\partial u_2}{\partial \xi_3} + \frac{u_1 u_2}{h_1 h_2} \frac{\partial h_2}{\partial \xi_1} - \frac{u_1^2}{h_1 h_2} \frac{\partial h_1}{\partial \xi_2} + \frac{u_2 u_3}{h_2 h_3} \frac{\partial h_2}{\partial \xi_3} - \frac{u_3^2}{h_2 h_3} \frac{\partial h_3}{\partial \xi_2} \right] +$$

$$+ \vec{e_3} \left[\frac{u_1}{h_1} \frac{\partial u_3}{\partial \xi_1} + \frac{u_2}{h_2} \frac{\partial u_3}{\partial \xi_2} + \frac{u_3}{h_3} \frac{\partial u_3}{\partial \xi_3} + \frac{u_1 u_3}{h_1 h_3} \frac{\partial h_3}{\partial \xi_1} - \frac{u_1^2}{h_1 h_3} \frac{\partial h_1}{\partial \xi_3} + \frac{u_2 u_3}{h_2 h_3} \frac{\partial h_3}{\partial \xi_2} - \frac{u_2^2}{h_2 h_3} \frac{\partial h_2}{\partial \xi_3} \right]$$
$$\tag{A.16}$$
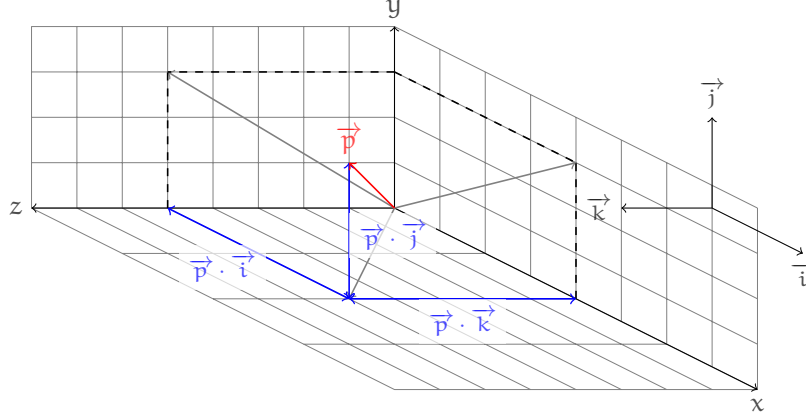
FIGURE A.1.   Orthogonal Rectangular Coordinates System (x, y, z)

$$\vec{u}\left(\vec{\nabla} \cdot \vec{u}\right) = +$$

$$+\vec{e_1}\left[\frac{u_1}{h_1}\frac{\partial u_1}{\partial \xi_1} + \frac{u_1 u_2}{h_1 h_2}\frac{\partial h_1}{\partial \xi_2} + \frac{u_1 u_3}{h_1 h_3}\frac{\partial h_1}{\partial \xi_3} + \right.$$

$$+\frac{u_1}{h_2}\frac{\partial u_2}{\partial \xi_2} + \frac{u_1^2}{h_1 h_2}\frac{\partial h_2}{\partial \xi_1} + \frac{u_1 u_3}{h_2 h_3}\frac{\partial h_2}{\partial \xi_3} +$$

$$\left. +\frac{u_1}{h_3}\frac{\partial u_3}{\partial \xi_3} + \frac{u_1^2}{h_1 h_3}\frac{\partial h_3}{\partial \xi_1} + \frac{u_1 u_2}{h_2 h_3}\frac{\partial h_3}{\partial \xi_2}\right] +$$

$$+\vec{e_2}\left[\frac{u_2}{h_1}\frac{\partial u_1}{\partial \xi_1} + \frac{u_2^2}{h_1 h_2}\frac{\partial h_1}{\partial \xi_2} + \frac{u_2 u_3}{h_1 h_3}\frac{\partial h_1}{\partial \xi_3} + \right.$$

$$+\frac{u_2}{h_2}\frac{\partial u_2}{\partial \xi_2} + \frac{u_1 u_2}{h_1 h_2}\frac{\partial h_2}{\partial \xi_1} + \frac{u_2 u_3}{h_2 h_3}\frac{\partial h_2}{\partial \xi_3} + \tag{A.17}$$

$$\left. +\frac{u_2}{h_3}\frac{\partial u_3}{\partial \xi_3} + \frac{u_1 u_2}{h_1 h_3}\frac{\partial h_3}{\partial \xi_1} + \frac{u_2^2}{h_2 h_3}\frac{\partial h_3}{\partial \xi_2}\right] +$$

$$+\vec{e_3}\left[\frac{u_3}{h_1}\frac{\partial u_1}{\partial \xi_1} + \frac{u_2 u_3}{h_1 h_2}\frac{\partial h_1}{\partial \xi_2} + \frac{u_3^2}{h_1 h_3}\frac{\partial h_1}{\partial \xi_3} + \right.$$

$$+\frac{u_3}{h_2}\frac{\partial u_2}{\partial \xi_2} + \frac{u_1 u_3}{h_1 h_2}\frac{\partial h_2}{\partial \xi_1} + \frac{u_3^2}{h_2 h_3}\frac{\partial h_2}{\partial \xi_3} +$$

$$\left. +\frac{u_3}{h_3}\frac{\partial u_3}{\partial \xi_3} + \frac{u_1 u_3}{h_1 h_3}\frac{\partial h_3}{\partial \xi_1} + \frac{u_2 u_3}{h_2 h_3}\frac{\partial h_3}{\partial \xi_2}\right]$$

A.2 Cylindrical Coordinates System

The conservations laws in cylindrical coordinates system is reported in this section.

Considering figure A.1, the transformation equations from cylindrical to rectangular system (and viceversa) are:

$$\begin{aligned} x &= x \\ y &= r\cos\vartheta \\ z &= r\sin\vartheta \end{aligned} \tag{A.18}$$

$$\begin{aligned} x &= x \\ r &= \sqrt{y^2 + z^2} \\ \vartheta &= \tan^{-1}\left(\frac{z}{y}\right) \end{aligned} \tag{A.19}$$

The base vectors of the cylindrical system are:

$$
\begin{aligned}
h_x &= \left| \frac{\partial \vec{p}}{\partial x} \right| = \left| \begin{array}{ccc} \frac{\partial x}{\partial x} & \frac{\partial y}{\partial x} & \frac{\partial z}{\partial x} \end{array} \right| = \sqrt{(1)^2 + (0)^2 + (0)^2} = 1 \\
h_r &= \left| \frac{\partial \vec{p}}{\partial r} \right| = \left| \begin{array}{ccc} \frac{\partial x}{\partial r} & \frac{\partial y}{\partial r} & \frac{\partial z}{\partial r} \end{array} \right| = \sqrt{(0)^2 + (\cos \vartheta)^2 + (\sin \vartheta)^2} = 1 \\
h_\vartheta &= \left| \frac{\partial \vec{p}}{\partial \vartheta} \right| = \left| \begin{array}{ccc} \frac{\partial x}{\partial \vartheta} & \frac{\partial y}{\partial \vartheta} & \frac{\partial z}{\partial \vartheta} \end{array} \right| = \sqrt{(0)^2 + (-r \sin \vartheta)^2 + (r \cos \vartheta)^2} = r
\end{aligned}
\tag{A.20}
$$

Thus the metric tensor is:

$$
T_{metric} = \begin{bmatrix} 1 & 0 & 0 \\ 0 & 1 & 0 \\ 0 & 0 & r \end{bmatrix}
\tag{A.21}
$$

The curvilinear basis unit vectors can be expressed as:

$$
\vec{e_x} = \frac{1}{h_x} \frac{\partial \vec{p}}{\partial x} = \frac{1}{1} \frac{\partial \vec{p}}{\partial x} \quad \vec{e_r} = \frac{1}{h_r} \frac{\partial \vec{p}}{\partial r} = \frac{1}{1} \frac{\partial \vec{p}}{\partial r} \quad \vec{e_\vartheta} = \frac{1}{h_3} \frac{\partial \vec{p}}{\partial \vartheta} = \frac{1}{r} \frac{\partial \vec{p}}{\partial \vartheta}
\tag{A.22}
$$

We note that the only metric derivative not null is:

$$
\frac{\partial h_3}{\partial \xi_2} = \frac{\partial h_\vartheta}{\partial r} = \frac{\partial r}{\partial r} = 1
\tag{A.23}
$$

We can now calculate the expression of the conservation laws in cylindrical system. Consider the following system of equations:

$$
\begin{aligned}
&\frac{\partial \rho}{\partial t} + \vec{\nabla} \cdot (\rho \vec{u}) = 0 \\
&\frac{\partial (\rho \vec{u})}{\partial t} + \vec{\nabla} \cdot (\rho \vec{u} \vec{u}) + \vec{\nabla}(p) = \vec{\nabla} \cdot \left(\overline{\overline{T}} \right) \\
&\frac{\partial (\rho E)}{\partial t} + \vec{\nabla} \cdot \left(\vec{B} \right) = 0
\end{aligned}
\tag{A.24}
$$

where $\overline{\overline{T}}$ is a tensor (of generic viscous terms), $\vec{B}$ is generic vector and where:

$$
\vec{\nabla} \cdot (\rho \vec{u} \vec{u}) = \vec{u} \cdot \vec{\nabla}(\rho \vec{u}) + \rho \vec{u} \left(\vec{\nabla} \cdot \vec{u} \right)
\tag{A.25}
$$

Using the expression A.13 for the cylindrical system we obtain:

$$
\vec{\nabla} \cdot (\rho \vec{u}) = \frac{1}{r} \left[\frac{\partial}{\partial x}(r\rho u) + \frac{\partial}{\partial r}(r\rho u_r) + \frac{\partial}{\partial \vartheta}(\rho u_\vartheta) \right]
\tag{A.26}
$$

where $\vec{u} = \begin{bmatrix} u & u_r & u_\vartheta \end{bmatrix}$. Using the expression A.16 and A.17 for the cylindrical system we obtain:

$$
\begin{aligned}
\vec{u} \cdot \vec{\nabla}(\rho \vec{u}) = &+ \\
&+ \vec{e_x} \left[u \frac{\partial (\rho u)}{\partial x} + u_r \frac{\partial (\rho u)}{\partial r} + \frac{u_\vartheta}{r} \frac{\partial (\rho u)}{\partial \vartheta} \right] + \\
&+ \vec{e_r} \left[u \frac{\partial (\rho u_r)}{\partial x} + u_r \frac{\partial (\rho u_r)}{\partial r} + \frac{u_\vartheta}{r} \frac{\partial (\rho u_r)}{\partial \vartheta} - \frac{\rho u_\vartheta^2}{r} \right] + \\
&+ \vec{e_\vartheta} \left[u \frac{\partial (\rho u_\vartheta)}{\partial \xi_1} + u_r \frac{\partial (\rho u_\vartheta)}{\partial \xi_2} + \frac{u_\vartheta}{r} \frac{\partial (\rho u_\vartheta)}{\partial \vartheta} + \frac{\rho u_r u_\vartheta}{r} \right]
\end{aligned}
\tag{A.27}
$$

$$\rho \vec{u} \left(\vec{\nabla} \cdot \vec{u} \right) = +$$
$$+ \vec{e_x} \left[\rho u \frac{\partial u}{\partial x} + \rho u \frac{\partial u_r}{\partial r} + \frac{\rho u}{r} \frac{\partial u_\vartheta}{\partial \vartheta} + \frac{\rho u u_r}{r} \right] +$$
$$+ \vec{e_r} \left[\rho u_r \frac{\partial u}{\partial x} + \rho u_r \frac{\partial u_r}{\partial r} + \frac{\rho u_r}{r} \frac{\partial u_\vartheta}{\partial \vartheta} + \frac{\rho u_r^2}{r} \right] +$$
$$+ \vec{e_\vartheta} \left[\rho u_\vartheta \frac{\partial u}{\partial x} + \rho u_\vartheta \frac{\partial u_r}{\partial r} + \frac{\rho u_\vartheta}{r} \frac{\partial u_\vartheta}{\partial \vartheta} + \frac{\rho u_r u_\vartheta}{r} \right]$$

(A.28)

Adding A.27 and A.28 we obtain:

$$\vec{\nabla} \cdot \left(\rho \vec{u} \vec{u} \right) = \vec{u} \cdot \vec{\nabla} \left(\rho \vec{u} \right) + \rho \vec{u} \left(\vec{\nabla} \cdot \vec{u} \right) = +$$
$$+ \vec{e_x} \left[\frac{\partial (\rho u^2)}{\partial x} + \frac{\partial (\rho u u_r)}{\partial r} + \frac{1}{r} \frac{\partial (\rho u u_\vartheta)}{\partial \vartheta} + \frac{\rho u u_r}{r} \right] +$$
$$+ \vec{e_r} \left[\frac{\partial (\rho u_r u)}{\partial x} + \frac{\partial (\rho u_r^2)}{\partial r} + \frac{1}{r} \frac{\partial (\rho u_r u_\vartheta)}{\partial \vartheta} + \frac{\rho u_r^2 - \rho u_\vartheta^2}{r} \right] +$$
$$+ \vec{e_\vartheta} \left[\frac{\partial (\rho u_\vartheta u)}{\partial x} + \frac{\partial (\rho u_\vartheta u_r)}{\partial r} + \frac{1}{r} \frac{\partial (\rho u_\vartheta^2)}{\partial \vartheta} + \frac{2 \rho u_r u_\vartheta}{r} \right]$$

(A.29)

The gradient of pressure in cylindrical coordinates is:

$$\vec{\nabla} (p) = \vec{e_x} \frac{\partial (p)}{\partial x} + \vec{e_r} \frac{\partial (p)}{\partial r} + \frac{\vec{e_\vartheta}}{r} \frac{\partial (p)}{\partial \vartheta}$$

(A.30)

For the divergence of the tensor $\overline{\overline{T}}$ using the A.15 we obtain:

$$\vec{\nabla} \cdot \overline{\overline{T}} = +$$
$$+ \frac{\vec{e_x}}{r} \left[\frac{\partial (r T_{xx})}{\partial x} + \frac{\partial (r T_{xr})}{\partial r} + \frac{\partial T_{x\vartheta}}{\partial \vartheta} \right] +$$
$$+ \frac{\vec{e_r}}{r} \left[\frac{\partial (r T_{xr})}{\partial x} + \frac{\partial (r T_{rr})}{\partial r} + \frac{\partial T_{r\vartheta}}{\partial \vartheta} - T_{\vartheta\vartheta} \right] +$$
$$+ \frac{\vec{e_\vartheta}}{r^2} \left[\frac{\partial (r^2 T_{x\vartheta})}{\partial x} + \frac{\partial (r^2 T_{r\vartheta})}{\partial r} + \frac{\partial (r T_{\vartheta\vartheta})}{\partial \vartheta} \right]$$

(A.31)

Finally the divergence of vector $\vec{B}$ in cylindrical system is:

$$\vec{\nabla} \cdot \left(\vec{B} \right) = \frac{1}{r} \left[\frac{\partial}{\partial x} (r B_x) + \frac{\partial}{\partial r} (r B_r) + \frac{\partial}{\partial \vartheta} (B_\vartheta) \right]$$

(A.32)

Using the equations A.26, A.29, A.30, A.31 and A.32 the system of conservation laws in cylindrical coordinates can expressed as:

$$\frac{\partial \rho}{\partial t} + \frac{1}{r} \left[\frac{\partial}{\partial x} (r \rho u) + \frac{\partial}{\partial r} (r \rho u_r) + \frac{\partial}{\partial \vartheta} (\rho u_\vartheta) \right] = 0$$
$$\frac{\partial (\rho u)}{\partial t} + \frac{\partial}{\partial x} (\rho u^2 + p) + \frac{\partial}{\partial r} (\rho u u_r) + \frac{1}{r} \frac{\partial}{\partial \vartheta} (\rho u u_\vartheta) + \frac{\rho u u_r}{r} = +$$
$$+ \frac{1}{r} \left[\frac{\partial (r T_{xx})}{\partial x} + \frac{\partial (r T_{xr})}{\partial r} + \frac{\partial T_{x\vartheta}}{\partial \vartheta} \right]$$
$$\frac{\partial (\rho u_r)}{\partial t} + \frac{\partial}{\partial x} (\rho u_r u) + \frac{\partial}{\partial r} (\rho u_r^2 + p) + \frac{1}{r} \frac{\partial}{\partial \vartheta} (\rho u_r u_\vartheta) + \frac{\rho u_r^2 - \rho u_\vartheta^2}{r} = +$$
$$+ \frac{1}{r} \left[\frac{\partial (r T_{xr})}{\partial x} + \frac{\partial (r T_{rr})}{\partial r} + \frac{\partial T_{r\vartheta}}{\partial \vartheta} - T_{\vartheta\vartheta} \right]$$
$$\frac{\partial (\rho u_\vartheta)}{\partial t} + \frac{\partial}{\partial x} (\rho u_\vartheta u) + \frac{\partial}{\partial r} (\rho u_\vartheta u_r) + \frac{1}{r} \frac{\partial}{\partial \vartheta} (\rho u_\vartheta^2 + p) + \frac{2 \rho u_r u_\vartheta}{r} = +$$
$$+ \frac{1}{r^2} \left[\frac{\partial (r^2 T_{x\vartheta})}{\partial x} + \frac{\partial (r^2 T_{r\vartheta})}{\partial r} + \frac{\partial (r T_{\vartheta\vartheta})}{\partial \vartheta} \right]$$
$$\frac{\partial (\rho E)}{\partial t} + \frac{1}{r} \left[\frac{\partial}{\partial x} (r B_x) + \frac{\partial}{\partial r} (r B_r) + \frac{\partial}{\partial \vartheta} (B_\vartheta) \right] = 0$$

(A.33)

Multiplying all terms of A.33 for r the conservation laws in cylindrical coordinates read:

$$
\begin{aligned}
&\frac{\partial(r\rho)}{\partial t} + \frac{\partial}{\partial x}(r\rho u) + \frac{\partial}{\partial r}(r\rho u_r) + \frac{\partial}{\partial\vartheta}(\rho u_\vartheta) = 0 \\
&\frac{\partial(r\rho u)}{\partial t} + \frac{\partial}{\partial x}\left[r\left(\rho u^2 + p\right)\right] + \frac{\partial}{\partial r}(r\rho u u_r) + \frac{\partial}{\partial\vartheta}(\rho u u_\vartheta) = + \\
&\qquad\qquad + \frac{\partial(rT_{xx})}{\partial x} + \frac{\partial(rT_{xr})}{\partial r} + \frac{\partial T_{x\vartheta}}{\partial\vartheta} \\
&\frac{\partial(r\rho u_r)}{\partial t} + \frac{\partial}{\partial x}(r\rho u_r u) + \frac{\partial}{\partial r}\left[r\left(\rho u_r^2 + p\right)\right] + \frac{\partial}{\partial\vartheta}(\rho u_r u_\vartheta) = p + \rho u_\vartheta^2 + \\
&\qquad\qquad + \frac{\partial(rT_{xr})}{\partial x} + \frac{\partial(rT_{rr})}{\partial r} + \frac{\partial T_{r\vartheta}}{\partial\vartheta} - T_{\vartheta\vartheta} \\
&\frac{\partial(r\rho u_\vartheta)}{\partial t} + \frac{\partial}{\partial x}(r\rho u_\vartheta u) + \frac{\partial}{\partial r}(r\rho u_\vartheta u_r) + \frac{\partial}{\partial\vartheta}\left(\rho u_\vartheta^2 + p\right) = -\rho u_r u_\vartheta + \\
&\qquad\qquad + \frac{1}{r}\left[\frac{\partial\left(r^2 T_{x\vartheta}\right)}{\partial x} + \frac{\partial\left(r^2 T_{r\vartheta}\right)}{\partial r} + \frac{\partial\left(r T_{\vartheta\vartheta}\right)}{\partial\vartheta}\right] \\
&\frac{\partial(r\rho E)}{\partial t} + \frac{\partial}{\partial x}(rB_x) + \frac{\partial}{\partial r}(rB_r) + \frac{\partial}{\partial\vartheta}(B_\vartheta) = 0
\end{aligned}
\tag{A.34}
$$

Noting that:

$$
\begin{aligned}
&\frac{1}{r}\left[\frac{\partial\left(r^2 T_{x\vartheta}\right)}{\partial x} + \frac{\partial\left(r^2 T_{r\vartheta}\right)}{\partial r} + \frac{\partial\left(r T_{\vartheta\vartheta}\right)}{\partial\vartheta}\right] = \\
&= \frac{\partial}{\partial x}\left(\frac{r^2}{r}T_{x\vartheta}\right) + \frac{\partial}{\partial r}\left(\frac{r^2}{r}T_{r\vartheta}\right) - r^2 T_{r\vartheta}\frac{\partial}{\partial r}\left(\frac{1}{r}\right) + \frac{\partial}{\partial\vartheta}\left(\frac{r}{r}T_{\vartheta\vartheta}\right) = \\
&= \frac{\partial}{\partial x}(rT_{x\vartheta}) + \frac{\partial}{\partial r}(rT_{r\vartheta}) - r^2 T_{r\vartheta}\cdot\left(-\frac{1}{r^2}\right) + \frac{\partial}{\partial\vartheta}(T_{\vartheta\vartheta}) = \\
&= \frac{\partial}{\partial x}(rT_{x\vartheta}) + \frac{\partial}{\partial r}(rT_{r\vartheta}) + T_{r\vartheta} + \frac{\partial}{\partial\vartheta}(T_{\vartheta\vartheta})
\end{aligned}
$$

the conservation laws in cylindrical coordinates become:

$$
\begin{aligned}
&\frac{\partial(r\rho)}{\partial t} + \frac{\partial}{\partial x}(r\rho u) + \frac{\partial}{\partial r}(r\rho u_r) + \frac{\partial}{\partial\vartheta}(\rho u_\vartheta) = 0 \\
&\frac{\partial(r\rho u)}{\partial t} + \frac{\partial}{\partial x}\left[r\left(\rho u^2 + p\right)\right] + \frac{\partial}{\partial r}(r\rho u u_r) + \frac{\partial}{\partial\vartheta}(\rho u u_\vartheta) = + \\
&\qquad\qquad + \frac{\partial(rT_{xx})}{\partial x} + \frac{\partial(rT_{xr})}{\partial r} + \frac{\partial T_{x\vartheta}}{\partial\vartheta} \\
&\frac{\partial(r\rho u_r)}{\partial t} + \frac{\partial}{\partial x}(r\rho u_r u) + \frac{\partial}{\partial r}\left[r\left(\rho u_r^2 + p\right)\right] + \frac{\partial}{\partial\vartheta}(\rho u_r u_\vartheta) = p + \rho u_\vartheta^2 + \\
&\qquad\qquad + \frac{\partial(rT_{xr})}{\partial x} + \frac{\partial(rT_{rr})}{\partial r} + \frac{\partial T_{r\vartheta}}{\partial\vartheta} - T_{\vartheta\vartheta} \\
&\frac{\partial(r\rho u_\vartheta)}{\partial t} + \frac{\partial}{\partial x}(r\rho u_\vartheta u) + \frac{\partial}{\partial r}(r\rho u_\vartheta u_r) + \frac{\partial}{\partial\vartheta}\left(\rho u_\vartheta^2 + p\right) = -\rho u_r u_\vartheta + T_{r\vartheta} + \\
&\qquad\qquad + \frac{\partial}{\partial x}(rT_{x\vartheta}) + \frac{\partial}{\partial r}(rT_{r\vartheta}) + \frac{\partial}{\partial\vartheta}(T_{\vartheta\vartheta}) \\
&\frac{\partial(r\rho E)}{\partial t} + \frac{\partial}{\partial x}(rB_x) + \frac{\partial}{\partial r}(rB_r) + \frac{\partial}{\partial\vartheta}(B_\vartheta) = 0
\end{aligned}
$$

$$
\tag{A.35}
$$

B

Multi-Resolution Code Overview

THE numerical algorithm presented in chapter 4 on page 36 has been implemented into the HeaRT (Heat Release and Transfer) numerical code. HeaRT is written in standard Fortran 95, with partial use of OOP (Object Oriented Programming) and is parallelized using Message Parsing Interface (MPI) standard.

The joined-grids algorithm is made up by 3 different modules:

1. The memory allocator (MA) module.

2. The joined grids geometric evaluation (GE) module.

3. The coarse-fine grids coupling (GC) module.

At the beginning of the numerical simulation, after that the computational domain has been decomposed between all the available cores and that the domain topology geometric characteristics have been evaluated, MA module allocates all the variables and parameters necessary to the fine to coarse and coarse to fine data transfer; after that, GE module evaluates all these quantities. Then the numerical integration starts, and at every time step GC module transfers data for any coarse-fine grid interface.

B.1 The Memory Allocator Module

The MM module is assigned to the memory management: for any zone in the processor domain it browses the three coordinate directions (I, J, K) searching for a finest grid at the beginning or at the end of the zone; if this finest zone exists, the following variables will be allocated:

- for any ghost coarse cell and for any coarse cell overlapping fine ghost cells, volume fractions of the fine cells that form a single coarse cell;

- for any ghost coarse cell and for any coarse cell overlapping fine ghost cells, surface area fractions, for any coordinate direction, of the fine cell surfaces that form a single coarse cell surface;

these two quantities are used for scalar and momentum restriction (section 4.2.2.1 on page 40) and for the conservation control after prolongation (section 4.2.2.2 on page 43).

Furthermore, for any fine ghost cell, the following variables will be allocated:

- the geometric distance between any point of the interpolation domain and the fine point where the variable has to be interpolated (one for scalars, one for each momentum component);

- the geometric distance, one for each coordinate direction, between the centroid of the interpolation domain and all the points that belong to the interpolation stencil (one for scalars, one for each momentum component);

- the geometric distance, one for each coordinate direction, between the centroid of the interpolation domain and the fine point where the variable has to be interpolated (one for scalars, one for each momentum component);

- the coordinate indexes of all the points (coarse and fine) that belong to the interpolation stencil.

B.2 The Geometric Evaluation Module

The GM module follows the scheme adopted in the MM module and evaluates all the variables that have been previously allocated. Specific care is been addressed to the correct composition of the interpolation stencil; after that the connection direction (I, J or K) is been identified (for example, I), the following steps are carried out:

1. if the interpolation centroid is "far" from the fine zone borders, the interpolation stencil can be composed only by coarse points also in the I direction (figure 4.7d on page 47);

2. if the interpolation centroid is adjacent to the fine cell border, in the interpolation stencil must be included also fine grid points: their number depends on the interpolation centroid position compared with the fine grid borders in the J and K directions; if the centroid is far from J and K fine zone borders, the first (or the last) interpolation stencil row in I direction is composed by only fine points (figure 4.7a on page 47); if the centroid is adjacent to a J or K (or both) fine border, the first (or the last) interpolation stencil row in I direction is composed by both fine and coarse points (figures 4.7b on page 47 and 4.7c on page 47).

This phase is really heavy in terms of computing time, because it involves a lot of conditional constructs, but it runs once at the beginning of the numerical simulation, so this aspect isn't so important.

B.3 The Coarse-Fine Grids Coupling Module

This module connects, at every substep of the Runge-Kutta algorithm, the edge of a fine zone that adjoins a coarsest one, and vice-versa. First, the connection
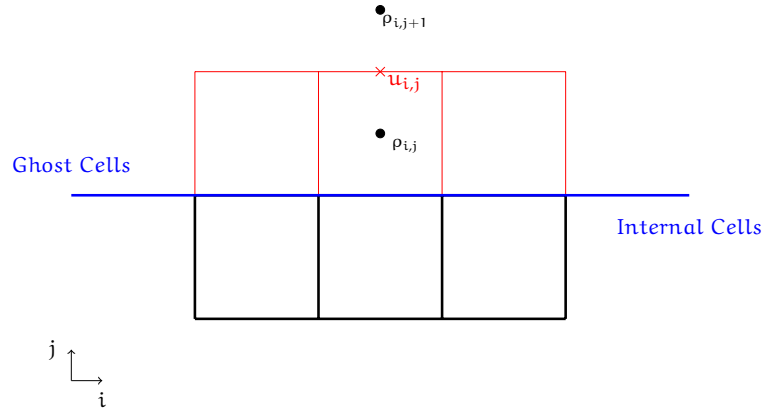
FIGURE B.1. "Extra" ghost for u evaluation

between different resolution zones is done for chemical species mass fractions, then for the momentum components; after the connection is made for pressure, temperature, density and total energy. Since the interpolation stencil are composed by only "true" integrated points, the connection between zones isn't hold to follow a precise order, but can take place indifferently first from fine to coarse grid or vice-versa: in the CM module, the communication occurs first from fine to coarse and then from coarse to fine.

Because of the use of a staggered grid, in the velocity and in the total energy evaluation processes an "extra" ghost is necessary.

A single velocity component u, is evaluated from the same component momentum ρu and from the density ρ, as $u = \rho u / \rho$; when the "upper" ghost cell velocity has to be calculated (figure B.1), the necessary $\rho_{i,j+1}$ doesn't exist in the flow field and also in the data structure ρ for that zone: so a dummy variable ρ_{gh+} is been allocated and by means of prolongation or restriction procedure, the value of $\rho_{i,j+1}$ is been evaluated and stored in ρ_{gh+}. After that is possible to calculate the ρ at the scalar cell interface and subsequently the u.

The same need is visible when the total energy has to been evaluated in the "lower" ghost cell (figure B.2 on the following page): the total energy, indeed, is calculated as a sum of the kinetic and the internal energy of the cell, but to evaluated the kinetic energy in the "scalar" cell, both $\rho u_{i,j}$ and $\rho u_{i,j-1}$ must be known; the variable $\rho u_{i,j-1}$ doesn't exist in the flow field and in the ρu data structure for this zone, so a dummy variable ρu_{gh-} is been allocated and by means of prolongation or restriction procedure, the value of $\rho u_{i,j-1}$ is been evaluated and stored in ρu_{gh-}. After that, the value of internal energy U can be calculated.

B.4 FUTURE DEVELOPMENTS: MULTI-LEVEL APPROACH

The Joined Grid algorithm presented in chapter 4 on page 36 can be easily evolved in a Multi-level algorithm, where on the entire domain there is a coarse grid and in specific zones, where is foreseeable the presence of high gradients and little vortexes, finest grid levels are generated "a priori", that is before that numeri-
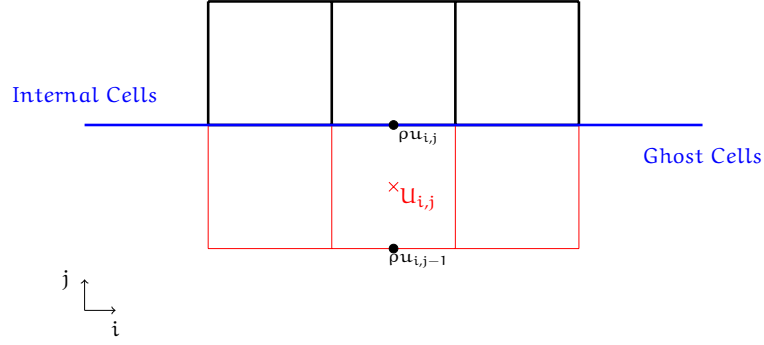
FIGURE B.2. "Extra" ghost for U evaluation

cal simulation begins. Also in this case is possible to define a refinement ratio, assumed the same between neighboring levels and for each direction, that is:

$$\frac{\Delta x_1}{\Delta x_2} = \frac{\Delta x_2}{\Delta x_3} = \cdots = \frac{\Delta x_{l-1}}{\Delta x_l} = r$$

$$\frac{\Delta y_1}{\Delta y_2} = \frac{\Delta y_2}{\Delta y_3} = \cdots = \frac{\Delta y_{l-1}}{\Delta y_l} = r \qquad \text{(B.1)}$$

$$\frac{\Delta z_1}{\Delta z_2} = \frac{\Delta z_2}{\Delta z_3} = \cdots = \frac{\Delta z_{l-1}}{\Delta z_l} = r$$

where Δx, Δy and Δz are grid spacings for the three directions and subscripts are level indexes: it is straightforward that in a one-dimensional grid, a coarse cell can contain only 2 fine cells, while for a bi-dimensional grid 4 fine cells are contained in a coarse one and in a three-dimensional grid a coarse cell contains 8 fine cells.

In case of a uniform coarse grid, fine levels are easily obtained dividing in n identical fine cells a single coarse cell (with $n = 2, 4, 8$); if coarse grid is non-uniform, this approach isn't applicable because fine grid obtained will display discontinuities on fine grid cell dimensions. To solve this problem is possible to map coarse grid stretched grid points in an artificial coordinate system in which the grid is uniform spaced: from this "uniform" grid fine cells can be obtained by simple division and fine points extracted in this fake coordinate system are brought back to the original "real" coordinate system. In this way not only coarse grid spacing but also fine grid spacing is coherent with the original stretching function.

Coarsest level has number 1 and the level number increase as grid refinement; fine grid are also properly nested: all level l fine points have to be contained into level $l-1$ grid, except boundary condition points (inlets, outlets and walls).

The two communication procedures, described in 4.2.2 on page 39 can be used also in a multi-level algorithm: the prolongation procedure remains the same, while the restriction procedure needs some little modifications: the information transfer, indeed, must take place on *internal points*, that is to say grid points where numerical solution is calculated on level l grid (yellow cells in figure B.3 on the next page).
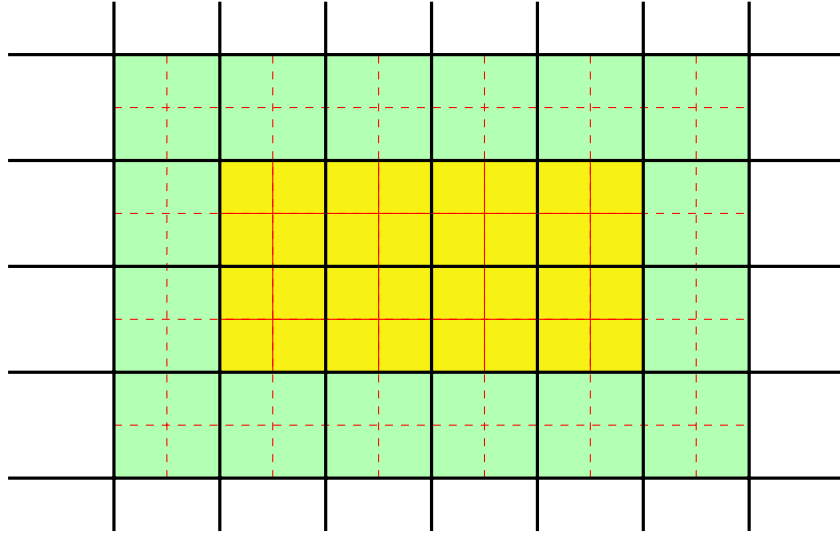
Figure B.3. Grids mutual position

B.4.1 Solution Algorithm

In the solution algorithm, each level solves conservation equations independently from other levels: level communications don't take place during a time step but at the end of Runge-Kutta procedure. In particular, communication between level l and level $l-1$ (or $l+1$) happens only when the two levels are at the same instant. So fine levels, to ensure CFL condition respect, must fulfill a multiple of time step of the previous (coarser) level, to reach the same instant and carry out communication: each level, indeed, evaluates its own δt that ensure stability conditions of its own grid.

Solution algorithm is illustrated in figure B.4 on the following page, where for the sake of simplicity, only 3 grid levels are considered.

Time integration procedure is here described:

1. *Prolongation* of boundary conditions at time t_{in} from level 1 to level 2;

2. *Prolongation* of boundary conditions at time t_{in} from level 2 to level 3;

3. *Temporal Integration* of level 1 grid, from t_{in} to t_{fin};

4. *Temporal Integration* of level 2 grid, from t_{in} to $t_{fin_2} \neq t_{fin}$;

5. *Temporal Integration* of level 3 grid, from t_{in} to $t_{fin_2} \neq t_{fin}$, by the means of p_1 time steps, while fine grid boundary condition are keep blocked at time t_{in};

6. *Prolongation* of boundary conditions at time t_{fin_2} from level 2 to level 3;

7. *Restriction* of solution at time t_{fin_2} from level 3 to level 2;

8. *Temporal Integration* of level 2 grid, da t_{fin_2} a t_{fin_3};
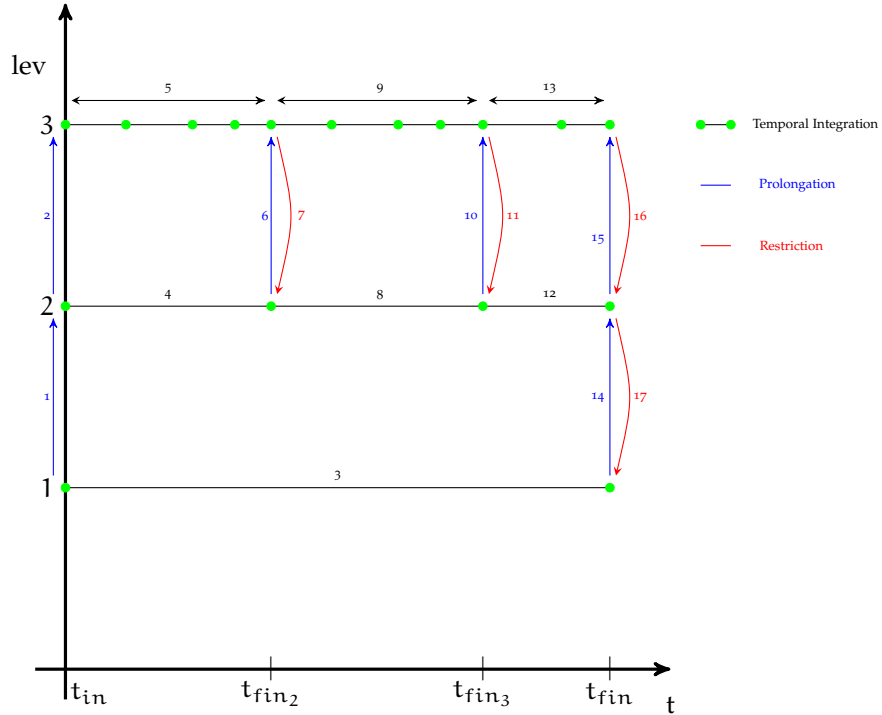
FIGURE B.4. Scheme of temporal advance on all grid levels

9. *Temporal Integration* of level 3 grid, da t_{fin_2} a $t_{fin_3} \neq t_{fin}$, by the means of p_2 time steps, while fine grid boundary condition are keep blocked at time t_{fin_2};

10. *Prolongation* of boundary conditions at time t_{fin_3} from level 2 to level 3;

11. *Restriction* of solution at time t_{fin_3} from level 3 to level 2;

12. *Temporal Integration* of level 2 grid, da t_{fin_3} a t_{fin};

13. *Temporal Integration* of level 3 grid, da t_{fin_3} a t_{fin}, by the means of p_3 time steps, while fine grid boundary condition are keep blocked at time t_{fin_3};

14. *Prolongation* of boundary conditions at time t_{fin} from level 1 to level 2;

15. *Prolongation* of boundary conditions at time t_{fin} from level 2 to level 3;

16. *Restriction* of solution at time t_{fin} from level 3 to level 2;

17. *Restriction* of solution at time t_{fin} from level 2 to level 1;

So HeaRT solver routine is been changed in a recursive procedure, in which level l, after completing its time integration, recalls solver routine for the following (if present) $l + 1$ level, that repeats the same operation until finest level is reached. After, finest level l_n catch up with $l_n - 1$ level by the means of p time

steps and so on, until all level catch up level 1. After that conservative equation integration is completed and the first level passes to the next time step.

In this algorithm, level communications are very important, because by the means of these communications all grid levels are tied each other and all grids flow fields are coherent, also if it's possible some difference due to the different spatial resolution between grid levels.

For example, in a turbulent flow field, little whirling structures motion has a big impact on macroscopic mixing of the fluid: if finest grid, that can "see" and solve little vortexes, doesn't transfer numerical solution to coarser levels, flow field on these levels (that because of their spatial resolution cannot solve so little structures) can be very different to the fine grid solution, because the mixing mechanism isn't well predicted.

Furthermore, fine grid boundary conditions are obtained by the means of prolongation from coarser level flow field, so if on coarser level numerical solution isn't in agreement with the solution on fine grid, level l will transfer "wrong" boundary conditions on level $l + 1$ and numerical solution on level $l + 1$ will start to distance from the "correct" solution evaluated on the previous time step: grids communications at certain instants are mandatory for a right implementation of a multi-level approach.

The algorithm is been chosen after an in-depth analysis of HeaRT code features: multi-block structured grids are well mixed with multiple overlapped grid levels; blocked boundary conditions and restriction from fine to coarse level ensure that all levels remain dependent each other. The entire flow field covered with a coarse grid allows to insert fine levels where at the beginning they weren't expected, without altering the complete domain: so evolved flow fields can be used as inputs for new simulations, without a restart from a fixed and uniform field.

C

Boundary Conditions Analysis

In HeaRT code, non reflecting boundary condition approach is called NSCBC (Navier-Stokes Characteristic Boundary Conditions): such approach permits to solve reflecting waves problem into flow field from a non reflecting inlet or outlet. NSCBC approach consists to solve Navier-Stokes equation on non-reflecting boundaries in terms of incident acoustic waves amplitude on the boundary itself; orthogonal derivatives are solved by the means of a non centered first order numerical scheme that uses numerical data that come from the internal flow field. Also if accuracy order at non-reflecting boundaries is lower than the remaining field, global accuracy is of the same order of the numerical scheme adopted into the internal points.

Red line in figure C.1 is the physical boundary when a non reflecting outlet boundary condition is imposed; on the right side of the red line there's the internal field, while in left side there are "ghost" cell used for numerical integration.

The algorithm is the following:
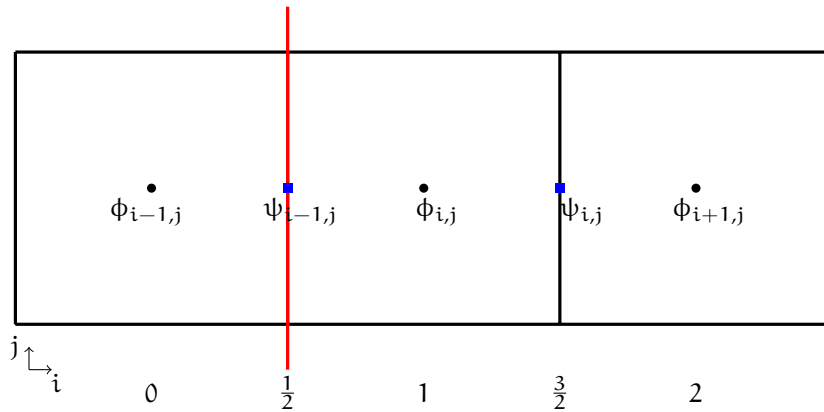
FIGURE C.1. Scheme for boundary condition

1. is necessary to calculate λ_1, λ_2, λ_3, that in this case assume the values:

$$\lambda_1 = u + a \tag{C.1}$$

$$\lambda_2 = u - a \tag{C.2}$$

$$\lambda_3 = u \tag{C.3}$$

where u is flow field in j direction in point 1, (obtained dividing mass fluxes average in $\frac{1}{2}$ and $\frac{3}{2}$ by flow density if point 1) and a is sound velocity calculated in point 1;

2. *first order derivative* are obtained on the boundary from:

$$\frac{\partial u}{\partial x} = \frac{u_1 - u_{\frac{1}{2}}}{\frac{\delta x}{2}} \tag{C.4}$$

$$\frac{\partial p}{\partial x} = \frac{p_2 - p_1}{\delta x} \tag{C.5}$$

$$\frac{\partial \rho}{\partial x} = \frac{\rho_2 - \rho_1}{\delta x} \tag{C.6}$$

$$\frac{\partial T}{\partial x} = \frac{T_2 - T_1}{\delta x} \tag{C.7}$$

where δ_x is the uniform grid spacing in i direction;

3. the following values are calculated:

$$d_1 = \frac{\left[\lambda_3 \left(a^2 \rho_x - p_x\right)\right] + \frac{1}{2}\lambda_2 \left(p_x - \rho a u_x\right)}{a^2} \tag{C.8}$$

$$d_2 = \frac{1}{2}\lambda_2 \left(p_x - \rho a u_x\right) \tag{C.9}$$

$$d_3 = \frac{-\frac{1}{2}\left[\lambda_2 \left(p_x - \rho a u_x\right)\right]}{\rho a} \tag{C.10}$$

where notation $\frac{\partial [..]}{\partial x}$ is substituted by the $[..]_x$.

At this point, d_1, d_2, d_3 values are used into HeaRT solver to change numerical integration scheme for the cell that lie on the non-reflecting boundary: this operation is repeated for any Runge-Kutta substep.

c.1 New Boundary Conditions

With the aim to obtain an easiest procedure for non-reflecting boundary conditions, some attempts have been accomplished: the first, and easiest, is to copy first (or last, depending on which boundary it's been considered) flow field point value on ghost cells; in this manner numerical scheme isn't modified and local order of accuracy is the same for boundary and for internal points.

To improve awful results obtained by the means of extrapolation (see C.2 on page 116), a new boundary condition, named "FaRo", is been introduced: with this boundary condition, the order of accuracy isn't modified; at the boundary the same variables used in the internal points are evaluated and employed in numerical integration of conservation laws. The procedure is the following (see figure C.1 on the previous page):

1. in point $\frac{1}{2}$ velocity in i direction, pressure and density are evaluated; velocity is collocated in that point, while pressure and density are calculated by the means of:

$$p_{\frac{1}{2}} = \frac{p_0 + p_1}{2} \tag{C.11}$$

$$rho_{\frac{1}{2}} = \frac{\rho_0 + \rho_1}{2} \tag{C.12}$$

2. in point 1 velocity and density are evaluated:

$$u_1 = \frac{u_{\frac{1}{2}} + u_{\frac{3}{2}}}{2} \tag{C.13}$$

$$\rho_1 = \frac{\left(\frac{\rho_0 + \rho_1}{2}\right) + \left(\frac{\rho_1 + \rho_2}{2}\right)}{2} \tag{C.14}$$

3. pressure, density and velocity derivative in i direction are evaluated:

$$u_x = \frac{\left(u_{\frac{3}{2}} - u_{\frac{1}{2}}\right)}{\delta_x} \tag{C.15}$$

$$\rho_x = \frac{\left(\frac{\rho_1 + \rho_2}{2}\right) - \left(\frac{\rho_0 + \rho_1}{2}\right)}{\delta_x} \tag{C.16}$$

$$p_x = \frac{\left(\frac{p_1 + p_2}{2}\right) - \left(\frac{p_0 + p_1}{2}\right)}{\delta_x} \tag{C.17}$$

4. sound velocity in point 1 is evaluated:

$$a_1 = \frac{\left(\frac{a_0 + a_1}{2}\right) + \left(\frac{a_1 + a_2}{2}\right)}{2} \tag{C.18}$$

5. pressure, density and velocity time derivatives in point $\frac{1}{2}$ are evaluated and integrated by the means of Runge-Kutta method used for internal points.

6. by the means of the variables $p_{\frac{1}{2}}$, $\rho_{\frac{1}{2}}$, $u_{\frac{1}{2}}$ just now calculated, temperature, total energy, etc...., are evaluated; the following values on ghost cells are evaluated by the means of:

$$p(0) = 2p_{\frac{1}{2}} - p_1 \tag{C.19}$$

$$rho(0) = 2\rho_{\frac{1}{2}} - \rho_1 \tag{C.20}$$

$$u(0) = u_{\frac{1}{2}} \tag{C.21}$$

$$T(0) = 2T_{\frac{1}{2}} - T_1 \tag{C.22}$$

$$Utot(0) = 2Utot_{\frac{1}{2}} - Utot_1 \tag{C.23}$$

where, with 0 index number, are indicated variables that belong to the cell with staggering;

7. variables values on ghost cells are used to integrate boundary points, without any modification to the numerical scheme adopted.

An additional step is to simplify "FaRo" boundary conditions, introducing a new procedure, named "FaRo NEW": at any Runge-Kutta substep, some variables necessary to the numerical integration of conservation equations are evaluated, as follow (see figure C.1 on page 112):

1. the following values are evaluated:

$$p_{\frac{1}{2}} = \frac{1}{2} \left[p_{iniz} + p_1 + \rho_1 a_1 \left(u_{iniz} - u_{\frac{3}{2}} \right) \right] \tag{C.24}$$

$$\rho_{\frac{1}{2}} = \frac{1}{a^2} \left(p_1 - p_{iniz} \right) + \rho_{iniz} \quad \text{se} \quad u_{\frac{3}{2}} < 0 \tag{C.25}$$

$$\rho_{\frac{1}{2}} = \frac{1}{a^2} \left(p_1 - p_{iniz} \right) + \rho_1 \quad \text{se} \quad u_{\frac{3}{2}} \geqslant 0 \tag{C.26}$$

$$u_{\frac{1}{2}} = \frac{\left(p_1 - p_{iniz} \right)}{\left(\rho_1 a_1 \right)} + u_{\frac{3}{2}} \tag{C.27}$$

where a_1 is sound velocity in the point 1 evaluated by the means of $a_1 = \sqrt{\frac{\gamma p_1}{\rho_1}}$;

2. variables $p_{\frac{1}{2}}$, $\rho_{\frac{1}{2}}$, $u_{\frac{1}{2}}$ just now calculated, are used to evaluate temperature, total energy, etc...., essential for numerical integration; on ghost cell the following values are calculated by the means of:

$$p(0) = 2p_{\frac{1}{2}} - p_1 \tag{C.28}$$

$$rho(0) = 2\rho_{\frac{1}{2}} - \rho_1 \tag{C.29}$$

$$u(0) = u_{\frac{1}{2}} \tag{C.30}$$

$$T(0) = 2T_{\frac{1}{2}} - T_1 \tag{C.31}$$

$$Utot(0) = 2Utot_{\frac{1}{2}} - Utot_1 \tag{C.32}$$

where, with 0 index number, are indicated variables that belong to the cell with staggering;

3. values evaluated in equations (C.24 to C.27 on the current page) are calculated in a different point to integrate momentum conservation equation in i direction:

$$p_1 = \frac{1}{2} \left[p_{iniz} + p_{\frac{3}{2}} + \rho_{\frac{3}{2}} a_{\frac{3}{2}} \left(u_{iniz} - u_{\frac{3}{2}} \right) \right] \tag{C.33}$$

$$\rho_1 = \frac{1}{a^2} \left(p_{\frac{3}{2}} - p_{iniz} \right) + \rho_{iniz} \quad \text{se} \quad u_{\frac{3}{2}} < 0 \tag{C.34}$$

$$\rho_1 = \frac{1}{a^2} \left(p_{\frac{3}{2}} - p_{iniz} \right) + \rho_{\frac{3}{2}} \quad \text{se} \quad u_{\frac{3}{2}} \geqslant 0 \tag{C.35}$$

$$u_1 = \frac{\left(p_{\frac{3}{2}} - p_{iniz} \right)}{\left(\rho_{\frac{3}{2}} a_{\frac{3}{2}} \right)} + u_{\frac{3}{2}} \tag{C.36}$$

where with subscript $iniz$ initial values in points 0 and $\frac{1}{2}$ are indicated; in such manner domain is extended towards infinity and no acoustic wave entering to the internal field can come from initial condition.

4. ghost cell values (subscript 0) and at the center of the first cell (subscript 1) are used, respectively, in mass conservation and energy conservation equations right hand side evaluations, and for momentum conservation equation in i direction right hand side evaluation, at any Runge-Kutta substep.

C.2 Boundary Conditions Results Comparison

To evaluate all boundary conditions, a simple one-dimensional test case is been developed; at the right boundary non reflecting boundary conditions (NSCBC) are forced, while at the left boundary non reflecting boundary condition has been changed from NSCBC to simple extrapolation, "FaRo" and "FaRo NEW"; as initial condition, a compression-expansion-expansion-compression has been imposed (CEEC, see figure C.2a and C.2b).

(a) Mass flow

Best numerical results are obtained by the means of NSCBC boundary condition, while simple extrapolation shows a totally wrong behaviour and a non-reflecting outlet can't be accurately simulated: when the acoustic wave arrives to the left boundary (figure C.3d on page 118), extrapolation obtained pressure is underestimated in comparison with the other boundary conditions imposed; so, a reflecting acoustic wave, of the same magnitude of the original wave, propagates into the internal field. "FaRo" boundary conditions, also if doesn't obtain a good result as NSCBC, permit to achieve an enough good non-reflecting condition; "FaRo NEW" numerical results are close to NSCBC

(b) Pressure

Figure C.2.   Initial conditions

boundary condition, except for time instant where acoustic wave arrives on the boundary (figure C.3f on page 118) and time instant in which acoustic wave leaves internal field (figure C.2n on page 120).

"FaRo NEW" boundary condition is also very simple to implement, and furthermore physical boundary isn't moved, to the contrary of what happen when NSCBC is used; due to the particular position of flow variables, indeed, physical boundary is relocated from point $\frac{1}{2}$ to point 1 (see figure C.1 on page 112), where mass flow is re-collocated and waves amplitudes are evaluated (variables d_1, d_2, d_3): in this way, conservation equations are partially rewritten close to the

boundaries (numerical scheme hasn't second order global accuracy), and imple-
mentation is therefore harder and less straightforward.

(A) Mass flow at t=0.00003895s

(B) Pressure at t=0.00003895s

(C) Mass flow at t=0.00011678s

(D) Pressure at t=0.00011678s

(E) Mass flow at t=0.00013622s

(F) Pressure at t=0.00013622s
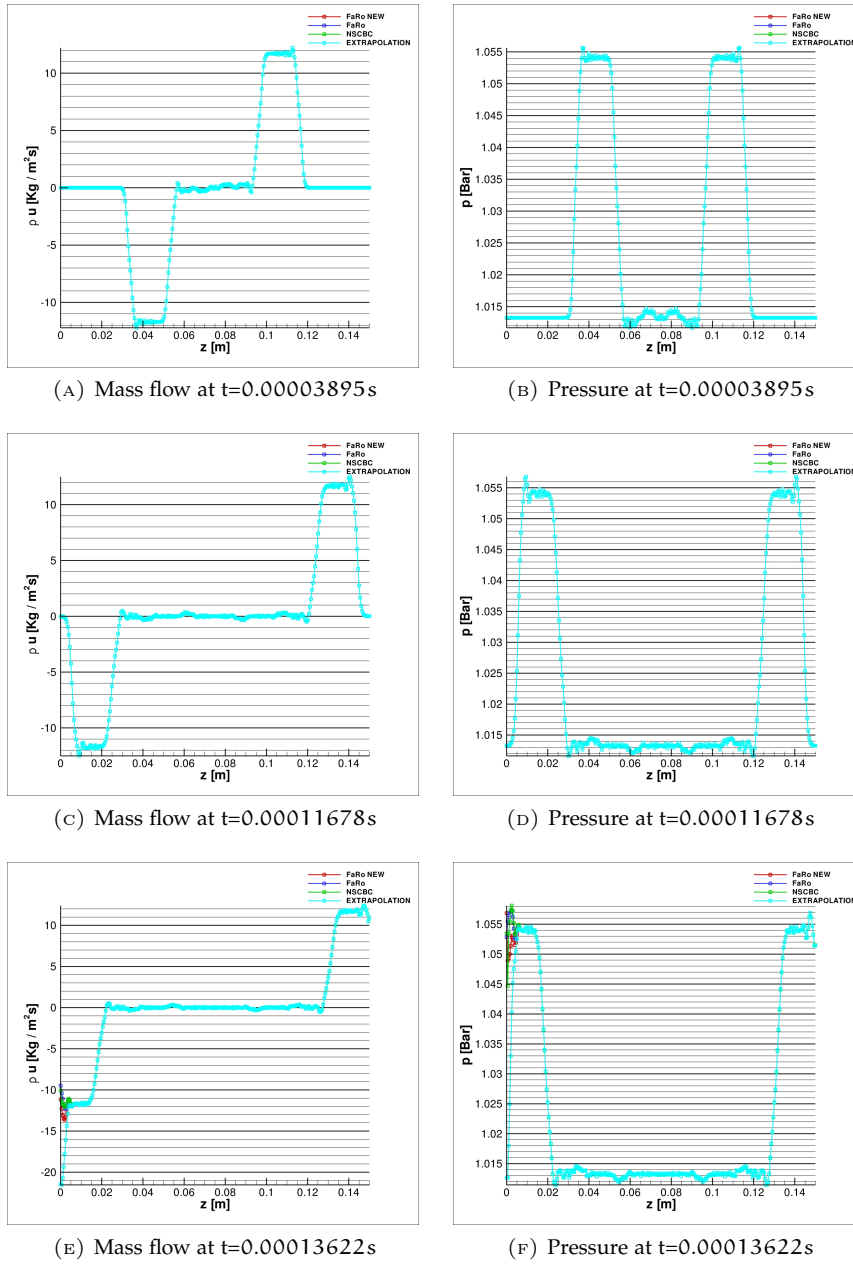
FIGURE C.3.   Numerical solution from t=0.00003895s to t=0.00011678s
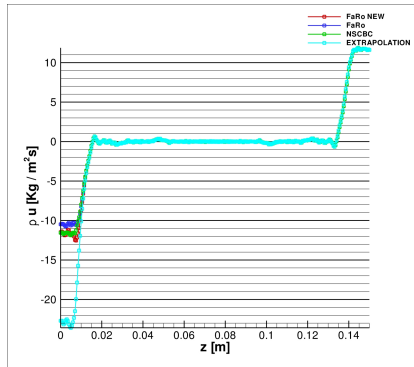
(G) Mass flow at t=0.00015526s
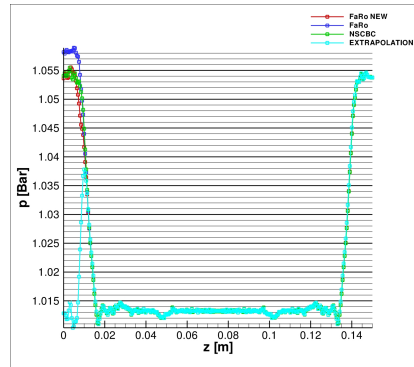
(H) Pressure at t=0.00015526s
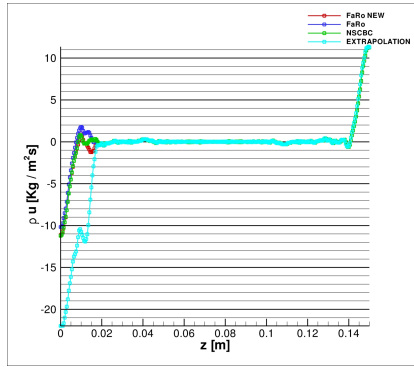
(I) Mass flow at t=0.00017433s
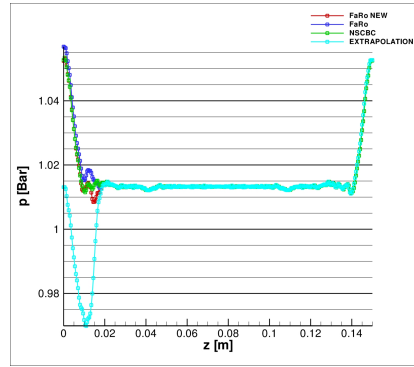
(J) Pressure at t=0.00017433s
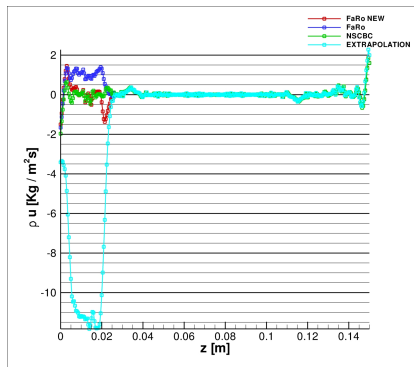
(K) Mass flow at t=0.00019376s
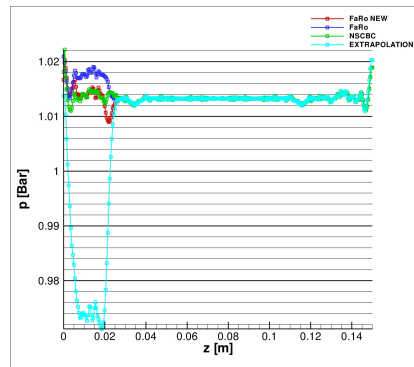
(L) Pressure at t=0.00019376s

FIGURE C.2.   Numerical solution from t=0.00015526s to t=0.00019376s
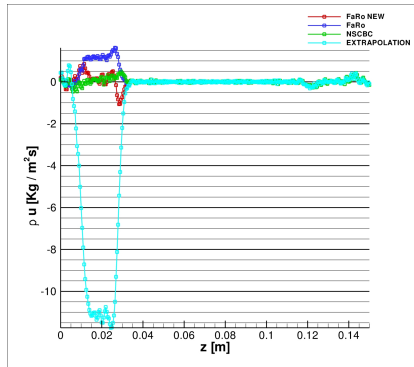
(M) Mass flow at t=0.00021343s
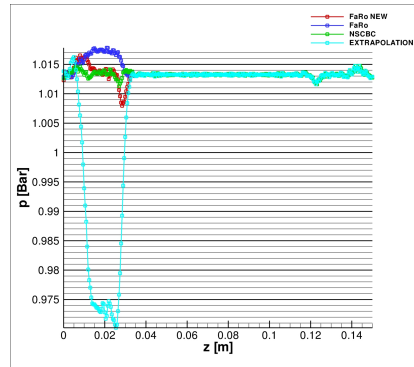
(N) Pressure at t=0.00021343s
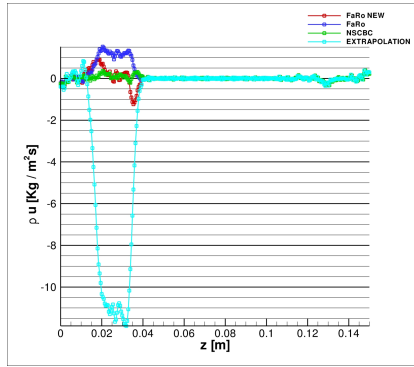
(O) Mass flow at t=0.00023311s
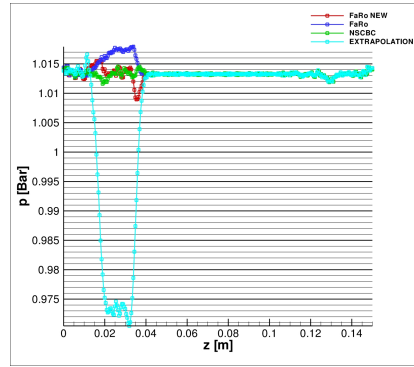
(P) Pressure at t=0.00023311s
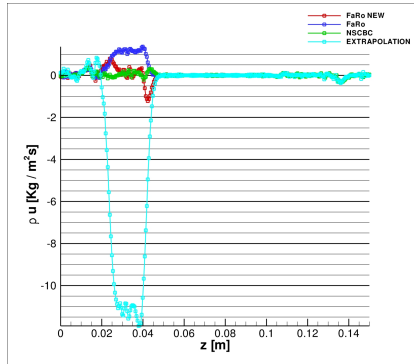
(Q) Mass flow at t=0.00025277s
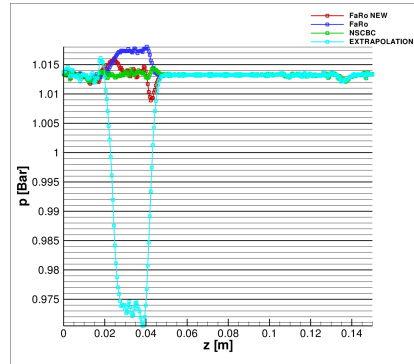
(R) Pressure at t=0.00025277s

FIGURE C.1. Numerical solution from t=0.00021343s to t=0.00025277s

Bibliography

Cecere, D., *Giacomazzi, E.*, *Picchia, F. R.* and *Arcidiacono, N. M. S.* Direct numerical simulation of a lean premixed ch_4/h_2–air slot flame. Combustion and Flame, volume 280:pages 1–27, 2015.

Cecere, D. and *Giacomazzi, E.* An immersed volume method for large eddy simulation of compressible flows using a staggered-grid approach. Computer Methods in Applied Mechanics and Engineering, volume 280:pages 1–27, 2014.

Giacomazzi, E., *Cecere, D.*, *Picchia, F. R.* and *Arcidiacono, N. M. S.* Sviluppo di un modello les per fiamme turbolente premiscelate. Technical Report 255, ENEA, 2014.

Cuoci, A., *Frassoldati, A.*, *Faravelli, T.* and *Ranzi, E.* A computational tool for the detailed kinetic modeling of laminar flames: Application to c_2h_4/ch_4 coflow flames. Combustion and Flame, volume 160:pages 870–886, 2013.

Hernandez-Perez, F. E., *Groth, C. P. T.* and *Gulder, O. L.* Les of a hydrogen-enriched lean turbulen premixed flame. In Proceedings of 51st AIAA Aerospace Sciences Meeting including the New Horizons Forum and Aerospace Exposition. 2013.

Donato, F., *Rossi, G.*, *Favini, B.*, *Giacomazzi, E.*, *Cecere, D.*, *Picchia, F. R.* and *Arcidiacono, N. M. S.* Les simulation of a devolatilization experiment on the ipfr facility. In Proceedings of XXXV Meeting of the Italian Section of the Combustion Institute. 2012.

Safta, C., *Ray, J.* and *Najm, N. N.* A high-order amr algorithm for chemically reacting flows. 2011. ICDERS 2011, Irvine, USA.

Shen, C., *Qiu, J.* and *Christlieb, A.* Adaptive mesh refinement based on high order finite difference weno scheme for multiscale simulations. Journal of Computational Physics, volume 230:pages 3780–3802, 2011.

Giacomazzi, E., *Cecere, D.*, *Donato, F.*, *Picchia, F. R.*, *Arcidiacono, N. M. S.*, *Daniele, S.* and *Jansohn, P.* Les analysis of a syngas turbulent premixed dump-combustor at 5 bar. In Proceedings of XXXIII Event of the Italian Section of the Combustion Institute. 2010.

Qianlong, L. A stable and accurate projection method on locally refined staggered mesh. International Journal for Numerical Methods in Fluids, volume 67:pages 74–92, 2010.

Bibliography

Donato, F. Numerical Modeling of Two-Phase Reactive Flows. Ph.D. thesis, University of Rome "Sapienza", Department of Electric Engineering, 2009.

Frassoldati, A., *Cuoci, A.*, *Faravelli, T.*, *Ranzi, E.*, *Candusso, C.* and *Tolazzi, D.* Simplified kinetic schemes for oxy-fuel combustion. In 1^{s}t International Conference on Sustainable Fossil Fuels for Future Energy. 2009.

Giacomazzi, E., *Picchia, F. R.*, *Arcidiacono, N. M. S.*, *Cecere, D.*, *Donato, F.* and *Favini, B.* Unsteady simulation of a co/h2/n2/air turbulent non-premixed flame. Combustion Theory and Modelling, volume 12:pages 1125–1152, 2008.

Lesieur, M. Turbulence in Fluids. Springer, 4th edition, 2008.

Nejat, A. and *Ollivier-Gooch, C.* A high-order accurate unstructured finite volume newton-krylov algorithm for inviscid compressible flows. Journal of Computational Physics, volume 227:pages 2582–2609, 2008.

Halter, F., *Chauveau, C.* and *Gokalp, I.* Characterizations of the effects of hydrogen addition in premixed methane/air flames. International Journal of Hydrogen Energy, volume 32:pages 2585–2592, 2007.

Mandilas, C., *Ormsby, M. P.*, *Sheppard, C. G. W.* and *Woolley, R.* Effects of hydrogen addition on laminar and turbulent premixed methane and iso-octane–air flames. Proceedings of the Combustion Institute, volume 31:pages 1443–1450, 2007.

Sankaran, R., *Hawkes, E. R.*, *Chen, J. H.*, *Lu, T.* and *Law, C. K.* Structure of a spatially developing turbulent lean methane-air bunsen flame. Proceedings of The Combustion Institute, volume 31:pages 1291–1298, 2007.

Cozzi, F. and *Coghe, A.* Behaviour of hydrogen-enriched non-premixed swirled natural gas flame. International Journal of Hydrogen Energy, volume 31:pages 669–677, 2006.

Filatyev, S. A., *Driscoll, J. F.*, *Carter, C. D.* and *Donbar, J. M.* Measured properties of turbulent premixed flames for model assessment, including burning velocities, stretch rates, and surface densities. Combustion and Flame, volume 141:pages 1–21, 2005.

Poinsot, T. and *Veynante, D.* Theoretical and Numerical Combustion. Edwards, 2nd edition, 2005.

Thompson, H. D., *Webb, B. W.* and *Hoffman, J. D.* The cell reynolds number myth. International Journal for Numerical Methods in Fluids, volume 5(4):pages 305–310, 2005.

Luche, J., *Reuillon, M.*, *Boettner, J. C.* and *Cathonnet, M.* Reduction of large detailed kinetic mechanisms: Application to kerosene/air combustion. Combustion Science and Technology, volume 176:pages 1935–1963, 2004.

Manhart, M. A zonal grid algorithm for dns of turbulent boundary layers. Computers & Fluids, volume 33:pages 435–461, 2004.

Bibliography

Klein, M., *Sadiki, A.* and *Janicka, J.* A digital filter based generation of inflow data for spatially developing direct numerical or large eddy simulations. Journal of Computational Physics, volume 186:pages 652–665, 2003.

Nagarajan, S., *Lele, S. K.* and *Ferziger, J. H.* A robust high-order compact method for large eddy simulation. Journal of Computational Physics, volume 191:pages 392–419, 2003.

Terracol, M., *Sagaut, P.* and *Basdevant, C.* A time self-adaptive multilevel algorithm for large-eddy simulation. Journal of Computational Physics, volume 184:pages 339–365, 2003.

Schefer, R. W., *Wicksall, D. M.* and *Agrawal, A. J.* Combustion of hydrogen-enriched methane in a lean premixed swirl stabilized burner. Proceedings of the Combustion Institute, volume 29:pages 843–851, 2002.

Borée, J., *Ishima, T.* and *Flour, I.* The effect of mass loading and inter-particle collisions on the development of polydispersed two-phase flow downstream a confined bluff body. Journal of Fluid Mechanics, volume 443:pages 129–165, 2001.

Mitran, S. M. A comparison of adaptive mesh refinement approaches for large eddy simulation. 2001.

Quéméré, P., *Sagaut, P.* and *Couailler, V.* A new multi-domain/multi-resolution method for large-eddy simulation. International Journal for Numerical Methods in Fluids, volume 36:pages 391–416, 2001.

Terracol, M., *Sagaut, P.* and *Basdevant, C.* A multilevel algorithm for large-eddy simulation of turbulent compressible flows. Journal of Computational Physics, volume 167:pages 439–475, 2001.

Kee, R. J., *Dixon-Lewis, G.*, *Warnatz, J.*, *Coltrin, M. E.*, *Miller, J. A.* and *K., M. H.* The chemkin collection iii: Transport. Reaction Design: San Diego, 1998.

Boersma, B. J., *Kooper, M. N.*, *Nieuwstadt, F. T. M.* and *Wesseling, P.* Local grid refinement in large-eddy simulations. Journal of Engineering Mathematics, volume 32:pages 161–175, 1997.

Ollivier-Gooch, C. Quasi-eno schemes for unstructured meshes based on unlimited data-depended least-squares recostruction. Journal of Computational Physics, volume 133:pages 6–17, 1997.

Tannehill, J. C., *Anderson, D. A.* and *H., P. R.* Computational Fluid Mechanics and Heat Transfer. Taylor & Francis, 1997.

Sullivan, P. P., *McWilliams, J. C.* and *Moeng, C.* A grid nesting methos for large-eddy simulations of planetary boundary-layer flows. Boundary Layer Metereology, volume 80:pages 167–202, 1996.

Versteeg, H. K. and *Malalasekera, W.* An Introduction to Computational Fluid Dynamics. Longman, 1995.

Bibliography

Liou, M. S. and *Steffen, C. J.* A new flux splitting scheme. Journal of Computational Physics, volume 107:pages 23–39, 1993.

Sommerfeld, M. and *Qiu, H. H.* Characterization of particle-laden, confined swirling flows by phase-doppler anemometry and numerical calculation. International Journal of Multiphase Flow, volume 19(6):pages 1093–1127, 1993.

Meneveau, C. and *Poinsot, T.* Stretching and quenching of flemelets in premixed turbulent combustion. Combustion and Flame, volume 86:pages 311–332, 1991.

Sommerfeld, M. and *Qiu, H. H.* Detailed measurements in a swirling particulate twophase flow by a phase-doppler anemometer. International Journal of Heat and Fluid Flow, volume 12:pages 20–28, 1991.

Berger, M. and *Colella, P.* Local adaptive mesh refinement for shock hydrodynamics. Journal of Computational Physics, volume 82:pages 64–84, 1989.

Shu, C. W. and *Osher, S.* Efficient implementation on essentially non-oscillatory shock-capturing schemes. Journal of Computational Physics, volume 83:pages 32–78, 1989.

Hishida, K., *Takemoto, K.* and *Maeda, M.* Turbulent characteristics of gas-solid two-phase confined jet. Japanese Journal of Multiphase Flow, volume 1(1):pages 56–69, 1987.

Kuo, K. K. Principles of Combustion. John Wiley and Sons Inc., 1986.

Leonard, B. P. A stable and accurate convective modelling procedure based on quadratic upstream interpolation. Computer Methods in Applied Mechanics and Engineering, volume 19:pages 59–98, 1979.

Brandt, A. Multi-level adaptive solutions to boundary-value problems. Mathematics of Computation, volume 31(138):pages 333–390, 1977.

Bird, R. B., *Stewart, W. E.* and *Lightfoot, E. N.* Transport phenomena. John Wiley & Sons, Inc., New York, 1960.

Stefan, J. über das gleichgewicht und die bewegung, insbesondere die diffusion von gasmengen. Sitzungsber. Akad. Wiss. Wien, volume 63:pages 63–124, 1871.

Maxwell, J. C. Illustration of the dynamical theory of gases. part 1. on the motions and collisions of perfectly elastic spheres. Phil. Mag., volume 19:pages 19–32, 1860a.

Maxwell, J. C. Illustration of the dynamical theory of gases. part 2. on the process of diffusion of two or more kinds of moving particles among one other. Phil. Mag., volume 20:pages 21–37, 1860b.

Smith, G. P., *Golden, D. M.*, *Frenklach, M.*, *Moriarty, N. W.*, *Eiteneer, B. et al.* Gri-mech detailed mechanism. http://www.me.berkeley.edu/gri_mech/.